Aalto University
School of Chemical
Engineering

Linda Sederholm

STRUCTURAL AND MAGNETIC PROPERTIES OF B SITE ORDERED DOUBLE PEROVSKITES

Master's programme in Chemical, Biochemical, and Materials Engineering
Major in Functional Materials

Master's thesis for the degree of Master of Science and Technology
Submitted for inspection, Espoo, 30 September, 2019

Supervisor Prof. Maarit Karppinen

Instructors Dr Girish Tewari
Dr Divya Srivastava

Aalto University
School of Chemical
Engineering

Aalto University, P.O. BOX 11000, 00076 AALTO
www.aalto.fi

Abstract of master's thesis

Author Linda Sederholm

Title of thesis Structural and magnetic properties of B site ordered double perovskites

Degree Programme Master's programme in Chemical, Biochemical, and Materials Engineering

Major Functional Materials

Thesis supervisor Prof. Maarit Karppinen

Thesis advisor(s) Dr. Girish Tewari and Dr. Divya Srivastava

Date 30.09.2019 **Number of pages** 81 **Language** English

Abstract

Perovskites (ABO_3), and especially double perovskites ($A'A''B'B''O_6$) provide an exceptionally versatile template for chemical substitution and fine-tuning of physical and chemical properties, including magnetic interactions. The geometry of B-site ordered double perovskites especially supports useful magnetic interactions, from ferromagnetism to exotic ground states such as half-metallicity and frustrated spin states. However, the vast space of hypothetic perovskite compositions poses a challenge in finding the elemental combinations with optimal properties. New methods are needed for wide-field screening of possible compositions to identify regions of interest.

This thesis provides a thorough review of the structural and compositional considerations of B site ordered inorganic oxide double perovskites needed for understanding their magnetic behaviour, including distortions, ordering effects, and physical and chemical pressure. The mechanisms of magnetic ordering and the appearance of exotic ground states are presented through theory and examples. Emphasis is put on the correlation between stoichiometry defined geometric parameters and magnetic superexchange interactions. Multivariate analysis is presented as a novel method for using these correlations to predict the magnetic behaviour of new phases, and find new candidates for ferromagnetic behaviour by a statistical approach.

The relationship between chemical composition and structural parameters is experimentally investigated in the $(Ba_{1-x}Sr_x)_2CoIrO_6$ perovskite series, in which chemical pressure is introduced by A site substitution, inducing a structural transition from hexagonal to cubic perovskite. Furthermore, a close structural examination of La_2FeIrO_6 is performed by comparing experimental data with the calculated optimal structure, as found by density functional theory, providing new information on the phase composition. Finally, the magnetic ground state of La_2FeIrO_6 is predicted by both density functional theory and multivariate analysis, and the results of the two methods are compared.

Keywords: perovskite, B site ordering, chemical pressure, magnetism, spin interactions, predictive methods, multivariate analysis

Aalto-universitetet
Högskolan för
kemiteknik

Aalto-universitetet, PB 11000, 00076 AALTO
www.aalto.fi

Sammandrag av diplomarbetet

Författare Linda Sederholm

Titel Strukturella och magnetiska egenskaper hos B-positionsordnade dubbelperovskiter

Utbildningsprogram Magisterprogrammet i kemi, biokemi och materialvetenskap

Huvudämne Funktionella Material

Övervakare Prof. Maarit Karppinen

Handledare Dr. Girish Tewari och Dr. Divya Srivastava

Datum 30.09.2019 **Sidantal** 81 **Språk** Engelska

Sammandrag

Perovskiter (ABO_3), och särskilt dubbelperovskiter ($A'A''B'B''O_6$) erbjuder en särdeles mångsidig startpunkt för kemisk substitution och finjusteringar av fysikaliska och kemiska egenskaper, inklusive magnetisk växelverkan. B-positionsordnade dubbelperovskiters geometriska struktur möjliggör särskilt användbara magnetiska beteenden, från ferromagnetism till exotiska grundtillstånd såsom halvmetalliska och frustrerade spintillstånd. Den ofantliga rymden av hypotetiska perovskitsammansättningar utgör emellertid en utmaning i sökandet efter grundämneskombinationer med optimala egenskaper. Nya metoder krävs för att på bred front genomsöka de möjliga kombinationerna och identifiera områden av intresse.

Detta diplomarbete erbjuder en grundlig presentation av strukturella och sammansättnings-mässiga aspekter av B-positionsordnade dubbelperovskiter som är relevanta för att förstå dessa materials magnetiska beteende, inklusive förvridningar, kemisk ordning, och fysikaliskt samt kemiskt tryck. Mekanismerna bakom magnetisk ordning och uppkomsten av exotiska grundtillstånd presenteras per teori och exempel. Korrelationen mellan stökiometriskt definierade geometriska parametrar och magnetisk utbytesväxelverkan betonas. Multivariabelanalys presenteras som en ny metod för utnyttjande av dessa korrelationer för att förutspå magnetiskt beteende hos nya faser, och hitta nya kandidater för ferromagnetism per statistisk analys.

Förhållandet mellan kemisk sammansättning och strukturella parametrar utforskas experimentellt i perovskitserien $(Ba_{1-x}Sr_x)_2CoIrO_6$, i vilken kemiskt tryck introduceras per substituering i position A, vilket föranleder en strukturförändring från hexagonal till kubisk perovskit. Vidare utförs en noggrann utvärdering av strukturen hos La_2FeIrO_6, i form av en jämförelse mellan experimentella data och den beräknade optimala strukturen, som erhålls med hjälp av täthetsfunktionalteori (density functional theory, DFT). Således erhålls nya rön gällande strukturens fassammansättning. Slutligen förutspås det magnetiska grundtillståndet hos La_2FeIrO_6 med hjälp av både DFT och multivariabelanalys, och de två metodernas utlåtanden jämförs.

Nyckelord: perovskit, elpasolit, B-positionsordning, kemiskt tryck, magnetiska egenskaper

Contents

Abbreviations

AFM	Antiferromagnet(-ic)
BVS	Bond valence sum
DFT	Density Functional Theory
FA	Factor analysis
FiM	Ferrimagnet(-ic)
FM	Ferromagnet(-ic)
HM	Half-metal(-lic)
JT distortion	Jahn-Teller distortion
LDA	Linear discriminant analysis
MgVA	Megavariate Analysis
MLR	Multiple linear regression
MVA	Multivariate Analysis
MVDA	Multivariate Data Analysis
NM	Nonmagnetic
PC	Principal component
PCA	Principal component analysis
RS	Rock salt
SG	Spin glass
SL	Spin liquid
t	Tolerance parameter
ϕ	Fitness factor

1 Introduction

The perovskite material class is named after the perovskite mineral, $CaTiO_3$, which was discovered in the Ural mountains in Russia in 1839 by German mineralogist Gustav Rose, and named after the Russian nobleman Lev Perovski. Its crystal structure was first described by Goldschmidt [1] in 1926, and investigated years later using X-ray diffraction. [2,3] The ideal perovskite is cubic, and highly tolerant for substitutions: almost any naturally occurring, stable ion can be incorporated in the structure, including small-molecule organic ions. [4–6] The number of possible perovskite compositions, even after limiting the calculations to chemically and structurally plausible B site ordered double perovskites, circles around an astounding $\sim 10^{14}$ possibilities. [7] Hopes are high that several of the as-yet-untried compositions would reveal superior properties. Perovskite phases have been suggested for a wide selection of applications, from sustainable energy harvesting and storage, to novel data storage and computing technology based on spin behaviour (spintronics). [4,8,9] A sister phase of perovskites has gained fame for one of its members expressing superconductivity at relatively high temperatures, namely $YBa_3Cu_3O_{7+\delta}$. [10]

A widely investigated perovskite variation is the double perovskite, in which one or both cation sites holds a 1:1 ratio of two species. Ordered B site double perovskites, also known as *elpasolites,* have the chemical formula $A_2B'B''O_6$ and present an excellent template for fine-tuning of magnetic interactions. Useful properties include multiferroic phases and ferromagnetic conductivity [11], and frustrated magnetic ground states such as spin liquid, spin glass, and spin ice. [12–15] The appearance of these exotic behaviours is highly sensitive to small changes in bonding distances and bond angles, as well as element and charge distribution, which can be controlled by adjustments in the chemical composition and synthesis parameters. Mismatched ionic radii are compensated by distortions of the perovskite structure, which, at its most severe, alters the atomic connectivity and replaces the perovskite lattice with a hexagonal phase. Application of pressure can restore the perovskite structure by altering effective ionic radii. [16]

A central concept in this thesis is chemical pressure, which can imitate physical pressure in some cases and induce a phase transition from hexagonal to cubic structure, [17] enabling wanted magnetic interactions which are not available in the hexagonal structure. The theoretical understanding of the perovskite structure, gained in the first part of this work, is applied experimentally in the synthesis and structural analysis of the series $(Ba_{1-x}Sr_x)_2CoIrO_6$, which transforms from hexagonal to cubic as the chemical pressure is adjusted by A site substitution. In La_2FeIrO_6, the magnetic interactions

affect the crystal structure, which is investigated computationally using density functional theory (DFT), and compared to the experimentally obtained structure.

Furthermore, multivariate analysis (MVA) is presented as a novel method for predicting magnetic ordering and novel candidates for ferromagnetic perovskite compositions. As traditional theory-based methods are too slow for wide-field screening and too complex for a reverse-engineering approach, statistical methods provide a novel tool for fast identification of possible compositions of interest. In this work, the magnetic structure of La_2FeIrO_6 is predicted by MVA and compared to the magnetic ground state obtained by DFT, supporting the tactic of using blind-to-theory chemometrics for finding hitherto unknown correlations between phase parameters and material properties.

The study is limited to inorganic B site ordered double perovskites with oxygen on the anion site, omitting the large classes of organic and hybrid organic-inorganic perovskites, non-oxide perovskites, and cationic substitution on the A site, aside from its use for controlling chemical pressure.

2 The perovskite structure

The ideal perovskite unit cell is described by the formula ABX_3, where A and B are cations and X is an anion, most commonly oxygen. The model unit cell is cubic with an ideal side length $a_0 = 3.905$ Å and $Pm\bar{3}m$ symmetry, and can be drawn up by placing the A cations in the corners, the B cation in the centre, and the X anion positioned on the centre of all six faces of the cube, as illustrated in Figure 1a. The B cation has a fixed coordination of 6, and in the standard depiction, the B cation and X anions are grouped together into octahedral BX_6 units. An alternative and more frequently used standard setting thus shows the structure as a lattice of corner-sharing BX_6 octahedra with the A cations placed in the 12-coordinated intermediate sites, shown in Figure 1b.

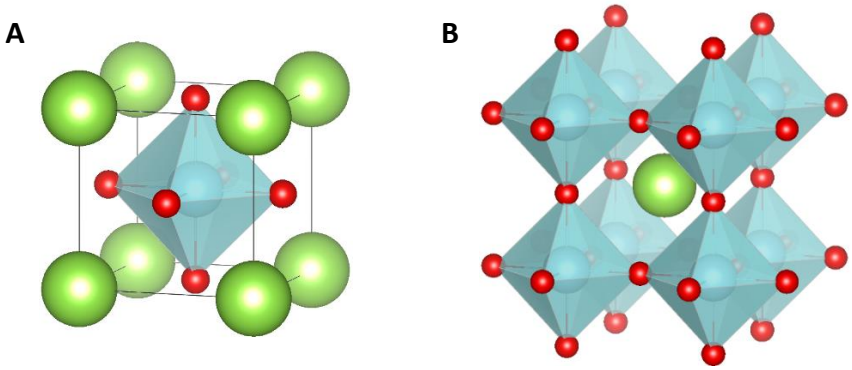

Figure 1. The standard depiction of the ideal perovskite unit cell uses two alternative settings: a) centred on the B cation, and somewhat more frequently, b) centred on the A cation.

Despite a varying level of covalence in the bonding regime, the perovskite structure is often assumed ionic for the purpose of description. A vast majority of perovskite phases are metal oxides, but other chemical species can also be incorporated into the perovskite structure. In addition to oxygen, the anion site accepts other chalcogens down to tellurium, halogens down to iodine, nitrogen, and even small-molecule anions [1,4,7,18,19]. The clear preference for oxygen is combinatorically explained by the ionic radius and charge of the O^{-2} ion. For the halogen anions, the range of cation oxidation states is limited to only +1 or +2, severely limiting the number of cation combinations available for halide perovskites. Nitride perovskites are limited by the high charge density of the N^{3-} ion, forcing the cations into exceptionally high oxidation states, in which most cations are too small for the B site. With a chalcogenide on the X site, the range of allowed cation oxidation states on the B site is the widest, stretching from +1 to +5. However, the ionic radii grow relatively large already with the S^{-2} ion, severely restricting the cation combinations that fulfil the requirements of the perovskite

structure for all chalcogenides except oxygen. Between the cations, the A site retains a strong preference for holding the less charged, often larger species, and is therefore limited to oxidation states +1…+3.[1]

The structure is highly tolerant for substitutions. Although both cation sites are able to host multiple chemical species at once, binary substitutions of recognizable stoichiometry are predominant. The term *double perovskite* is used for phases where one or both of the cation sites consists of a 1:1 distribution of two elements, either ordered or disordered. In case of an ordered phase, the unit cell is expanded to accommodate the full pattern. Figure 2 depicts a specific case of double perovskites, called *elpasolites*, where the B site is doubled with a 1:1 stoichiometry and is rock salt ordered. Ideally, the structure thus expresses $Fm\bar{3}m$ symmetry. A closer discussion on substitution stoichiometry and ordering of co-occupied sites is provided in chapter 3.

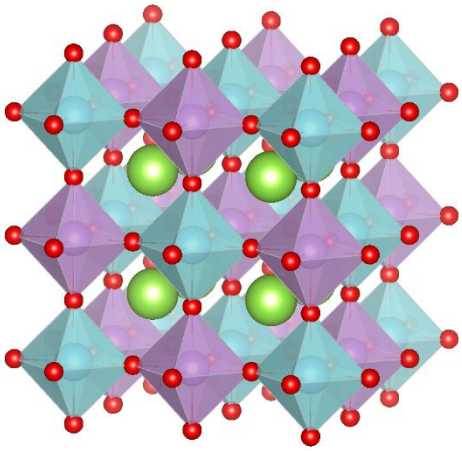

Figure 2. The elpasolite structure makes a special case of double perovskites with a rock salt ordered B site, written $A_2B'B''O_6$. The unit cell is expanded to accommodate the full pattern, which is equivalent to eight times the single perovskite unit cell.

When splitting a lattice site into two or several parts, the question arises in which order the elements sharing the site should be reported. With no clear and consistent physical or chemical differences between split sites, human convenience motivates the order in which site-sharing species are reported. In lack of global rules to dictate nomenclature, several local customs have evolved. A common praxis separates ordered and disordered perovskites by multiplying the compound formula into the $A'A''B'B''O_6$ form only for ordered double perovskites[1]. For disordered perovskites, lower-index equations of type ${A'}_{1-x}{A''}_x{B'}_{1-y}{B''}_yO_3$ are commonly used, and are especially practical when both sites are unequally substituted. Enclosing site-sharing species in brackets as $(A'A'')(B'B'')O_3$ can be clarifying when multiple species are involved, and for annotating sample series of varying

[1] Or other multiplicity depending on co-occupant ratios, such as $A'A''_2B'B''_2O_9$ or $A'A''_3B'_2B''_2O_{12}$.

ratios between the bracket-enclosed species. Following the customs of inorganic chemistry, the species of lower charge is written first: if the ions hold the same charge, the order is determined by the minimal, or else the maximal available oxidation state. Ultimately, atomic number decides the order between elsewise identical ions. However, deviations from these principles are frequent, and can for example be motivated by the logic of the experiment. A typical case is doping, in which case the dopant is often written after the default occupant of the site.

2.1 Phase stability

In order to evaluate whether a given elemental combination is viable for forming a perovskite phase, a selection of parameters derived from the ionic radii of the suggested species have been developed. Theoretical ion sizes considering both ion charge and coordination environment have been presented by Shannon [20] and remain the most widely used. Stable phase formation also requires suitable bonding environments for all species in the phase, considering both bond lengths and coordination number. The coordination environment can be evaluated by bond strain investigations, comparing the structurally suggested bond lengths and number of bonds to the preferred bond lengths and availability of bonding electrons. Depending on the electron structure of the ion, a certain coordination number might be preferred over another. Especially the d-block metals, which incorporate d-orbitals in bond formation, can be sensitive to the geometry of the coordination environment as a direct consequence of the spatial distribution of the valence orbitals. [7]

2.1.1 Tolerance parameter and fitness factor

Assuming a rigid-sphere model, the ideal perovskite structure can be investigated geometrically in order to find the internal proportions of the ionic species in the ideal structure case, where all species are in contact with one another without leaving any ion free to rattle in its site. This geometrical restriction is normally reformulated into the *Goldschmidt tolerance factor* t, based on structural concepts first presented by Goldschmidt in 1926. [21] The equation for t is presented in *Equation 1*, which yields $t = 1$ for the ideal perovskite phase. Accounting for substitutions, $\bar{R}_n$ denotes the weighed-average ionic radius of all species occupying the site n.

$$t = \frac{\bar{R}_A + R_X}{\sqrt{2} \cdot (\bar{R}_B + R_X)} \qquad \text{Equation 1}$$

The Goldschmidt tolerance factor can be used to predict whether the ideal perovskite structure will form, if it will be distorted, or if the atomic connectivity is broken by too severe mismatch of ionic radii. As neither the ionic radii nor the rigid-sphere model is exact, a phase of ideal or near-ideal perovskite can form even if the calculated tolerance parameter is not precisely equal to unity. Thus, phases with tolerance parameters larger than one have been found, despite the theoretical stipulation that a too large A cation will destabilize the structure. Generally, the range of perovskite formation determined from reported phases is around $0.85 \dots 1.07$ with the vast majority of compounds appearing within the $0.93 \dots 1.01$ range. [12 SI]

A more detailed model for the allowed ion radii combinations has been developed by Filip et.al [1]. Adding a closer consideration of the octahedra, represented by the octahedral factor μ, average octahedral factor $\bar{\mu}$, and octahedral mismatch $\Delta\mu$ (Equation 2 a-b), allows the construction of a *space of stability* for double perovskites. The space is drawn up by the parameters t, $\bar{\mu}$, and $\Delta\mu$, and is presented in Figure 3.

a) b)

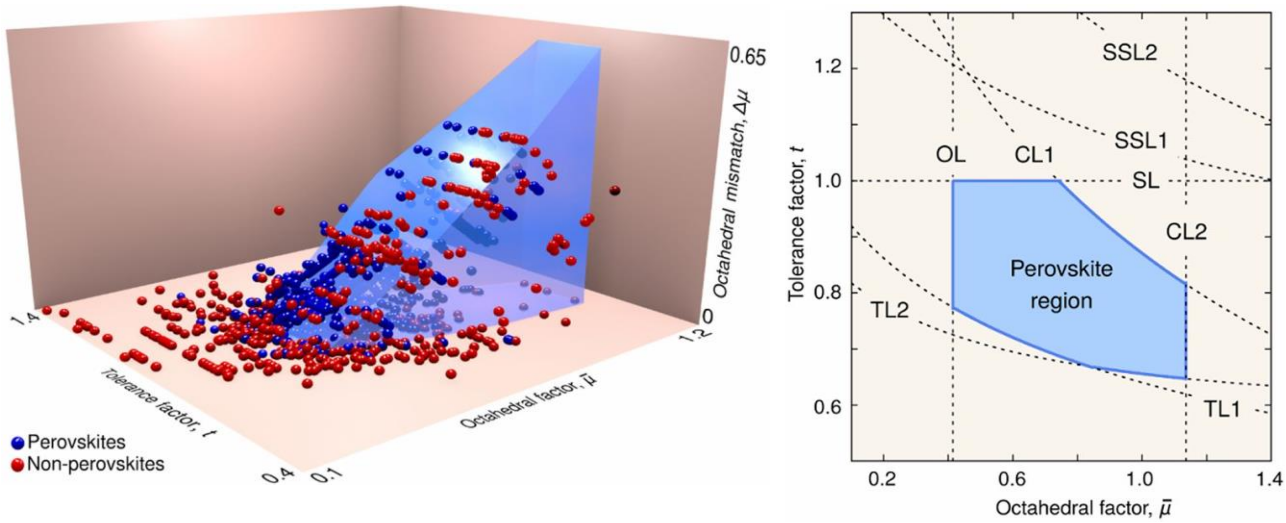

Figure 3. a) The space of stability for B site ordered double perovskite formation, drawn up in the (t, μ, Δμ) space, with experimentally successful (blue) and unsuccessful (red) perovskite syntheses marked with dots. b) The boundaries of the space are illustrated in the projection to the base of the stability space, with the limits expressed with dashed lines: chemical limits (CL), octahedral limit (OL, stretch limit (SL), and tilt limits (TL) (left). Theoretical secondary stretch limits (SSL) are also included. (Reprinted from ref [1], fig 1e and 2.)

$$\mu = \frac{R_B}{R_X} \quad \rightarrow \quad \bar{\mu} = \frac{\bar{R}_B}{R_X} \qquad \text{Equation 2a}$$

$$\Delta\mu = \frac{|R_A + R_O|}{2\,R_X} \qquad \text{Equation 2b}$$

The limits of the space of stability are derived from a geometric analysis, and yields four groups of limiting factors: [1]

1) The *stretch limit* dictates the maximal size of the A cation as touching all 12 of its surrounding X anions, and translates into the upper boundary for *t*

$$t \leq 1, \text{ equivalent to}$$

$$R_A + R_X \leq \sqrt{2}(R_B + R_X)$$

2) The *tilt limit* dictates the maximal tilting of adjacent octahedra as when their equatorial X anions touch, and translates into a lower limit for *t*

$$t \geq \ddot{\rho}_\mu/\sqrt{2}\,(\mu + 1)$$

3) The *octahedral limit* dictates the minimum size of the B cation as allowing all 6 of its surrounding X anions to touch, and defines the lower boundary

$$\sqrt{2}(R_B + R_X) < 2\,R_X$$

$$(\bar{\mu} \geq \sqrt{2} - 1 + \Delta\mu)$$

4) The *chemical limit* dictates the upper bounds of *t* and $\bar{\mu}$ based on the reality of the smallest available anion and largest available cations (X = F^-, A = Cs^+, B = Fr^+ & Ac^{3+} for a double perovskite)

$$t \leq (R_{Cs^+}/R_{F^-} + 1)/\sqrt{2}\,(\mu + 1)$$

$$\bar{\mu} \leq (R_{Fr^+} + R_{Ac^{3+}})/2R_{F^-}$$

The tilt limit is dependent on a piecewise function $\ddot{\rho}_\mu$, which takes into consideration that the axial tilt angle θ and the axial rotation φ (Figure 4) dominate the tilt limit in different regimes of the octahedral factor μ, thus setting a limit for the ratio ρ_μ (Equation 3). Subsequently, the tilt limit divides into two equations defined by $\ddot{\rho}_\mu$, as $\ddot{\rho}_\mu = 0.44\bar{\mu} + 1.37$ (TL1) and $\ddot{\rho}_\mu = 0.73\bar{\mu} + 1.13$ (TL2). Detailed mathematical derivations of these functions can be found in reference [1], SI.

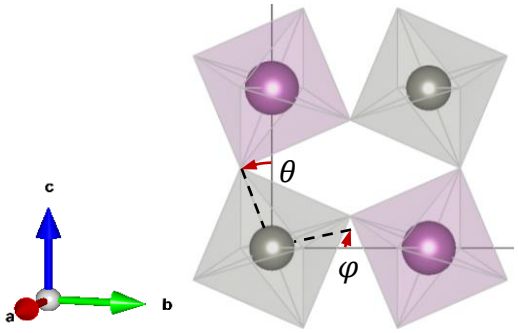

Figure 4. Axial tilt θ and rotation angle φ for calculating the limits of the space of stability, with θ given as absolute angle to the c-axis, and φ as the rotational component in the ab-plane.

$$\rho_\mu = \frac{R_A + R_X}{R_X} \qquad \text{Equation 3}$$

If the A site cation is too small for its site, indicated by both the form factor and the tolerance parameter taking a value below unity, distortions must be introduced to retain the atomic

connectivity. Discussed further in Chapter 2.2, octahedral tilting is the dominating mode of deformation. Accompanying distortions of the unit cell parameters break the cubic symmetry of the ideal phase. In order to predict not only formability, but also the symmetry of the phase formed, further attention is given to the ratio of cation radii by Teraoka *et.al* [22]. Based on a simple Pythagorean analysis of the ionic radii of an ideal single perovskite, the *fitness factor* Φ can be formulated, as presented in Equation 4.

$$\Phi = \frac{\sqrt{2}\,\bar{R}_A}{(\bar{R}_B + R_X)} \qquad \text{Equation 4}$$

As with the Goldschmidt tolerance factor, increasing deviations from unity signifies increasing severity of deformations. Above $\Phi = 1.00$ phases tend to be cubic; this distorts to tetragonal for $1.00 > \Phi > 0.93$; orthorhombic is found for $0.93 > \Phi > 0.90$; and below $\Phi \approx 0.90$ monoclinic and lower symmetries dominate. Various distortions can affect the symmetry of phases and induce axial tilting even when the value of Φ would indicate a higher symmetry.

Slightly oversized A ions induce tetragonal symmetry by stretching the c-axis. However, larger A cations will break the perovskite structure, since there are no further modes of distortion that could compensate for octahedra being forced apart. Instead, a too large strain on the B-O-B bonds will convert the structure to a hexagonal phase. The transformation is best visualized by depicting the ideal perovskite structure in a hexagonal setting, in which the layers of BO_6-octahedra along the cubic planes $(1\ 1\ 0)_c$ take on a cubic close packing with an A-B-C stacking sequence. The transition from cubic to hexagonal structure is gradual with increasing oversizing of the A cation, altering the stacking sequence of single layers by introducing hexagonally stacked layers with increasing frequency. Various sequences are possible, and the phases are named according to the periodicity of the stacking. [23] The similarity between cubic perovskite and two examples of its hexagonal sister phases are illustrated in Figure 5.

The ratio between octahedral and hexagonal AO_3 layers depends on the extent of the ion radii mismatch. A hexagonal stacking alters the interconnectivity of BO_6 octahedra, introducing face-sharing at the hexagonally stacked oxygen layers that make up the interface between layers of octahedra. This creates 90° B-O-B bonding angles as the B cations are brought closer to each other. If the repulsion between too-close B cations is strong, the hexagonal phase can be destabilized. Some B cations can form pairwise metal bonding to counteract the electrostatic repulsion, such as in $BaRuO_3$ [23], while in other cases strain is relieved by introducing patterns of B site vacancies in the face-sharing layers of octahedra. [25]

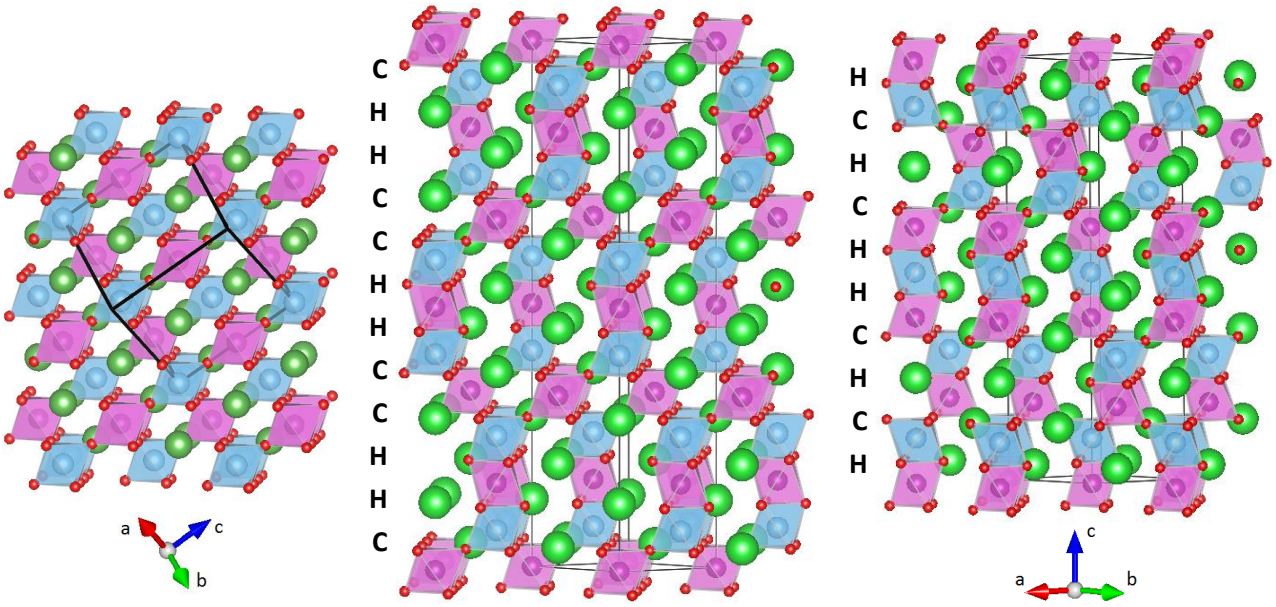

Figure 5. Comparison of the structures of ideal cubic double perovskite (left), and two hexagonal perovskites, 12-layered 12R (middle) and 10-layered 10H (right). The stacking of each oxygen layer is shown along the side of each hexagonal structure, H for hexagonal and C for cubic stacking. All structures are seen along $(1\ 1\ 0)_c$ for similar orientation of octahedra. (Figure adapted from ref [24])

2.1.2 Bond valence sum

The concept of bond valence sum (BVS) presents a rough method for evaluating whether the bonding in a suggested phase is viable or not, and which bond might be strained or unstable. Such information helps predict whether a phase will form, degrade, or present distortions. The BVS method is based on Pauling's rules for ionic coordination [26], which state that the valence V of an atom must be equal to the sum of the valences of its bonds (v_i) (Equation 5). Atomic valence is determined by the number of electrons available for bonding in the atom's valence shell. Each bond's valence can be calculated based on the measured bond length R_i. This is shown in Equation 6, where R_0 stands for the ideal bond length when the atom has valence 1, and b is an empirical parameter, often taking values close to 0.37 Å. The values of these parameters are dependent on bonding regime and can be found in literature.[2]

$$V = \sum v_i \qquad \text{Equation 5}$$

$$v_i = \exp\left(\frac{R_0 - R_i}{b}\right) \qquad \text{Equation 6}$$

[2] Tabulated values for R_0 and b in different bonding regimes are provided online and kept up-to-date by the International Union of Crystallography. [140]

If the calculated bond valence sum does not match the valence of the atom in question, it is said to be overbonded ($V < \sum v_i$) or underbonded ($V > \sum v_i$). Small mismatches in calculated values can be expected since the tabulated values are not precise, and bonding regimes are open for interpretation. Notable mismatches, however, indicate an unstable phase or a need for distortions for the phase to be stable, for example adjustment of the atomic positions, to find an arrangement that better fulfils the valence requirements of the atom. This can include a rearrangement of neighbouring atoms, leading to altered coordination numbers. Some elements can also accept bonding mismatch and adapt mixed valence states, discussed further in Section 3.3.

2.2 Structural distortions

As the aristotype perovskite poses strict boundaries for the ratios of the ionic species, perovskites of ideal structure are in minority. When ionic radii do not match perfectly, distortions are introduced to compensate for the mismatch and restore stable bonding. In total, three types of distortions are possible in perovskites: octahedral tilting, cation displacement, and structural distortions of the octahedra. Subsequent secondary distortions affect the lattice parameters and crystal system. Distorted variants, called hettotypes, thus dominate the perovskites, the majority of which are defined by tilting of the BO_6-octahedra. [27] Depending on chemical composition, ion radii and bonding preferences, a multitude of octahedral tilting patterns are possible. Cation site displacements are also common and often accompany other distortions, such as structural deformation of the octahedra.

Several systems for describing and predicting the consequences of distortions of the octahedral lattice have been devised. The most famous classification system, discussed further below, was developed by Glazer in 1972 and refined by Burns and Glazer a few decades later. [28,29] A twin classification was developed in Russia by Aleksandrov around the same time. [30] In the 1990-es Thomas and Beitollahi developed a method based on polyhedral analysis, better adapted for cases where cations are displaced from their ideal sites. Lacking a classification notation, this method focuses more on the mathematical perspective of structural analysis. [31–33]

Introducing distortions to the perovskite structure, symmetry is often reduced, and the crystal system changed. Thus, the unit cell parameters need to be expanded to accommodate the full pattern of the altered structure. For ease of comparison, a pseudocubic description with the BO_6-octahedra at the corners is used also for perovskites of non-cubic symmetries, for which other settings would be the default. This description allows the construction of a reduced unit cell, which corresponds to the

single perovskite unit cell and represents an average of the structure per would-be single perovskite formula ABO_3. In the case of double perovskites, the cation sites are assumed homogenously co-occupied for the purpose of creating the idealized reduced-cell model and calculating its unit cell parameter a_c. The reduced-cell parameters are used for comparing unit cell volume and degree of distortion from the ideal pattern of the obtained real structure. [8]

2.2.1 Octahedral tilting and the Glazer notation

Due to the interconnectivity of the BO_6-octahedra, complex patterns arise when tilting is introduced to the perovskite lattice. A notation for consequently categorizing the numerous patterns was developed by A. M. Glazer in 1972 [28], subsequently named the *Glazer notation.* Taking the ideal cubic perovskite lattice as its starting point, the glazer notation describes the aberration of the octahedra from the ideal orientation, in terms of rotations around each of the principal unit cell axes, which are defined by the crystallographic directions as $a = [1\ 0\ 0]$, $b = [0\ 1\ 0]$, and $c = [0\ 0\ 1]$. The notation is thereby locked to the atomic pattern of the structure, retaining its descriptive power for perovskites of non-cubic symmetry. As a rotation around the "a"-axis will obviously introduce a displacement of the atoms in the bc-plane, shifting the directions of the "b" and "c" axes, the tilting operations do not make an Abelian group[3]. The effects of this can, however, usually be neglected, as tilt angles in perovskites rarely exceed 15°. Beneath this limit, statistical error dominates over the imprecision of assuming initial axis orientation for each subsequent operation.

The octahedral interconnectivity means any tilt of one octahedron is constrained to introduce an equal but opposite rotation in all adjacent octahedra in the equatorial plane of the rotation. Along the axis of rotation, tilting is not geometrically enforced to propagate. Thus, the tilt propagation in each case is symbolically defined by introducing an upper index, which defines whether the tilting of the adjacent octahedron follows ("+"), reverses ("-"), or goes extinct ("0") along the given axis. With the letters for the unit cell axes a, b and c annotating the tilt around each axis, the generic Glazer notation thus takes the form $a^{\square}b^{\square}c^{\square}$. Geometrically, ten possible combinations of tilt operations are created, presented in Table 1.

Table 1. The ten fundamental combinations of Glazer tilting.

3 tilts	$a^+b^+c^+$	$a^+b^+c^-$	$a^+b^-c^-$	$a^-b^-c^-$
2 tilts	$a^0b^+c^+$	$a^0b^+c^-$	$a^0b^-c^-$	
1 tilt	$a^0b^0c^+$	$a^0b^0c^-$		
0 tilts	$a^0b^0c^0$			

[3] An abelian group is defined as a group of operations that commute, i.e. produce the same outcome regardless of the order in which they are performed.

The Glazer notation always reports the tilt of the axes in the "a, b, c" order. If the extent of the tilt is equal for several axes, the letter of the former is repeated at the position of the latter. Considering this, the number of mathematically possible tilt systems expands to 23, of which some turn out non-viable in reality. A group theoretical analysis performed by Howard *et.al* [27] reduces the number of possible tilt systems to 15, leaving out eight tilt systems found to exhibit higher symmetry than their corresponding space groups. In practice, eleven of these tilt systems have been found to occur in perovskites, of which five systems dominate by encompassing ca 97% of all tilted perovskites: $a^0a^0a^0$, $a^0a^0c^-$, $a^0b^-b^-$, $a^-a^-c^+$, and $a^-a^-a^-$, illustrated in Figure 6. Of these, $a^-a^-c^+$ appears to be the most common. [34–36]

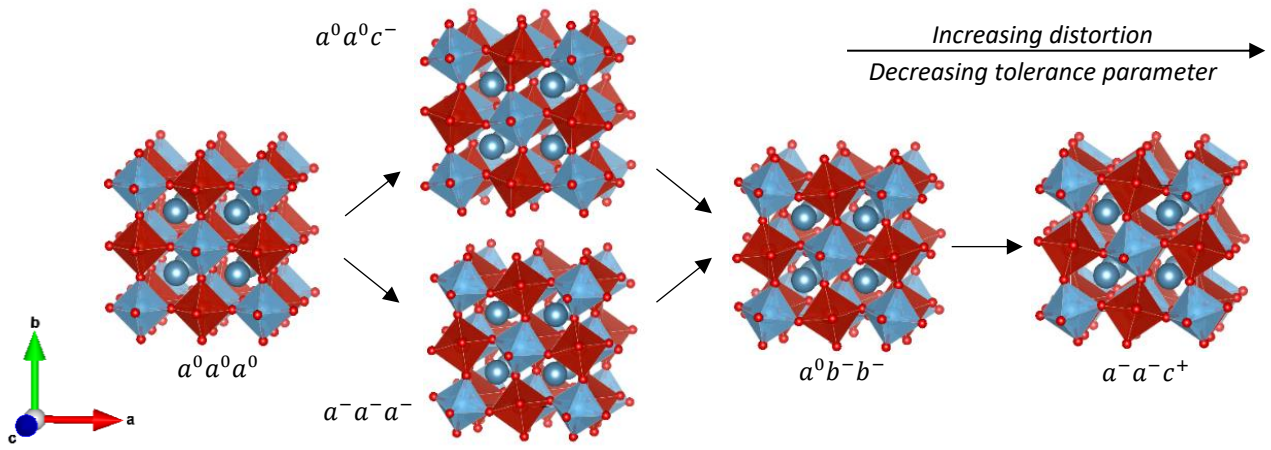

Figure 6. The five most common tilting systems, viewed at an angle along the c axis in a cubic model. These five tilting systems are interrelated by making up the most common progression of tilt systems upon increasing distortion, as determined by Vasala *et.al* [7].

The Glazer notation presents a simplified model for describing structural distortions and rearrangements taking place during phase transitions, and thus assists the prediction of phase transitions as a function of temperature or pressure. As the tilting patterns directly affect the crystal symmetry, the evolution of space group assignment with increasing distortions can be anticipated. The most common progression upon decreasing tolerance factor is shown in Figure 6. All tilt systems originate in the undistorted $a^0a^0a^0$ aristotype, from which hettotypes of increased distortion are derived. The hettotypes settle into three groups, defined by possible transitions between symmetries. These interrelationships have been explored by Howard *et.al* [27] and a schematic representation of the hettotype hierarchy is presented in Figure 7. The space group presented for each hettotype is the highest-symmetry alternative, which is often further lowered in real perovskites due to additional distortions or ordering of the cation sites.

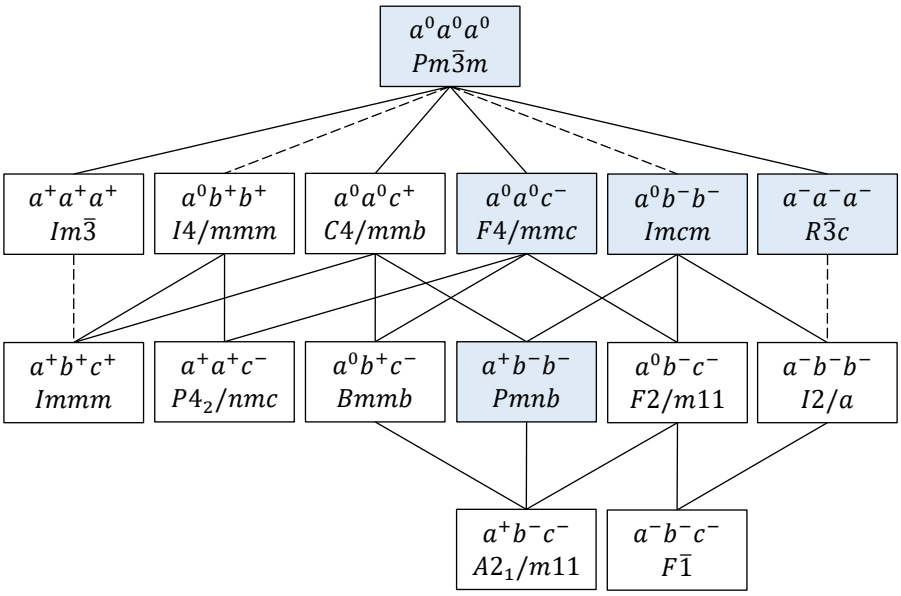

Figure 7. Interrelationships between tilting patterns with their adherent highest-symmetry space groups. Lines represent possible direct transition paths, dashed lines mark the transitions that are required to be first order based on Landau theory [37]. The five most frequently occurring space groups are marked blue. (Figure adapted from references [27] and [29] Table A9.1)

Examining the different tilt systems, a handful of shorthand rules can be formulated for determining symmetry changes and correlations between tilts and changes in unit cell parameters:

- For an axial ratio a/c < 1, two superscripts will be "+" and the third one "0"
- For an axial ratio a/c > 1, two superscripts will be "0" and the third one "+" or "-"
- For superscripts "0" and "+", all mirror planes perpendicular to the twist axis are preserved
- If two or all superscripts are "0" or "+", the unit cell will be orthogonal
- If all tilts are equal in magnitude, all principal (pseudo)axes will be equally contracted
- If all superscripts are "-", all three pseudo-axes will be inclined to one another
- With exactly two "-" superscripts, those two pseudo-axes will be inclined to each other and orthogonal to the third one

The Glazer notation is limited to tilting patterns encompassing maximum two layers of BO_6-octahedra along either crystallographic direction, and thus works best for perovskites with either homogenous or 1:1 alternating B site chemistry. For other cases, including compound tilt systems, the notation needs modifications and the descriptions become very complex; these cases are not discussed here. In itself, the Glazer notation does not consider the chemistry of the A site, but the adaption of a tilting pattern can be affected by the stoichiometry of the A site. A few of the Glazer patterns also especially support ordering of the A site by creating unequal A site environments: $a^+a^+a^+$, $a^+a^+c^-$, $a^0b^+b^+$, and $a^0b^+b^-$. [28,34–36] Factors affecting the ordering of double perovskites are discussed further in chapter 3.

2.2.2 Ion displacements and octahedral distortion

Octahedral distortions are usually secondary effects, caused by ionic displacements or bonding preferences. Both the A and B site cations can cause distortions due to preferences for bonding angles, bonding distances, and degree of covalence. Additionally, some tilting systems unavoidably introduce octahedral distortions based on geometrical restrictions, although these are rare. [38,39] One factor affecting octahedral symmetry is the electronic structure of the B site cations. Among the transition elements, partial formation of π-bonds over the B-O-B connection can stabilize 180° bonding when high charge of the B site affects the charge distribution over oxygen. However, if the B site cation is from the p-block, the availability of π-bonding is affected. In a 180° B-O-B bond with highly charged B-cations on either side, oxygen cannot be stably polarized, thereby angled bonds are favoured for maximized polarizability of the oxygen site. [7]

The Jahn-Teller (JT) effect, first described by Jahn and Teller in 1937, is an intrinsic tendency of certain ionic species to adopt asymmetric bonding environments. The effect is based on the electronic structure of the ion, which contains an unstable degeneracy. By distorting the structure, the degenerate orbitals are given different environments and the degeneracy is lifted, providing an unambiguous lowest-energy electron distribution. [40] Several transition metals present JT-active ions, famous among them are Cr^{+2}, Mn^{+3}, Fe^{+2}, and Cu^{+2}. In an octahedral environment, the d-orbitals of these ions split into two subsets: two e_g-orbitals and three t_{2g}-orbitals. Ions where the degeneracy arises from the t_{2g}-orbitals are more numerous, since the number of possible ambiguous electronic configurations is larger. On the other hand, JT-distortions caused by degenerate e_g-orbitals tend to be stronger, and more often resistant to phase transitions. Thus, high-spin and low-spin configurations of the same ion can express JT-activity of different strength depending on the environment. The difference in strength is explained by the different geometries of the orbital groups, of which the e_g-orbitals are better positioned to interact with surrounding species in the octahedral environment. Depending on the electron configuration, the JT-effect will distort the coordination octahedron, either by an elongation or by a contraction of one of the principal axes, as shown in Figure 8. Elongation of one axis is preferred in most cases, since this distortion places two of the t_{2g}-orbitals at the lowest energy level. The opposite distortion is favoured only in cases when the degeneracy is induced by a single-electron situation in the t_{2g}-orbitals, and is often very weak. There is some debate whether the appearance of square-planar coordination complexes could be modelled as extreme cases of axial JT-elongation, in which the axial bonds are discarded altogether in favour of the equatorial bonds. [41]

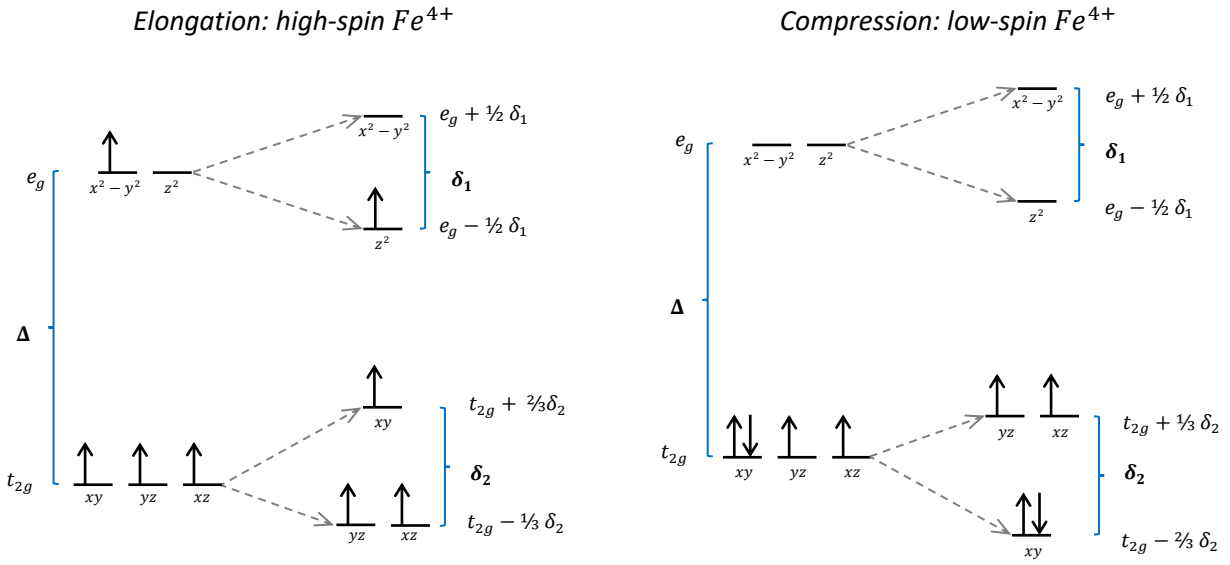

Figure 8. The effect of Jahn-Teller distortion on the electron configuration and electron orbital energies in the case of axial elongation (left) and contraction (right), as exemplified by the high-spin and low-spin versions of Fe^{4+}, respectively.

Similar effects can also be imposed on a structure externally, inducing a JT-like distortion without the presence of a JT-active ion. This mechanism holds interesting possibilities in the design of complex electromagnetic functionality, such as switchable ferroelectricity, which has been presented as a pathway for controlling magnetic order using electric fields. Since JT-distortions are linked to orbital ordering, electric manipulation of orbitals could be used to induce antiferrodistortive distortions and improper ferroelectricity, as described by Varignon *et.*al [42]. Other exotic properties such as metal-insulator transitions can also be associated with extrinsically induced JT-distortions. JT-like distortions tend to express a transition temperature T_{JT}, above which the asymmetric behaviour is lost due to thermally induced rapid fluctuations of the direction of distortion. [43]

Ferroelectric cation displacement is another intrinsic effect caused by the electron configuration, which can arise from a lone electron pair effect. Among the p-block semimetals, several ions present a lone s-electron pair in its valence shell, for example Pb^{+2} and Bi^{+3}. Due to the lone electron pair, a spherical description of the ion is no longer valid. Adjusting the bond lengths to minimized energy creates an asymmetric environment, which in the octahedral coordination expresses as an elongation of one axial bond and out-of-plane displacements of the equatorial bonds. When the charge environment of the BO_6-octahedron is no longer symmetric, the material becomes polarizable. Simultaneously, the octahedron affected can be geometrically distorted. [44] Whether a material containing polarized octahedra can express overall polarizability is dependent on the overall

symmetry of the structure. Thus, the Glazer tilting systems can predict the appearance of physical properties to some extent, in cases where the behaviour depends on crystal symmetry.

Geometrical distortions of the octahedra can also be induced by the A site cation in cases where A is undersized and tolerates reduced coordination numbers. Tension on the A-O bonds caused by the small A ion can displace the oxygen ions to enable shorter A-O bonds, in exchange for a reduced coordination. Most frequently CN(A) is reduced from 12 to 8, but in certain extreme cases square planar coordination can appear. The appearance of square planar A sites is more favoured in certain tilting systems, such as $a^+a^+a^+$, where ¾ of the A sites can become square planar if the tilting is large enough. [44] On the other hand, the larger the A cation, the more flexible the bonding to oxygen, allowing compounds with larger average cation radii to better compensate for mismatches and retain a more symmetric structure. Thus, octahedral distortions due to bonding preferences are more frequent in compounds of lower atomic weight. [7]

3 Cation ordering in B site ordered double perovskites

When introducing substitution at a given site in a structure, the baseline assumption is a random but overall homogenous distribution of the substituent element. For certain combinations and suitable stoichiometric ratios of co-occupants, ordering into long-range regular patterns may appear. Various patterns are possible at both the A and B cation sites, and can appear both independently and in a mutually reinforcing manner. Driving forces for the splitting of a crystallographic site into two or several unequal sites are Coulombic repulsion, ion size differences, and bonding preferences. At the B site, the two first dominate the ordering dynamics, while A site ordering is strongly affected by bonding preferences and bonding symmetry. This is one reason why the B site adapts ordered patterns considerably more willingly than the A site. [44]

Assuming a 1:1 occupation ratio of a binary occupied cation site, there are three fundamental patterns for cation ordering in the cubic perovskite lattice. In a rock salt (RS) arrangement, the elements alternate in all three directions, thus the pattern can be interpreted as zero-dimensional (0D). Layers of same-species sites alternate along the $[1\ 1\ 1]$ direction. Similarly, the columnar pattern (1D) alternates along the $[1\ 1\ 0]$ direction, and the layered arrangement (2D) alternates only along $[1\ 0\ 0]$. [44] The patterns are presented in Figure 9.

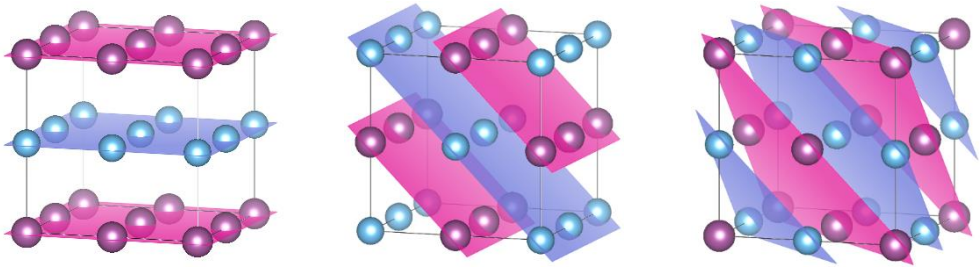

Figure 9. Regular ordering patterns for 1:1 B site ordered double perovskites. From left to right, layered, columnar, and rock salt (RS) patterns, with elemental alternation following directions $[0\ 0\ 1\ ]$, $[0\ 1\ 1]$, and $[1\ 1\ 1]$, respectively. Crystallographic lattice planes are shown to emphasize the geometry of the patterns.

Among the B site ordered double perovskites, the RS pattern of ordering dominates overwhelmingly. The number of RS-ordered $A_2B'B''O_6$ compounds is so large that they have been defined as a separate subclass of perovskites, called *elpasolites*. [1] The high occurrence of the RS pattern arises from cooperative contributions of Coulombic forces and ionic radii. Unless the charge difference between the two B site occupants is negligible, electrostatic repulsion will promote an arrangement that maximizes the distance between the stronger charged species. Similarly, ions of notably different sizes will generate lattice strain, which is relieved by minimizing the number of similar species in neighbouring octahedra. Mostly due to the induced lattice strain, very few compounds express the layered arrangement and even fewer are columnar, as both arrangements require deformation of

the octahedra. All compounds expressing the layered arrangement have been found to contain a JT-active species or other special behaviour. Only one case with columnar arrangement has been found, allowing very few conclusions to be drawn. The compound in question also expresses doubling of the A site, which can affect B site order. [7]

Ordered phases of 2:1 or higher molar ratio on the B site are significantly less common than the equimolar elpasolites. Arrangements mimicking the RS-order are encouraged by the same mechanisms, promoting the formation of layers along $[1\ 1\ 1]$. Phases where the minority species is the stronger charged dominate, the most common charge distribution being $A_3^{+3}B'^{+2}_2B''^{+5}O_9$. With a 2:1 stoichiometry, layer sequences of B'-B'-B" are stabilized by the presence of B cations supporting octahedral distortions, such as JT-active species and concerted cation displacements in the majority layers. Another possibility is the formation of regular RS-order, where one site is purely occupied by the majority species and the other dominated by the minority species. The mixed-chemistry site is rarely ordered within itself. The highest ratio for which long-range order appears is 3:1, which tends to adapt arrangements with alternating majority-pure and disordered, 1:1-mixed layers. The incentive to order is, however, weaker than for the lower ratios. [36,44]

Introducing order at a split crystallographic site will inevitably have consequences for the symmetry of the crystal. As the appearance of order introduces an inequality of the sites, symmetry elements relating neighbouring B sites are destroyed and symmetry is lowered. With respect to symmetry, the introduction of RS-order at the B site is directly comparable with the introduction of octahedral tilting patterns. As discussed previously in Chapter 2.2.1, octahedral tilting introduces equal alteration of every second octahedron along each plane of twisting, giving rise to a RS-pattern of equally vs oppositely twisted octahedra. This has been well illustrated above in Figure 6, where the orientationally unequal sites have been given different colour. Just as in the case of tilting patterns, all space groups appearing for ordered perovskites are subgroups of the aristotype space group $Pm\bar{3}m$, which in the very simplest case of B site splitting into an untilted RS pattern is automatically transformed into $Fm\bar{3}m$. [38]

Whether B site order is favourable or not can be predicted by so-called stability field maps, as developed by Davies *et. al* [44]. Similar in idea to the maps predicting perovskite formability, the stability field maps are drawn up by plotting the charge difference against the size difference of the two B site species. Different stoichiometries and arrangement patterns present different requirements for favouring order, giving each stoichiometry its own map. The cooperative behaviour of charge difference and differing ionic radii shows especially well in the stability field map for 1:3 stoichiometry, in which the lower limit for ordering is a slope (Figure 10).

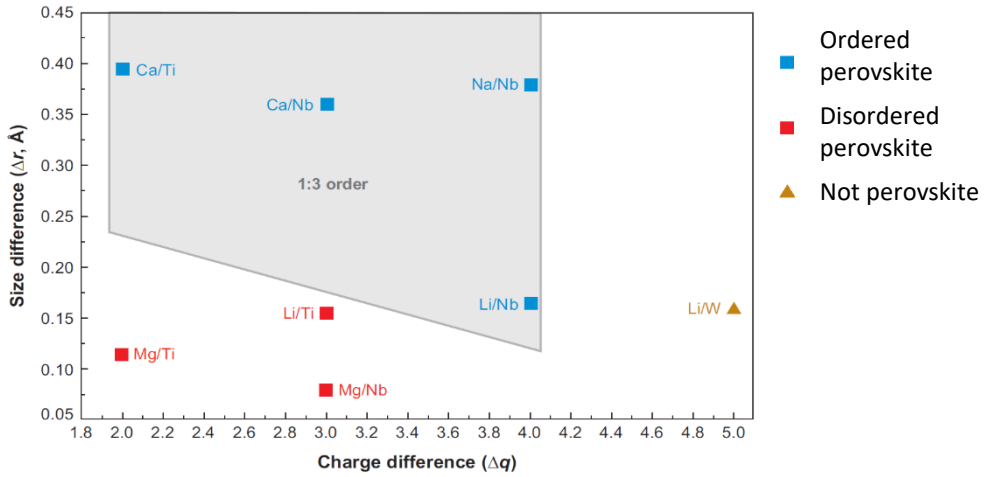

Figure 10. Stability field map for B site ordering with 1:3 B site stoichiometry. The cooperative influence of charge difference and size difference is evidenced by the tilted lower limit of the ordered zone (grey). Labels annotate B site chemistry of the perovskite-suitable stoichiometry. (Reprinted: ref [44] Figure 21)

The presence of B site ordering can be evaluated by X-ray diffraction (XRD), by checking for specific reflections only present in the XRD patterns of ordered compounds. Namely, the $(1\ 1\ 1)_c$ reflection, which in orthorhombic setting is equivalent to the $(1\ 1\ 0)_{or}$ reflection family, is allowed only in RS ordered compounds, which belong to space group $Fm\bar{3}m$. In disordered compounds, this reflection goes extinct due to the increased symmetry of the simplified structure, which can be modelled as a single perovskite of space group $Pm\bar{3}m$. A weakness of the method is the small risk of mistaking a disordered compound for an ordered one if the compound expresses strong octahedral tilting, since this induces RS-patterning of the BO_6-octahedra by geometry. The effect is, however, much weaker than with true B site ordering, and can be ruled out if the expected phase has a high tolerance parameter. [36]

3.1 Degree of order

The discussion has thus far assumed long-range ordering to be perfect and complete. In most cases, however, ordering will be disrupted by defects, divided into domains, or partially inhibited by kinetic and thermodynamic effects. Depending on the stoichiometry and pattern of ordering, the incentives for ordering vary in strength. The overall degree of ordering is expressed by the order parameter S, defined in Equation 7, in which $g(B)$ describes the amount of B cations holding correct site occupancy. At perfect disorder, half of the B ions will have taken the wrong site and the equation yields zero, while S=1 annotates perfect order.

$$S = 2\,g(B) - 1$$ Equation 7

The dominating driving force for ordering at ambient conditions is charge difference. Electrostatic repulsion is expressed by the Madelung energy, which is proportional to the charge difference squared. Thus, with increasing charge differences at the same crystallographic site, electrostatic repulsion quickly becomes a dominating contributor to the total energy of the system. Considering RS-ordering with a 1:1 compositional ratio on the B site, order is always favourable when the charge difference is larger than two. With a charge difference of precisely two, about half of the phases are ordered, with ion sizes difference stepping in as a second promotor for ordering. As these incentives are cooperative, a precise value for the necessary size difference cannot be defined. The prevalence of order increases gradually between 7% and 17% differing radii and a charge difference of two. A size difference of 35% compared to the smaller ion practically renders disorder impossible, even when the B site species have the same charge. [7,44]

For phases with 1:2 and 1:3 stoichiometry, order is induced by the same mechanisms as for 1:1 stoichiometry, but stronger incentives are needed. The notably lower prevalence of ordered phases impedes precise determination of threshold values for charge and size differences, but charge differences of minimum three appear to be necessary. Additionally, geometric considerations weigh in, and other effects might dominate the ordering incentive, such as the availability of concerted cation displacements and asymmetric bonding. The predictive power of the tolerance factor is also altered the more complex the stoichiometry of the doubled site becomes. [44]

The kinetic and thermodynamic prerequisites for the appearance of cation order are diffusion and entropy. With increasing temperature, diffusion is promoted, but entropy is simultaneously increased. Two critical temperatures for order-disorder phase transitions can thus be found: the kinetic limit T_k presents the temperature below which diffusion of at least one of the species is inhibited by lack of thermal energy, and the entropic threshold T_S sets the maximum temperature above which entropy will overpower the incentives for ordering. Combining the kinetic and entropic limits for ordering, three possibilities present themselves: 1) highly ordered at all temperatures when $T_k \ll RT \ll T_S$; 2) controllable ordering when $T_k < T_S$ and both fall within a manageable temperature range, and 3) permanently blocked with $T_k > T_s$ at any temperature. In the second regime, final degree of ordering can be controlled by synthesis conditions and thermal treatments. [7,45] These mechanisms have been thoroughly investigated by Sahknenko and Ter-Oganessian [46], and developed into a statistical method for predicting which of the three groups a given composition

will belong to, and at what temperature range ordering could be expected, taking into account that both T_k and T_S are sensitive to pressure. The effects of pressure are returned to in Chapter 3.4.

The kinetic limit for ordering is strongly linked to the physical barriers for diffusion, and thus strongly influenced by the relative ionic sizes and distortedness of the phase. A smaller species on the A site provides less of a barrier for diffusion between the B sites, lowering the energy barrier for neighbouring B cations to swap sites. Simultaneously, a smaller A site cation forces the B sites closer together which enhances the effect of charge differences. Reducing the tolerance parameter by A site substitution can thus promote ordering at the B site, but has the side effect of increasing distortions and altering bond angles and symmetry of the phase, in a similar manner to the application of pressure (further discussed in Chapter 3.4). [7] As different synthesis methods provide different kinetics and growth mechanisms, choice of synthesis method can sometimes influence the formation of cation order. However, since the differences in phase formation mechanisms are multiple and their interactions unkclear, the precise effects of method choice cannot yet be well predicted.

Bonding preferences can support ordering, for example if one of the site co-occupant is noticeably more electronegative, in which case ordering will lessen bond strains by allowing polarization of oxygen. Adverse effects are however also possible, as competing phases with the same stoichiometry can provide a preferable bonding environment for some compositions. One example is the pyrochlore phase, which appears as a growing impurity with increased synthesis time and thus presents an unwanted side-effect of the synthesis conditions needed for allowing cation order to appear. Substitution of one cation site can alter the bonding structure on the other by the same mechanism of electron competition, since effective electronegativities are influenced by the electronegativity of nearby atoms. This effect can be seen e.g. in the sister perovskites Ca_2MnWO_6 and Sr_2MnWO_6, in which the longer Mn-O bonds are found in the Ca-compound. [47] Another bonding effect can be seen in the case of oxygen deficient phases, where the species more tolerant of reduced coordination tends to accumulate on sites adjacent to the vacancy, mutually reinforcing long-range patterns of vacancies and cations or the formation of domains. [48,49]

3.2 Ordering defects

The nucleation and growth of the ordered phase follows the same thermodynamic principles as other phase transformations. Order expresses a preference for growing along the $[1\ 1\ 1]$ direction of the pseudocubic setting. This is explained by the geometry of the direction, as every site ‘next up’ is surrounded by three already-ordered adjacent sites. A direct consequence of phase nucleation is the

formation of inverse order domains, called antiphase domains. These can form based on either ionic site distribution or octahedral tilting patterns, or both, in which case domain boundaries tend to coincide. This type of defect system has been experimentally observed and investigated in Sr_2FeMoO_6 [50], in which the degree of ordering can be controlled by adjusting the cooling rate during synthesis. The defect type associated with the antiphase domains is the antisite border, at which the lattice strain is increased by the pairwise arrangement of similar B sites. If diffusion is not kinetically blocked, antisite switches can appear and drive the minority phase towards extinction over time. The higher the phase boundary energy, the stronger the incentive to convert the minority phase. Perovskites with B site cations differing drastically in both size and charge can be assumed practically antisite-free. When ordering is interrupted prematurely, for example by rapid cooling, superstructures containing various degrees of ordered zones inhabiting an overall disordered structure can form. The ordering parameter S does not distinguish between such ordered/disordered compound phases and phases rich in antisite defects or domains. [50,51]

Isolated instances of pairwise switched sites, called antisite defects may also appear by thermal excitations, or as stacking faults during phase formation. An isolated antisite defect causes notable strain on the lattice, driving an alternative route for antisite domain formation via defect clustering. [52] If the lattice strain is too high and diffusion rates too low, this behaviour can however be blocked, stabilizing the appearance of antisite point defects even in the most readily ordered elpasolites.

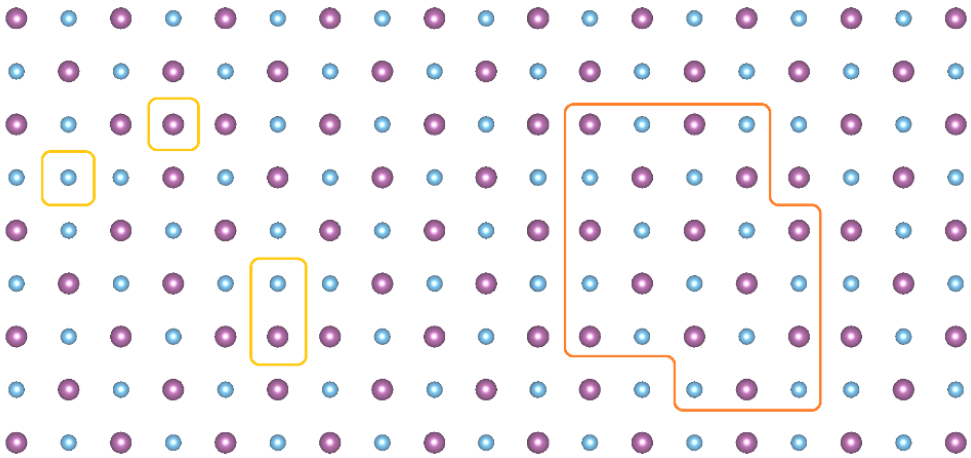

Figure 11. 2D depiction of ordering defects in double perovskites. To the left, two antisite defects encircled in yellow. To the right, an antiphase domain encircled in orange.

As with all crystalline solids, classical defects such as Schottky defects and Frenkel pairs will occur in perovskites, presenting a pathway to the occurrence of ordering defects. Antisite defects also take place between the A and B sites, although in noticeably lower rates than within either site. The

mechanics of site swapping have been most closely studied in phases where antisite defects are of harm, such as $Pb(Zr,Ti)O_3$.[53] The formation of cation antisites from Frenkel pair defects has been modelled in $BaTiO_3$ and $SrTiO_3$ [52]. Site swapping can also occur because of bonding preferences when ion sizes are suitable. A sample series where site redistribution is induced by substitution is $BaLaB'TeO_6$ with $B = Na \rightarrow K \rightarrow Rb$. The substitution results in La^{+3} relocating to the B site as the average radius of the substitute species increases and exceeds the radius of La^{+3} itself. [54] True cation mixing is seen in Ca_2LnRuO_6 with $Ln = Y, La - Lu$, where the entire series of Ln^{+3} ions expresses willingness to mix with the A site. Across the series, the extent of Ca^{2+}/Ln^{3+} site swapping follows a radius-dependent trend with a large change in preference towards the B site taking place over $Tm \rightarrow Er \rightarrow Y \rightarrow Ho \rightarrow Dy \rightarrow Tb$. [55,56]

Domains of differing composition can form when segregation is energetically favoured. An altered chemistry on the A-site, discussed further in Chapter 4.1, can be a driving factor. In $ATiO_3$ with the A site divided between Li^+, Nd^{3+}, and vacancies V_A'', domains of $LiNdTi_2O_6$ and $Nd_2V_A''Ti_3O_9$ tend to form in a ratio determined by the A site chemistry. The domain distribution arranges into a superstructure with nanometre-scale features and long-range checkerboard-type pattern, the periodicity of which can be tuned by adjusting the A site stoichiometry. [57]

3.3 Charge disproportionation and charge ordering

Charge disproportionation is a rare behaviour seen only for a handful of ions, for example Fe^{+4} and Au^{+2}. Both have a charge in between two oxidation states with energetically more optimal electron structures, sufficiently lower in overall energy to counterbalance the increased Madelung energy of disproportionation. Ions with electronic structures close to d^0, d^5, or d^{10} occupancy are more susceptible to charge disproportionation due to the energetic benefits of d-orbital contraction. Crystal field splitting induced by the coordination environment can promote charge disproportionation as a way of avoiding energetically unfavourable Jahn-Teller distortion. This is an especially strong driving factor in the case of gold. Thus, phases formally containing iron or gold ions with the aforementioned charges are likely to actually present equimolar amounts of $Fe^{+3/+5}$ and $Au^{+1/+3}$ ions. [36,41,58]

Charge ordering appears fast, and readily adapts long range ordering when the conditions are favourable. Atomic diffusion is not required, but minor structural adjustments might occur to accommodate changing ionic radii. With no need for diffusion, the lower kinetic limit does not apply. Instead, the lower thermal limit is defined by the energy barrier of tunnelling between cation sites.

The upper limit of ordering, founded in entropy, remains relevant for charge ordering, cancelling out charge differences when thermal excitation rates become too high. For example, the charge disproportionation of $CaFeO_3$ only persists up to ca 17°C (290 K), above which all iron cations express equal charge of +4. The related phases $CaCu_3Fe_4O_{12}$ and $LaCu_3Fe_4O_{12}$ present similar, temperature-dependent charge disproportionation of iron. [36,59,60] Driven only by electrostatic repulsion, charge ordering always takes on the rock salt pattern in cubic lattices.

In double perovskites with different elemental ions sharing the B site, charge disproportionation can have curious consequences for cation ordering. In Ca_2FeMnO_6 [49], iron has an overall charge of +4 and disproportionates spontaneously to $Fe^{+3/+5}$. With the B site occupied by two different elements with noticeably different ion radii, an RS-ordering between the two would be expected, but due to the charge disproportionation a layered order is instead preferred. The explanation lies in the charge distribution, which is the most homogenous when the $Fe^{+3/+5}$ ions are concentrated into layers of chequered order. If the B site was to adopt an RS-ordering, a homogenous charge distribution would be geometrically impossible.

Charge transfer reactions do not need to follow integer values. For example, $BaBiO_3$ [58,61], $CaFeO_3$ [62], and $YNiO_3$ [63] all present partial disproportionation of the B site ion, with a clear splitting into two electronically unequal sites of non-integer charge. In fact, a majority of charge disproportionation cases result in non-integer charges, and charge transfer can also take place between elementally different species at the B sites. Several compounds express mixed-valence oxidation states, which can be interpreted as a case of partial charge transfer between the B site species. The amplitude of the charge transfer varies with degree of elemental ordering. One example is the double perovskite La_2MnCoO_6, which experiences partial-to-complete charge transfer, from near complete Co^{+2}/Mn^{+4} in the ordered case to a charge distribution much closer to Co^{+3}/Mn^{+3} in the disordered case. [45] Similarly, in Sr_2FeMoO_6 the valence of iron fluctuates with the degree of ordering of the local environment. Antisites and antiphase boundaries consequently present Fe^{+3}/Mo^{+5} while the ordered regions show various levels of $Fe^{+2/+3}/Mo^{+5/+6}$ valence mixing. The change in charge distribution drives a structural transition from cubic to tetragonal when the molybdenum content is increased from 25% to 33%. [64–67]

3.4 Physical and chemical pressure

The effect of external (physical) pressure on the perovskite structure can be described in terms of an alteration of the tolerance parameter. As mentioned, the rigid-sphere model assumed for calculating

the tolerance parameter is not strictly correct, and the effective ionic radii shrink when the structure is compressed. Due to their electron structure, larger ions are more easily compressed than smaller ones, and thus application of an external pressure can act to lower the effective tolerance parameter when A site ions are compressed more than B site ones. By this mechanism, compositions with tolerance parameters above one, that form hexagonal phases at ambient conditions, can in some cases form a cubic perovskite phase if subjected to high pressure. [16] Similarly, distortion systems are affected by pressure, as the internal proportions between bond lengths are altered. As bond compression depends on both bond participants and the magnitude of the applied pressure, the effect of pressure on distortive behaviour is extremely difficult to predict. Whether pressure will increase or decrease distortions is currently best predicted by assessing the chemical nature of the bond participants. Most phases will distort more under pressure as the effective tolerance parameter is decreased. Phases containing asymmetric ions, such as Jahn-Teller active cupper, are more likely to adapt less distorted structures under pressure as the asymmetric ion is forced to adopt a more symmetric environment. [7]

Due to differences in preferred bond lengths, external pressure can sometimes assist the appearance of cation order within the $B'B''O_6$-lattice. Chemical bonds tolerate stretching better than compression, so in a disordered lattice, minimal lattice strain is more easily achieved by stretching the bonds between adjacent smaller B site ions, rather than compressing the bonds between adjacent larger ones. This results in a natural contraction of the unit cell parameters when a phase becomes ordered. The phenomenon is bidirectional, as further compression of the bonds between adjacent large ions will significantly enhance the incentive for ion size-driven ordering. On the other hand, compression of interatomic distances counteracts ordering by hampering diffusion, which relies on sufficient interatomic space. Added together, these effects allow only a small number of cases where moderately applied pressure can contribute to the appearance of B site ordering. [68–70]

Although bonds prefer stretching over contraction, stretching of bonds will give rise to a counter-force directed towards contracting the bond back to its optimal length. In a lattice of stretched-out bonds, the forces of all stretched bonds add together to form an intrinsic, contractive force known by the term *chemical pressure.* Chemical pressure can act similarly to an external pressure in terms of influencing structural distortions, cation ordering, and magnetic interactions (discussed further in Chapter 5). Contractive lattice strain is regularly introduced in perovskites as A site substitution, introducing a smaller but equally charged cation to a fraction of the sites. Common substitution pairs are Na^{+}/K^{+}, Ca^{+2}/Sr^{+2}, and Sr^{+2}/Ba^{+2}. [71,72]

Although assumed similar in all aspects except for size, there are always some differences in chemical behaviour between substitution pairs, such as electronegativity and bonding. This can have noticeable influence on the physical behaviour of the material. One such example is the $Ca^{+2}/Sr^{+2}/Ba^{+2}$ trio, in which barium has a notable preference for higher-symmetry structures as compared to strontium, which in turn promotes higher symmetry than calcium. When seeking to alter crystal structure by substitution with this pair, this effect can potentially obstruct analysis by introducing uncertainty as to whether the phase transition observed is more dependent on changed tolerance parameter, or different bonding preferences. [73,74]

4 Non-stoichiometry

4.1 A site substitution and ordering

Altering of the A site stoichiometry is a common trick for tuning the tolerance parameter and thereby octahedral tilting patterns of perovskite phases. Although this act technically splits the A-site, it is often assumed to remain homogenous if the applied stoichiometry does not present low-integer ratios that would promote ordering. This is especially the case when the functional behaviour stems from a doubled B-site and its degree of ordering, in which case the 'starting point' stoichiometry is often described as being doped at the A site by the other species. This kind of doping is often done assuming the default and dopant ions are identical in all aspects but size, as mentioned above in Chapter 3.4. However, as differences between even the most similar pair of ions do go beyond size, the effects of substitution also go beyond simple alteration of the geometrical parameters of the phase. Even the most chemically similar pair of ions, take the commonly used Ca^{2+}/Sr^{2+} or Sr^{2+}/Ba^{2+} pairs for example, will at the very least differ in electronegativity in addition to ionic radius. This influences the bonding of the entire phase, as Coulombic repulsion is a determining factor for electron mobility. [75] Additionally, the assumption of retained homogeneity of a doped A site hides behind it the real possibility of ordering of the A site species. Since electrical conductivity is also promoted by regular patterns of the electrical potential, A site ordering can influence the electromagnetic behaviour of a phase even when the A site is assumed not to contribute.

Unlike the B site, the A site does not prefer 1:1 stoichiometry for ordering, but rather prefers 1:3 stoichiometry. The fundamental difference between the A and B sites regarding ordering aptitude lies in their bonding to oxygen. Each oxygen ion is surrounded by two axially placed B cations and four equatorially placed A cations. With an ordered B site, the RS pattern allows the intermediate oxygen to find its optimal distance to each B ion along the B'-O-B'' line in every direction. However, the same ordering at the A site would place oxygen in an inversion-symmetric square planar arrangement. In this geometry, finding a position with optimal bonding distances to both species simultaneously is impossible. This makes RS-ordering at the A site highly unfavourable, effectively blocking its appearance in the real world. A similar situation appears for a large fraction of the oxygen sites in a columnar pattern. Thus, the A site strongly prefers a layered arrangement. [36] The comparative rarity of B site ordered perovskites with stoichiometry other than 1:1 can be similarly explained, as other ordering patterns create unequal environments for the A site, as well as several different oxygen environments. [44]

With a substituted A site, unequal A sites can become favourable. Certain octahedral tilting patterns especially promote ordering of differently sized A site ions, due to the strong effect of tilting on the bonding distances. Often, one site is singled out for being notably larger than the others, explaining the relatively high preference of the A site to order in a 1:3 stoichiometry. Four systems have been found to stabilize A site ordering, as mentioned in Section 2.2.1, by creating A sites of considerably differing size. The four systems supportive of A site order, $a^+a^+a^+$, $a^+a^+c^-$, $a^0b^+b^+$, and $a^0b^+b^-$, are presented in Figure 12 with the differently sized A sites highlighted. [36]

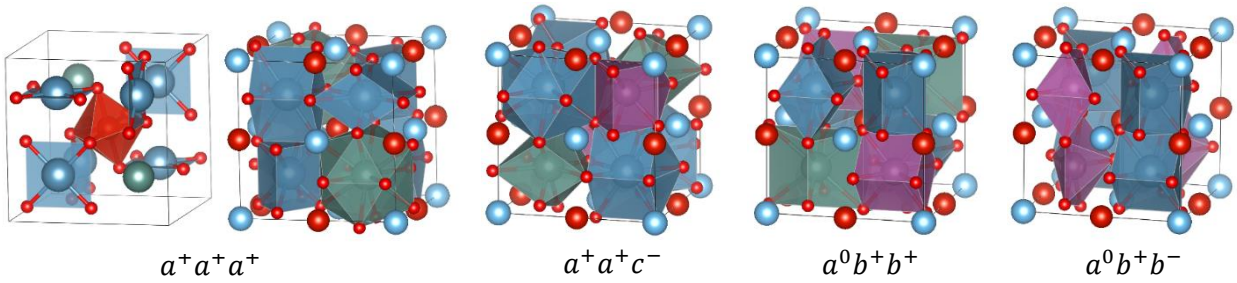

Figure 12. The four Glazer tilting systems promoting A site order. Polyhedra depict the A site environment as drawn up by the closest situated oxygen sites, with different colours representing differently shaped sites. The reduction in coordination number with shrinking bonding distances to oxygen is clearly visible, and shown especially for the $a^+a^+a^+$ system (leftmost) in which severe tilting can effectively reduce the coordination of ¾ of the sites to square-planar coordination, while the fourth site remains a perfect icosahedron for a perfectly cubic phase.

Co-substitution can stabilize ordering at both sites simultaneously, as A site ordering and RS-ordering at the B site can reinforce each other through enhanced octahedral tilting systems. Generally, the B site orders more easily, enhancing the incentives for ordering at the A site. Co-ordering is most common for 1:3 + 1:1 stoichiometry, in which case the B sites prefer RS ordering and the A site a body centred cubic (BCC) pattern for the minority species. Examples include $CaCu_3Ga_2Sb_2O_{12}$ and $CaCu_3Cr_2Sb_2O_{12}$ [36], and $CaCu_3Fe_2Sb_2O_{12}$ [76], the last of which is also a rare example of the A site ordering more readily than the B site. For 1:1 stoichiometry, columnar ordering can be promoted by the $a^0b^+b^-$ tilting pattern, while layered ordering is to be preferred in very weakly tilted or untilted structures.

4.2 Oxygen stoichiometry

The perovskite tolerance for variations in stoichiometry extends further than simple substitution of atomic species. All sites tolerate varying types of deviations in stoichiometry, mainly vacancies and substitution, but the oxygen site is especially flexible in accommodating vacancies. In fact, most perovskites phases contain less oxygen than indicated by the reported formula. Oxygen deficiency is

especially common in phases incorporating cations with several preferred oxidation states, as these give the phase flexibility regarding charge distribution. The oxygen content can have significant influence on properties, especially electromagnetic behaviour and ion conductivity, and is therefore an important parameter in perovskite chemistry. Oxygen intercalation/elimination reactions in perovskites can occur at temperatures as low as 100-300°C, considerably lower than the ca 1000°C temperatures regularly needed in perovskite synthesis. [77] Final oxygen content of a perovskite mainly depends on two parameters during synthesis: oxygen availability and cooling rate. Most perovskites are synthesized in solid state surrounded by a gas atmosphere, in which case oxygen content is controllable by directly adjusting the oxygen partial pressure of the synthesis atmosphere. In closed system syntheses, an oxygen donator material such as $KMnO_4$ must be added. When using encapsulated synthesis methods, excess oxygen can be removed by reducing gases such as H_2 or Ar, or by sacrificial materials such as elemental carbon. [8]

The oxygen non-stoichiometry of perovskites has been intricately studied in $SrCoO_{3-\delta}$, in which cobalt readily transitions between Co^{2+} and Co^{3+}. With decreasing oxygen content, the symmetry of the originally cubic phase changes to tetragonal and then orthorhombic, with maximal oxygen deficiency $\delta \approx 0.7$. Investigations have shown that the oxygen intercalation/elimination reaction follows a gas intercalation mechanism mediated by the oxygen vacancy network. Upon entering the material, O_2 is first converted to superoxide O_2^-, and then reductively split and incorporated in the perovskite structure. Thus, the oxygen content varies with depth in oxygen deficient grains, leaving the core closer to $SrCoO_3$ in stoichiometry than the surface. [77,78]

Anion site vacancies can induce accumulation of the more vacancy-tolerant cation species into patterns when the site-sharing species have different bonding preferences. *Brownmillerite* ($A_2B_2O_5$) can be seen as a limit case for oxygen vacancy ordering into alternate BO_3-planes, with alternating rows of oxygen missing along $[1\ 0\ 0]$. This strongly promotes a layered order in case of two different B site species. [48,49] Severe oxygen deficiency in $SrCoO_{3-\delta}$ leads to the formation of a brownmillerite phase at $\delta = 0.5$, which can be converted to a perovskite by heating in a strongly oxidizing environment. [79] Sub-brownmillerite levels of oxygen leads $SrCoO_{3-\delta}$ into a nanostructured arrangement of brownmillerite-like domains. [78]

Reversible oxygen uptake/release can be used for oxygen storage in solid materials. Several perovskites express promise for this application, among them $LaCoO_3$ and doped or undoped $LaMnO_3$. The flexibility in oxygen content allows for both deficient and overloaded states, depending on the elemental composition. $LaMnO_3$ can support both cases, depending on the dopants at the A

and B sites. [80] For example, B site Rh-doped $LaMnO_{3+\delta}$ can accommodate up to $\delta = 0.15$ of excess oxygen by means of a small structural change, which is reversible at 400°C. [81]

Oxygen vacancies can sometimes co-exist with cation vacancies. Ordered and stoichiometric B site vacancies supported by oxygen vacancies present as layered absences in quadruple perovskites $A_4B'B''_2O_{12-\delta}$, named the *12L perovskites*. The structure of the 12L phase is that of a layered B site ordered double perovskite, in which alternating B' layers are vacant. [82] The structure can also form in a hexagonal polymorph [83] and take on various other periodicities [84].

5 Magnetic properties

The cubic or near-cubic perovskite structure provides an excellent template for tuneable magnetic interactions. With highly substitution-tolerant cation sites situated at a suitable distance of ca 4 Å from one another, the number of possible combinations of magnetic and non-magnetic ions is vast, enabling a wide spectrum of different magnetic arrangements and behaviour. Magnetic interactions can occur between so-called Kramer's ions, i.e. ions containing unpaired electrons, giving the ion a nonzero magnetic moment. [85] Both the A site and the B site can hold Kramer's ions, but due to the wider range of allowed oxidations states, the number of magnetic ions available for the B site is considerably larger.

Interactions between nearby situated spins allow cooperative magnetic behaviour to manifest. Electron spin interactions appear from the combined effects of Coulombic repulsion and the Pauli principle, dictating that no two electrons can share the same quantum state. There are four fundamental regimes of spin alignment and overall magnetic behaviour: 1) *ferromagnetic* (FM) materials contain all-parallel alignment of unpaired spins, and produces an intrinsic magnetic field; 2) *antiferromagnetic* (AFM) ordering results in zero net magnetization, as equal numbers of parallel and antiparallel spins cancel each other out; 3) in *ferrimagnetic* (FiM) materials a part of the spins are arranged antiparallel to the rest, but do not cancel out; and 4) *paramagnetic* (PM) behaviour appears when all spin interactions are too weak to induce alignment between neighbouring spins. [86]

The division of the magnetic ordering regimes into four main systems is practical when discussing only external qualities of materials, but becomes insufficient for the purpose of designing and controlling the finer magnetic interactions of novel materials. On the atomic scale, endless variations in spin alignment patterns and magnetic behaviour are possible, and depend on lattice topology and the extent of elemental order in the material. The selection of spin alignment patterns presented below constitutes only a part of all possibilities, encompassing the systems most relevant for the perovskite and elpasolite lattices.

5.1 Magnetic ground states

The preferred magnetic pattern in a phase is called its *ground state*. Ferromagnetic alignment is the simplest ground state, expressing variation only in the extent of alignment and elemental composition. As all aligned spins are unidirectional and mutually reinforcing, net magnetization is the sum of the aligned partitions of all contributing spins, regardless of the chemical identities of the

contributing species. The FM ground state can thus include either one or both B subsites, with the former case being more common due to the rarity of FM coupled ion pairs. One example of an FM compound is La_2ZnMnO_6 [87] (Figure 13, left) which holds only one magnetic B site species.

Ferrimagnetic alignment follows lattice topology and elemental composition in determining which part of the spins will be arranged parallel, and which will be antiparallel. The majority of FiM compounds contain magnetically unequal atoms or ions with oppositely arranged spins. As the magnetic moment of one species is larger than that of the other, they generally do not cancel out despite the opposing alignment[4], such as in La_2NiIrO_6 [88], shown in Figure 13. In materials containing only one magnetically contributing element, unequal lattice sites can induce unequal distribution of spins. FiM behaviour in Pb_2FeNbO_6 and Pb_2FeTaO_6 arise from magnetically equal Fe^{3+} ions, which add up to a FiM behaviour due to the geometry of their partially ordered arrangement[5]. [89] The most famous ferrimagnet, spinel magnetite Fe_3O_4, is a mixture of the two cases. In magnetite, iron is distributed over two different sites at a ratio of 1:2 in which it expresses different oxidation states, and thereby different magnetic interactions. [86] In some cases, FiM can be canted, leading to a weak net magnetization perpendicular to the axis of opposed alignment.

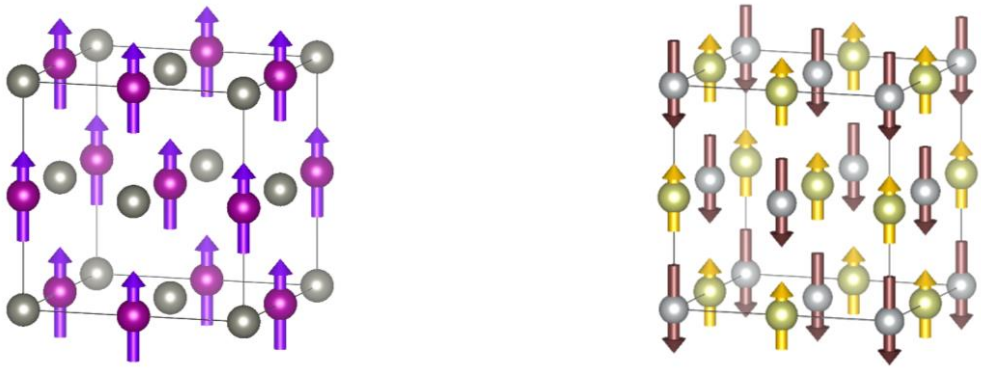

Figure 13. Model visualizations of FM (left) and FiM (right) ground states. The FM ground state is shown for La_2ZnMnO_6 in which only Mn^{4+} is magnetic, and the FiM ground state for La_2NiIrO_6 in which oppositely aligned Ni^{2+} and Ir^{4+} do not cancel out. For clarity, only the B site cations are shown. (Figures drawn based on refs [87,88], respectively.)

Antiferromagnetic (AFM) alignment is reminiscent of FiM, but the oppositely arranged spins are equimolar and of the same species, leading to a perfect cancelling-out of the net magnetic moment. Depending on lattice, AFM can take on a multitude of different up/down patterns called *ground states.* In order to accommodate the full pattern of the ground state, the magnetic unit cell often contains several crystallographic unit cells. The possible patterns in an RS ordered double perovskite

[4] In compensated ferrimagnetism, oppositely aligned spins are numerically balanced to cancel out. [141]

[5] This is known as Lieb-Mattis-type ferrimagnetism, as described by Lieb and Mattis. [142]

depend on if whether all B-sites are involved (cubic arrangement) or only one (tetragonal arrangement). Possible magnetic ground states patterns for cubic arrangement have been labelled A to G, with B representing FM arrangement, by Wollan and Koehler [90]. These include the patterns seen for ion ordering, corresponding to A-type (layered), C-type (columnar), and G-type (RS-order). AFM patterns concerning only one B site typically arrange in a layered manner following the crystallographic directions $[1\ 0\ 0]$ (type I), $[1\ 1\ 1]$ (type II), or $[1\ 2\ 0]$ (type III). Type III is an example of an arrangement in which the magnetic unit cell contains two crystallographic unit cells. [7] All these patterns are presented in Figure 14. More complex AFM patterns are also possible, such as screw-type AFM in which spin alignment follows a fourfold screw axis [91], and superstructures of multiple fundamental patterns, for example D-E and G-F [90]. Similar to FiM, AFM arrangements can also be canted and present a sidewise net magnetization. [86]

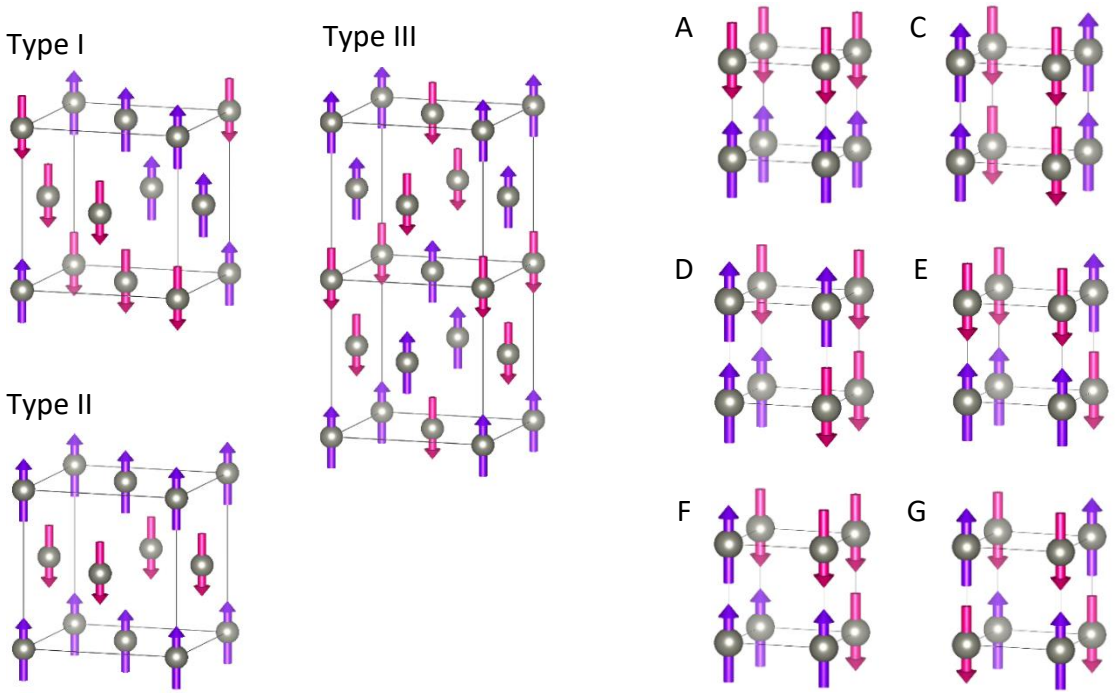

Figure 14. Left: the three types of AFM patterns found in RS ordered double perovskites when only one B site is concerned. Right: the fundamental cubic lattice AFM types as defined by Wollan and Koehler. For most of these patterns, multiplication of the cell shown is required to include the full magnetic pattern.

A common parameter for comparing magnetic behaviour is magnetic susceptibility χ. The magnetic susceptibility describes how a material will adapt spin ordering in response to being subjected to a magnetic field. The absolute value of χ describes the magnitude of the ordering as a function of the applied field strength, and the sign determines the direction of the alignment.

Although paramagnetic materials express no net magnetization nor preference of spin alignment, paramagnets should not be confused with nonmagnets. Nonmagnetic materials are characterized by

their lack of unpaired spins, thus presenting no magnetically polarizable constituents. Paramagnetic materials contain unpaired electrons, which are too weakly coupled to align spontaneously, but which can react to the application of an external magnetic field, i.e. their magnetic susceptibility is nonzero. A special case of paramagnetism is *diamagnetism,* which is the only case where the induced spin polarization aligns antiparallel to the external magnetic field i.e. $\chi < 0$. Diamagnetic response can never be larger than annulment of the applied field, limiting the strongest diamagnetic susceptibility to $\chi = -1$. [86,92] This can only be achieved in superconductors, in which diamagnetism is a consequence of induced electrical screening currents [93] rather than electron-orbital interactions. Superparamagnetic magnetization is only limited by the maximal number of unpaired spins that can be incorporated in any given structure, and is currently achieved in nanostructures of intrinsic strong ferromagnets such as magnetite.[94]

5.2 Temperature and transitions

The appearance of magnetic order is dependent on temperature. Thermodynamics prevent spins from ever being permanently fixed in one direction, and with rising temperature, thermal fluctuations gradually decrease the average extent of alignment until thermally induced random spin flipping overpowers any magnetic arrangement. Thus, every material has a *magnetic transition temperature* above which it becomes paramagnetic; for ferro- and ferrimagnets this is called the Curie temperature (T_C), and for antiferromagnets, the Néel temperature (T_N). Some ferromagnets can express weak magnetization above T_C due to transient formation of local alignment, called the *Griffiths phase*.[95] More complex magnetic transitions are also possible, and can be connected to structural phase transitions. [4,68,86,92]

The magnetic susceptibility of both FM, FiM and AFM materials follow the Curie-Weiss law above the Curie/Néel temperature. The Curie-Weiss temperature or Weiss constant Θ is commonly used as a measure of whether FM or AFM interactions dominate the overall magnetic behaviour. FM occurs when Θ has a positive value, and AFM when Θ is negative. For the critical value $\Theta = 0$ the interactions are perfectly balanced, resulting in exceptional magnetic behaviour, returned to in Chapter 5.4. The absolute value of Θ corresponds with the ordering energy and thus gives an indication of the magnetic ordering temperature, which indicates the strength of the magnetic ordering. The value of Θ is found by plotting the reciprocal molar magnetic susceptibility (${\chi_n}^{-1}$) against temperature and extrapolating the slope of the paramagnetic section to the intersection with the temperature axis. [24,96]

5.3 Spin exchange interactions

The quantum mechanical operations provide multiple types of spin exchange interactions, of which the three most common ones are direct exchange, double exchange, and superexchange. Direct exchange requires very close proximity of magnetic ions, and involves electron hopping between overlapping orbitals. Magnetic behaviour in 3d-metals is well described by direct exchange, but in the perovskite lattice, the distance between cations exceeds its effective range and other mechanisms dominate. Double exchange also involves electron hopping between ions holding both localized and delocalized electrons, and requires the participating elements to support mixed valence states. Following Hund's rule, electron hopping is only allowed between ions when the hopping electron's spin can be preserved, i.e. when the localized spins in the adjacent ions are parallel. Thus, double exchange always induces parallel alignment of neighbouring spins. The double exchange interaction is very sensitive to bond angles, as even a small misalignment requires readjustment of the spin alignment for the exchange to take place. At 90° misalignment, double transfer hopping is completely blocked. Double exchange can take place in perovskites but is not common. [86]

Superexchange is the predominating exchange mechanisms in oxides, including perovskites, and leaves all involved spins localized. Spin alignment is communicated via so-called J-coupling, which connects spins via virtual electron transfers mediated by chemical bonds. J-couplings can extend over several atoms, expanding the complexity of the system and introducing coupling competition. Superexchange interactions can be either ferromagnetic ($J > 0$) or antiferromagnetic ($J < 0$) across any given pair of coupled spins. The strength and sign of J is mostly determined by electron orbital occupancy and degeneracy, interatomic distances, and bonding angle. The extensive set of interconnected rules have been developed into a set called the *Goodenough-Kanamori rules* [97,98], which successfully help predict the strength and sign of J in cases where magnetic anions interact via an intermediate nonmagnetic anion. The Goodenough-Kanamori rules have been reformulated by Anderson, forming a set of rules often referred to as the *Goodenough-Kanamori-Anderson rules* that better fit the description of perovskites. These are frequently recited as: [86]

1) *Strong AFM interaction* will appear for M-O-M bonds at 120°-180° angles, when both hold singly occupied 3d-orbitals pointed at each other, with large orbital overlap and large hopping integrals
2) *Weak FM interactions* will appear for M-O-M bonds at ∼90° angles, when both hold singly occupied 3d-orbitals that have zero overlap due to symmetry
3) *Weak FM interactions* will appear for M-O-M bonds where one atom holds a singly occupied 3d-orbital which overlaps with the other atom's empty or doubly occupied orbital of the same type

The rules emphasize the acute effect of bond angles on the strength of the interaction. Changes in bonding angles associated with structural phase transitions can thus have dramatic effects in systems with competing AFM interactions. As orbital overlap integrals are often large and rarely zero, AFM interactions dominate in superexchange.

J-couplings weaken with distance, leaving two dominating coupling types within either B sublattice: nearest-neighbour (NN) and next-nearest neighbour (NNN). Interspecies couplings taking place between the sublattices are discussed further down. Examining the cubic perovskite setting, NN couplings are found along the face diagonals, and NN couplings along the unit cell axes. Theoretically, spins can couple throughout the crystal, but beyond the third-nearest neighbour interactions become negligibly weak, as well as difficult to calculate. In distorted perovskites, coupling strengths will differ depending on their geometrical position in the unit cell, and J-constants must thus be given separately for every inequivalent ion pair. Lower indices are used to annotate different J-coupling constants, defined case-by-case based on the lattice and its magnetic interactions. Prediction of extended superexchange is still imprecise, and computational methods are required for solving the magnetic state of systems containing multiple unequal and conflicting J-couplings. [99] The most dominant four couplings in an orthogonal perovskite are shown in Figure 15.

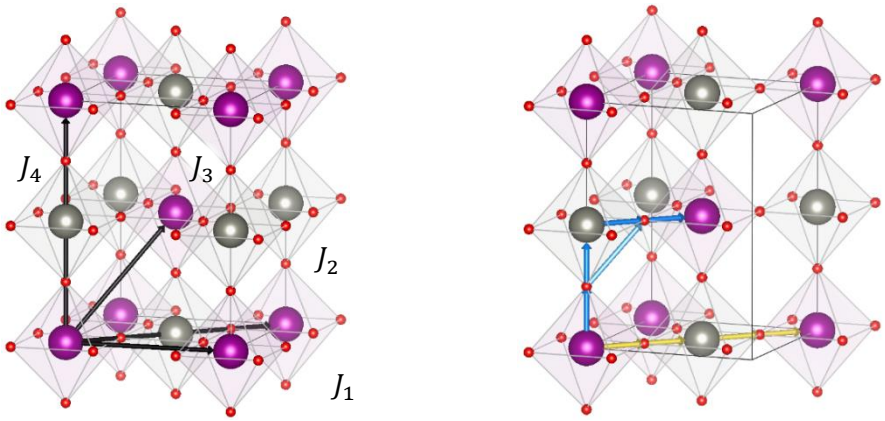

Figure 15. J-couplings in a double perovskite unit cell, shown in orthogonal setting for clarity. To the left, atom-to-atom J-coupling interactions numbered. To the right, the nearest-neighbour (NN) pathway shown in blue (oxygen shortcut in paler blue), and the next-nearest-neighbour (NNN) pathway shown in yellow.

An additional exchange type can take place in systems already connected by superexchange. This weak, antisymmetric interaction is known as the *Dzyaloshinski-Moriya interaction*, or D-coupling. It can occur in materials with low symmetry, between spins laying in the plane perpendicular to the highest-symmetry axis, and results in a minuscule, parallel canting of AFM arranged spins. Thus the Dzyaloshinski-Moriya interaction can induce weak ferromagnetic moments in otherwise antiferromagnetic materials, with D ca two orders of magnitude smaller than J. [86]

The choice of spin pattern is determined by competitions between orbital spin interactions in the t_{2g} and e_g orbitals, of which e_g takes the higher energy in an octahedral crystal field. Both types of orbitals take part in superexchange interactions over the linear M-O-M-bond, and the strength of interaction is extremely sensitive to changes in distance. In shorter bonds, e_g orbitals become compressed and their superexchange becomes weaker, allowing t_{2g} superexchange to dominate. Thus, minuscule differences in bonding distances can have determining effects on spin pattern, and are especially influential in the choice of spin pattern in AFM compounds. Whether the interaction is AFM or FM depends on whether the occupancy of the orbitals on either side of oxygen are the same or not. Uneven occupancy of the e_g-orbital where one of them is empty promotes FM coupling, while most other combinations allow for AFM. [43]

Another requirement for superexchange is that the interacting orbitals must match in energy. In B site ordered double perovskites, the different B site species can couple magnetically to each other only if both are Kramer's ions and the magnetically active orbitals are of comparable energy. When the energy difference grows, orbital overlap rapidly decreases and the strength of the coupling weakens. [7,100] Consequences of this, with regard to choice of elements, are more closely discussed in Chapter 5.4. The requirement for orbital overlap also illuminates the effect of bonding angle on the strength of magnetic interactions. Since the electron density of the t_{2g} and e_g orbitals varies spatially, ion placements must structurally match the spatial arrangement of the orbitals. In a bent bond, the oppositely placed p-orbitals of oxygen cannot simultaneously overlap both B site ions' orbitals perfectly, and the magnetic interactions are weakened. Both FM and AFM couplings are negatively affected by increased bending, but at different rates, allowing the adjustment of bonding angles to be deterministic of magnetic ordering regime in some cases. One example is the A_2NiOsO_6-series, where altering the A site chemistry by $Ca \rightarrow Sr \rightarrow Ba$ gradually decreases the octahedral tilting, allowing FM interactions to strengthen, without the also-strengthened AFM interactions rising to domination. [101]

The electromagnetic environment of the $B'O_6$-octahedron is not spherosymmetric, but provides different energies for different spin alignments. Thus, spin alignment cannot follow any crystallographic direction, but will prefer an alignment corresponding with a local energy minimum, called an *easy axis*. The directions of the easy axes depend on magnetic species, distortions, and unit cell parameters, and can change with temperature. [86,102] Canted magnetic alignments can be explained by non-parallel easy axes in adjacent $B'O_6$-octahedra, for example due to octahedral tilting.

5.4 Complex magnetic behaviour

B site ordered double perovskites express multiple types of complex behaviour. Complex behaviour, including multiple magnetic transitions, can occur both when the cations interact and when they arrange independently from one another. The doubled B site presents an extended chemical variability and increased amount of possible magnetic exchanges within the same phase. Including the A site, three interpenetrating lattices of cations are available, and all can hold magnetic species. Whether they interact or not depends on whether they are able to couple magnetically. Aside from the requirements of proximity and possession of unpaired electrons, magnetic interaction between two atoms also necessitates the spins to inhabit overlapping energy levels. If the energy of the orbitals holding the magnetically active unpaired spins are on a comparable level, they can couple, but if they differ significantly coupling is inhibited. Consequently, magnetic couplings are often strongest between chemical species of the same period, and weaker or even unavailable between 3d/5d transition metal pairs. [100,103,104]

An example of independently ordering B site sublattices as a consequence of orbital energy mismatch is RS ordered Sr_2CoOsO_6. [103] Here, both the cobalt and osmium ions adopt AFM arrangements, but at different temperatures. This independent behaviour is explained by the significant difference in energy between the t_{2g} orbitals of Os^{6+} and e_g orbital of Co^{2+}, leading to dominance of the longer-distance *M–O–M'–O–M* couplings. Upon cooling, both metals first adopt interpenetrating, long-range AFM order of locally fluctuating spins, then cobalt spins freeze in a type II AFM pattern which later becomes canted, and finally osmium settles in a complex canted AFM ground state. A structural transition is associated with the ordering of osmium. [103,105]

Magnetic interactions between the A and B sites are rare, but can occur when occupied by chemically similar species. In $(NaMn_3)Mn_4O_6$, complex behaviour arises from a combination of magnetic interactions between A and B site Mn^{+3} ions, and $Mn^{+3/+4}$ charge ordering of the B site. [106] Several A/B double perovskites present magnetic interactions between magnetic species on one A and one B site. The most prominent series contain cupper as a majority element at the A site, for example $CaCu_3Fe_2Sb_2O_{12}$ [96] and $CaCu_3Fe_2Nb_2O_{12}$ [76] , both of which express antiferromagnetic coupling between cupper and iron. Exchange between all three sites is also possible and has been recently documented in ferrimagnetic Ln_2CoIrO_6 with Ln = Eu, Tb, Ho. [107]

In RS-ordered B site sublattices, AFM-coupling can cause geometric frustration as a result of the tetragonal lattice arrangement. If all distances are equal, no overall optimal arrangement of spins is available: the ground state is degenerate. The frustrated magnetic structure can remain mobile,

forming a spin liquid phase of infinitely fluctuating spins, or freeze in a spin ice or spin glass phase. In the spin glass phase spins pair up into pairs of opposing alignment, which in turn align randomly between themselves, locking the material into one of the available ground states at random. The formation of a spin glass phase is aided by the availability of distinct easy axes, into which the spins settle pairwise below the spin freezing temperature T_G. [12–15] Several spin glass perovskites have been found, for example Sr_2CaReO_6.[108] A variation of spin glass is spin ice, in which longer-range interactions between spin pairs reduce the number of degenerate ground states. In spin ice, the frozen spins express long-range order, similar to the proton distribution in aquatic ice. Contrary to spin glass, application of a magnetic field will promote spin freezing in spin ice. The most famous spin ice compound is pyrochlore $Dy_2Ti_2O_7$. [109] Perovskite examples are still being sought.

Frustrated spin phases may also occur in the border regime between different types of AFM ground states, for example columnar (C-type) and Néel (G-type) AFM, which have been examined for the appearance of spin liquid behaviour. [110] There are several examples of spin glass phases appearing as a result of adjusting chemical pressure. Substitution with Ca^{+2} in the place of Sr^{+2} on the A site of series A_2CoOsO_6 results in a transition from AFM to FiM behaviour, with a small window for spin glass behaviour when the Ca/Sr ratio is around 1:1. The critical parameter is the evolution of the bonding angle B'-O'-B'', which determines what exchange interactions will dominate. Spin glass arrangements appear for both of the weakly coupled B-sublattices, adding a doubling of the spin freezing temperature (T_{G1}=32 K, T_{G2}=13 K) to the complexity of the phase. [72] The sister series A_2FeOsO_6 undergoes a similar structure-magnetic transition [111] and could potentially express similar behaviour.

Charge disproportionation presents an interesting pathway to magnetic transitions. As magnetic behaviour depends on valence electron structure, the same atom may express different magnetic interactions at different oxidation states, as has been seen in $CaCu_3Fe_4O_{12}$. Upon cooling, the Fe^{4+} ion becomes unstable around 210 K and disproportionates into Fe^{3+}/Fe^{5+}, inducing a small structural rearrangement and a drastic change in behaviour from an electrically conducting nonmagnetic state to an electrically insulating FiM state, where all iron spins are parallel and cupper is antiparallel. [112]

Mixed-valence cations can promote ferromagnetic interactions through double exchange between degenerate electronic ground states. The perovskite $(La, Ca)MnO_3$ contains both Mn^{3+} and Mn^{4+} ions, where the distribution of oxidation states results in a ground state degeneracy. Transitions between the ground states require local charge transfer between ions, which in turn requires ferromagnetic polarization of the d-orbitals holding the itinerant electron. Thus, the electrical

conduction of mixed-integer oxidation states is linked to spin polarization, which is sometimes expressed only at low temperatures. [113] The spin-polarized conductors are closely related to half-metals, introduced theoretically by de Groot *et.al.* in 1983. [114] In half-metals, the electronic density of states (DOS) is asymmetric, with the most drastic difference at the Fermi level, where one spin channel is discontinuous and the other continuous. This allows materials to simultaneously express both ferromagnetism in the localized spin channel and metallic conduction in the itinerant channel, with the additional feature of the electric current being perfectly spin-polarized. [113] Among the earliest examples of ferromagnetic half-metallicity in perovskites is $La_{0.7}Sr_{0.3}MnO_3$, which shows an itinerant majority spin channel and a localized, FM aligned minority spin channel. Above T_C the phase becomes paramagnetic and completely insulating. [115] Several other compounds have been predicted half-metallic, among them a mixed rutile $Cr_{½}V_{½}O_2$, which was experimentally shown not to form with the required oxidation states, but which provides an excellent example of the asymmetric density of states seen in half-metals (Figure 16). [116]

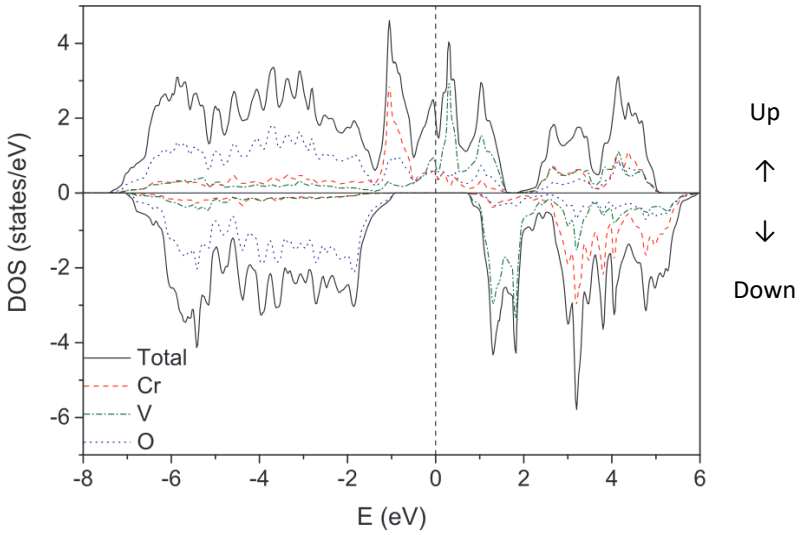

Figure 16. The predicted density of states of $Cr^{4+}{}_{½}V^{+4}{}_{½}O_2$, clearly showing the asymmetric distribution of the spin-up and spin-down channels. At the Fermi level (E=0eV), the continuous nature of the spin-up channel provides spin-up polarized metallic conduction, while the discontinuous spin-down channel renders electrons localized and allows ferromagnetic magnetization. Reprinted from ref [116].

5.5 Effects of cation ordering

The degree of cation ordering drastically changes the distribution of different chemical environments, altering bonding and bonding-derived physical properties of the material. Magnetic interactions are especially strongly affected, with several magnetic ground states highly reliant on an unbroken RS-ordered B site lattice. This is easily understood by revisiting the various possible J-couplings, shown

in Figure 15. When antisite B ion defects are introduced, the J-couplings in their vicinity are drastically altered, leading to different dominating interactions than in the rest of the crystal. Another effect of order is the regular pattern it creates for the electronic potential landscape. The presence (or absence) of a periodic potential can affect electric conductivity in a decisive manner. One example is Sr_2FeMoO_6 in which half-metallicity has been predicted for the perfectly ordered case. [50]

Since AFM interactions are stronger and more common, many FM compounds rely on B site order for avoiding AFM couplings of adjacent same-species ions. One such example is La_2MnCoO_2, which expresses a strong change in magnetic behaviour depending on the degree of order at the B site. In its ordered state, all nearest-neighbour interactions are of Mn^{4+}-Co^{2+} type, a rare case of strong FM coupling. Introducing randomly distributed antisite defects, the increasing number of AFM-coupled same-species ions on adjacent sites presents an interruption that gains influence until it percolates and becomes dominant. [45,117] La_2ZnMnO_6 behaves similarly, as the FM behaviour stems from FM-couplings over nonmagnetic Zn^{2+} ions. [87] Even in cases where the magnetic interactions include the A site does the degree of order play a crucial role. In $CaCu_3Fe_2Nb_2O_{12}$ strong magnetic coupling between Cu^{2+} and Fe^{3+} make the compound ferrimagnetic, but only when the B site is ordered. When order of the B site is disrupted, magnetic order of the A site is destroyed as well, despite the A site retaining its 1:3 BCC ordering regardless of the state of the B site. The degree of order at the B site can be finely tuned by adjusting the cooling rate of the last stage of synthesis, thus prematurely disrupting the diffusion process that enables ordering. [76]

A special case where the disruptive influence of disorder could be exploited is linked to the search for a spin liquid phase in perovskites. This has been employed in $Sr_2Cu(Te,W)O_6$ by introducing disorder in the nonmagnetic B subsite only, taking advantage of the influence of the valence orbitals of the intermediate ion in the B'-O-B''-O-B' superexchange system. In this compound, Cu^{2+} makes up the AFM coupled magnetic sublattice, in which different superexchange pathways come to dominate depending on whether the nonmagnetic site is occupied by Te^{6+} or W^{6+}. Mixing these two together in a random distribution introduces confusion in the superexchange interactions, promoting magnetic frustration, which is required for a spin liquid ground state. [75]

6 Multi- and megavariate analysis in chemometrics

Chemometrics is the science of applying mathematical tools for describing and analysing real-world chemical systems. The field was established in the 1970-es with the introduction of computers in chemistry, allowing for faster mathematical analysis of measurement data and application of statistical methods for recognizing trends, correlations, and deviations in measurements. In contrast to most computational methods, chemometrics does not require a phenomenological model of the data to be analysed. This blindness to theory allows application of chemometric methods on complex systems and data that does not fit any known model, and can even be used to find new variable correlations and thus aid model development. Today, chemometric methods are widely used in industry for automatic process supervision, regulation, and quality control, e.g. by correlating upstream process parameters with downstream analytic data. [118]

One tool in chemometrics is *multivariate data analysis* (MVA or MVDA), an expansion of linear regression analysis of two-dimensional data into systems with multiple variables. Compared to the number of observations N, the number of variables is allowed to be high, even larger than the number of observations. MVA variables are divided into two types; *predictor* variables (x_i) that define the state or setup of a system, and *response* variables (y_i) that describe the behaviour. These are often spoken of as the X-variables and the Y-variables, and the spaces drawn up by each group are called the k-space and m-space, for k X-variables and m Y-variables, respectively. The *rank* of the dataset is determined by the total number of independent variables. A specialized version of MVA, adapted for cases where part of the variables are interdependent, is called *megavariate analysis* (MgVA). The term 'MVA' is often used to refer to both cases. [118]

The fundamental tools of MVA treat all variables as independent X-variables, i.e. the dataset is assumed to be full rank ($K = k$). This can be illustrated as a matrix X of width k and height N. Key functions include *multiple linear regression* (MLR) for finding multidimensional correlations, *linear discriminant analysis* (LDA) for describing the importance of each variable, and *factor analysis* (FA) and *principal component analysis* (PCA), which are both used for finding the main correlations, but employ mathematically different methods. Classical MVA is well suited for separating groups of similar but uncorrelated observations described by uncorrelated variables. A weakness of treating all variables as independent is the possibility of detecting false or exaggerated correlations between

variables. Caution is thus needed when drawing conclusions about systems that lack an established theoretical description. [118]

For systems containing variables that are known to be linked in an $y = f(x)$ manner, MgVA methods are preferred. With some variables already linked to each other in the input data, the effective rank of the dataset is reduced ($K < k$). This can be visualized as a matrix X of width k and height N which correlates to a matrix Y of width m and height N. The most important functions in MgVA are projection methods that aim to reduce the complexity of the dataset by compressing the original variables into a smaller set of new variables, called *principal components* (PC:s). Fundamental methods are *principal component analysis* (PCA) and *partial least square projections to latent structures* (PLS), which can be combined with additional methods forming e.g. *PLS discriminant analysis* (PLS-DA). The primary methods PCA and PLS are described in more detail below. [118]

Since projection methods are sensitive to the numerical values of the data points, pre-processing of the data is required to assure that all variables are given equal emphasis in the analysis. This means normalizing each variable and translating the value of each data point onto a standardized scale. Various normalization methods are available. The simplest one is *unit scaling* whereby each observation for a given variable is linearly transferred to a $0 \dots 1$ range. However, this makes it sensitive to divergent extreme data points. A more anomaly-tolerant method is *unit variance scaling*, in which the variables are scaled to equal variance (unit variance $\sigma = 1$). Following normalization, the data is mean-centred by setting the mean value of each variable to zero. [118]

Although MVA and MgVA are developed for numerical data, methods are available for including qualitative variables as well, for example synthesis method. Qualitative variables are most commonly incorporated for describing classes, i.e. pre-known groupings of observations, but can also be treated as model-making variables. In that case, they need to be translated to numerical values, which is generally done by splitting the qualitative variable into a set of binary variables, one for each value of the original variable. [118]

6.1 Principal component analysis

The main principle of *principal component analysis* (PCA) is transforming the raw data into a new data set of lower dimensionality, while simultaneously finding correlations among the original variables. PCA can be performed on any set of independent variables, and is thereby applicable both for datasets containing only X-variables and for sets with both X- and Y-variables: in the latter case, PCA is only performed on the X-variables and its results compared to the Y-variables. [118]

PCA is performed on the normalized and mean-centred data by adding principal components (PCs) to the model one by one, until the model can no longer be improved. Each PC is added to the multidimensional data plot along the direction of largest variance that is perpendicular to all previously added PC:s, and must pass through the mean point of all variables (set to the Origin by the mean-centring). The plane drawn up by any combination of two PC:s is called a *model plane*. Each data point is given a new set of coordinates determined by its projection onto the model planes of the projection space (*T*-space) drawn up by the PC:s. These new coordinates are called *scores*, and their values are described by *score vectors* t_i which replace the PC:s to make the basis for the new setting. [118] The process is visualized in Figure 17a.

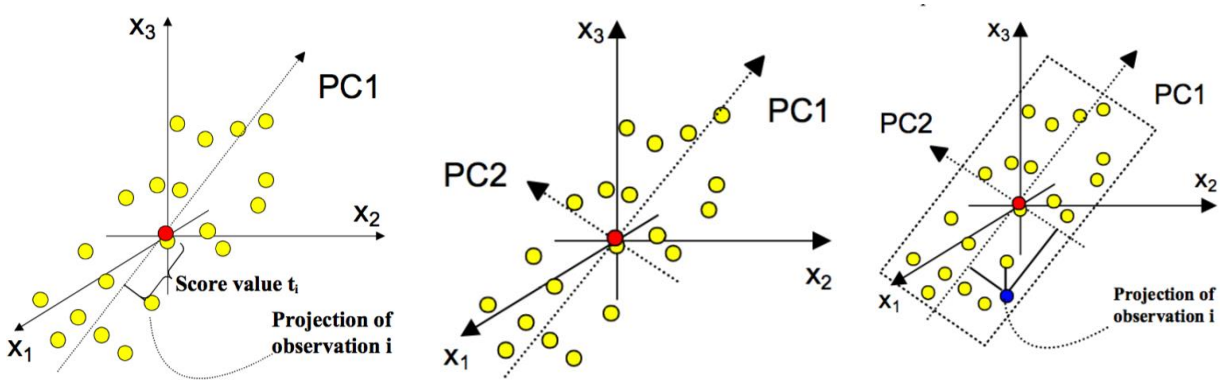

Figure 17. Geometrical interpretation of the process of adding PC:s to a dataset of rank *K*=3. From left to right, the data is first normalized and mean-centred around the Origin (red dot). The first PC is fitted along the direction of largest variance, and each sequential PC is then added along the direction of highest remaining variance that is perpendicular to all previous PC:s. Finally, the observations (yellow dots) are projected onto the PC:s to give their scores in projected space (blue dot). (Figure adapted from ref [118] fig. 3.12-3.14, page 40-41)

As the PCA model consists of significantly fewer score vectors than the original number of variables, some data on the original position of each data point will be lost. The distance of each data point to its projected position in *T*-space is collected in the *residual matrix* E. Mathematically, the original data X is reformulated in the PCA model as $\mathrm{X} = 1 \cdot \bar{\mathrm{x}}' + \mathrm{T} \cdot \mathrm{P}' + \mathrm{E}$, where the $1 \cdot \bar{\mathrm{x}}'$ term represents the normalization and mean-averaging operation. The residual matrix can be useful for analysing divergent data points and determining outliers, as described below. [118]

Since the variance and linearity of variance is reduced for every added PC, the first few score vectors tend to contain the majority of useful information on the system. Plotting two score vectors against each other yields a *scores plot,* in which the original observations appear as described by their new coordinates. Examination of the scores plots can reveal information on groups, trends, and divergent observations. Major contributors to the positioning of each observation in the scores plot can be found in the *loading plot*, set up by the *loading vectors* p_i which make up the loading matrix P. The

loading vectors describe the contribution of each original X-variable in the formation of the score vectors, and help determine which of the original variables contribute the most to separating observations in a given score plot. The loading plots also reveal correlations between original variables, with strongly correlated variables placed close together across multiple plots, and variables of low importance placing near the Origin. Of similar use is the *variable importance plot* (VIP) which describes the overall contribution of each variable for drawing up the model. High contributors hold values above 1, moderate contributors have values $0.5 \dots 1$, and variables with <0.5 weight are considered unimportant. The contribution of each original variable on the T-space positioning of an individual observation can also be separately examined, e.g. for determining if its position might be influenced by a missing data point. [118]

6.2 Partial least square projections to latent structures

PLS is closely related to PCA, but especially adapted for cases with both multiple X-variables and multiple Y-variables. While finding principal components and correlations within the X-variables, PLS simultaneously does the same for the Y-variables. The ability of the method to find correlations in complex datasets and vague or approximate relationships between the X- and Y-variables makes PLS reminiscent of thermodynamic models, which often describe macroscopic behaviour without connecting to microscopic theory. This 'blindness' to theory makes PLS especially useful for analysing complex phenomena lacking an overall-valid theoretical model, or for providing further support for a suggested theory. [118]

The principle of PLS is closely reminiscent to PCA, with the dominating difference being the inclusion of a Y matrix in the original dataset. This means that every observation is described as a point in two different spaces: the *k*-space defined by the X matrix, and the *m*-space defined by the Y matrix. As PC:s are added to the model, the position of each observation must be considered in both spaces simultaneously, meaning the orientation of the PC:s in *k*-space are affected by the shape of the point swarm in *m*-space. In other regards, PC:s are added by the same principles as in PCA, but the rule of orthogonal PC:s only applies to *k*-space. [118]

With two variable spaces to transform, the PC:s will translate into two sets of scores in the projected model. The score vectors replacing the Y matrix are named u_i, and are created pairwise with the score vectors t_i being generated from the X matrix. Plotting t_i and u_i against each other reveals whether the correlation found between the predictor variables and response variables is linear or follows some other mathematical trend. The contribution of each variable to the model is described by the

weight vectors, denoted w^* and c for the X- and Y-variables respectively. In other aspects, interpretation of the PLS data is highly reminiscent of PCA and similar conclusions regarding trends, groups and outliers can be drawn. Mathematically, the data reformulation in PLS can be described by

$$\begin{cases} \mathrm{X} = 1 \cdot \bar{\mathrm{x}}' + \mathrm{T} \cdot \mathrm{P}' + \mathrm{E} \\ \mathrm{Y} = 1 \cdot \bar{\mathrm{y}}' + \mathrm{U} \cdot \mathrm{C}' + \mathrm{F} \end{cases}$$

where F denotes the residual matrix for the projection of the Y-variables. Due to the inner relation between X and Y, $\mathrm{Y} = 1 \cdot \bar{\mathrm{y}}' + \mathrm{T} \cdot \mathrm{C}' + \mathrm{G}$ (where G is another residual matrix) also holds. The increased mathematical complexity of PLS means that missing and aberrant data points are better tolerated than in PCA. [118]

6.3 Model quality and outliers

The mathematical requirement of orthogonality between all PC:s results in a limit to the number of PC:s, as the rank of the model cannot exceed the rank K of the original dataset (i.e. the number of X-variables). For a good model, however, the number of PC:s needs to be considerably lower than K. The optimal number of PC:s is determined by following the evolution of two parameters, R^2 and Q^2, as PC:s are added to the model. Both are given as a value between zero and one. The goodness of fit parameter R^2 (explained variation) describes the extent to which the model explains the dataset, and the goodness of prediction Q^2 (predicted variation) expresses the accuracy of the model's predictions. R^2 and Q^2 can also be investigated separately for each X-variable, revealing which variables are well explained by the model and which are not. [118]

The optimal rank of the model is determined by simultaneously maximizing the values of R^2 and Q^2 while keeping their difference at a minimum. The value of R^2 will inherently approach one as more PC:s are added, but Q^2 tends to undergo a fluctuating increase and then drop off sharply. Hence, Q^2 is considered more critical, and the optimal amount of PC:s is found where the value of Q^2 stops increasing or the difference between Q^2 and R^2 grows too large. For an acceptable model, both parameters should express values > 0.3, while values of $Q^2 > 0.5$ are considered good, and values of $Q^2 > 0{,}9$ is deemed excellent. [118]

Outliers and misleading data points can be detected by examination of score plots, loading plots, and plotting the data in the residual matrix. Score plots are often analysed by adding *confidence limits* such as Hotelling's T^2, which appears as an ellipse around the mean point of the given score plot. With a given confident limit, often taken as 95% by default, that fraction of observations should lie inside the confidence ellipse and the remaining ones not far outside it. Data points falling far outside

the confidence ellipse are potential outliers and deserve closer examination. *Moderate* and *strong outliers* are separated by their behaviour across multiple plots, as well as the *distance to model plot,* which is based on the sum of the observation's residuals stored in the residual matrix. Data points that deviate consistently across multiple plots as well as in the sum of residuals can be concluded strong outliers, while moderate outliers only deviate across some plots but does not present an aberrant sum of residuals. Strong outliers can potentially have strong leverage on the entre model, affecting the positioning of PC:s and shifting the confidence ellipse. Closer examination of strong outliers can reveal justifications for exclusion of the observation, e.g. if it is found that the aberrant behaviour stems from a possibly erroneous measurement. [118]

7 Density Functional Theory

Density functional theory (DFT) is a material modelling method, in which material parameters are calculated in a theory-based manner. This bottom-up approach is called *first principles modelling* or *ab initio calculations*, referring to the construction of data based purely on fundamental models of the physics at play in the structure, and not at all on experimental measurements. In the case of DFT, modelling is based on quantum mechanics, i.e. the mathematical description of quantum particles' properties and interactions. The core of the method is the famous Schrödinger equation in its complex, many-body form. [119] The Schrödinger equation was first presented by Schrödinger himself in 1926 [120], and describes the discrete behaviour of the energy of matter particles. Due to its complexity, the equation can only be truly solved for a system with maximum two particles. Larger systems can only be approximately solved employing one of several tactics for mathematical simplification of the problem, with sequential corrective terms. These methods consume vast amounts of computational power, requiring the use of supercomputers for any structures of higher complexity as the computational power needed scales approximately cubically with the number of atoms included in the simulation. [119]

In DFT modelling, the Schrödinger equation is used for solving the electron density of the valence electrons in a given landscape of atoms. The goal of DFT is to find the optimal parameters for a given structure, for example bond angles and bond lengths, and then analyse the energy landscape for this model. Direct results from the calculations are electronic density distribution and total energy of the system. Extractable data include dielectric constant, piezoelectric behaviour, polarizability, electronic band structure, phonon modes, heat capacity, and optical properties. The structure of optimal energy is found by an iterative process, where the free parameters are adjusted in a systematic way for each iteration until the calculations repeatedly yield a result within the given error margins. For example, structural optimization is performed by adjusting the positions of the atoms based on the previous iteration's energy landscape, until the calculated energy converges at a minimum. [119]

Mathematically, there are several ways of applying DFT for a simulation, and different software adapt different algorithms. The core tactic is plotting the atoms as a rigid grid of potential wells, and calculate the behaviour of their valence electrons in the established landscape of positive ions. This is called the *clamped nuclei* approximation and is employed for solid materials where atoms can be assumed 'clamped down' i.e. locked into their position in space. Modern calculations employ ionic pseudopotentials, treating the atom nucleus and its core electrons as a single unit. Treating the nucleus and core electrons as a single unit is motivated by the negligible participation of the core

electrons in interactions that determine material properties. The valence electrons are assumed to be perfectly independent particles, whose freedom to move throughout the system is only limited by the potential landscape of the ion grid. Such neglect of the Coulombic repulsion between electrons might seem crude, but has been shown to result in electron behaviour in agreement with the fundamental rule of electron energy states being filled up from the lowest energies and allowing only single occupancy of each state. The identity of each filled-up energy level combined with the calculated spatial electron density reveals how localized the electrons around each ion are, in turn producing the other physical and chemical properties of the material. [119]

The key to a good DFT model lies in the way the ionic pseudopotential is mathematically described and how the electron density over the material is calculated. As the best theoretical model for the potential well around a nucleus or ion leads to extremely heavy calculations, different mathematical shortcuts are used to enable calculation of larger systems. The simplest method for approximating local electron density is the local density approximation (LDA). Today, ultra-soft pseudopotentials such as the projector augmented wave (PAW) method are widely used. Other common tools include the Perdew-Burke-Ernzerhof (PBE) functionals for the exchange correlations and the generalized gradient approximation (GGA) for framework. Several different simplifications, derivations, and corrective measures have been developed for these, for example the ones described by Xu *et.al.* [121] and Perdew *et.al* [122,123]. A more thorough introduction to the various details of DFT can be found in the book by Feliciano Giustino [119] as well as other sources.

8 Objective

Among magnetic materials, the ferromagnetic ground state is the most useful one for technological applications. Unfortunately, antiferromagnetic coupling is considerably easier to achieve, rendering antiferromagnetic behaviour overwhelmingly more common than ferromagnetic. One of the central goals for predictive methods is thereby finding candidates for ferromagnetic materials with sufficiently high magnetic ordering temperatures to be useful. As theory-based predictive methods are unsuitable for wide-range screening, more blunt methods based on statistical modelling have been tried [16,124] but their application is still far from widespread. Investigations with high-precision simulation methods have frequently pointed out strong candidates for wanted magnetic states only for them to be discovered to form other phases in reality. A frequent occurrence with perovskites is the formation of the hexagonal perovskite phase instead of the cubic structure that might produce the wanted magnetic interactions.

In this work, the influence of composition on structure is evaluated in a series of samples with varying A site chemistry, which imitates the influence of applying pressure to a hexagonal perovskite phase in order to induce a transition to cubic perovskite structure. Transformation from hexagonal to cubic structure under pressure has proven successful before [17], and is suggested to have similar effects on the hexagonal phases Ba_2CoIrO_6 [24] and Ba_2CrReO_6 [125]. Both of these are members of FM perovskite families, and are predicted possibly FM in their cubic form. [126] Here, chemical pressure is introduced in Ba_2CoIrO_6 by partial substitution of Ba with Sr, which is chemically similar to Ba but ca 10% smaller. A series of six samples with 20% increments in the molar fraction of Sr is produced and structurally evaluated to find the point at which the structure transforms from hexagonal to cubic perovskite.

Two mathematical methods for predicting magnetic behaviour are applied and evaluated. Density Functional Theory (DFT) is theory-based and gives reliable predictions for specific compositions, while Multivariate Analysis (MVA) is blind to theory and can provide quick and rough estimates on properties based on simple structural data. These are applied together in order to predict the magnetic behaviour of La_2FeIrO_6, a phase reported AFM in the 1990-es [127–131]. The phase presents a rare case of nonmagnetic Ir^{3+} on the B site. As data on its structure is lacking in detail, La_2FeIrO_6 is also synthesized and examined structurally. Previous syntheses [128–132] have mainly

mentioned La_2FeIrO_6 only as the end sample of substitution series $(Ca_{1-x}La_x)_2FeIrO_6$ and $(Sr_{1-x}La_x)_2FeIrO_6$, with emphasis on the behaviour of the other members of the series. Since phase purity has been reported a challenge in these investigations, special attention is given to solve the phase composition of the synthesized sample. Unfortunately, the magnetic behaviour could not be measured and compared to the predictions due to technical problems.

9 Methods

9.1 Experimental

Seven samples were synthesized: one standalone La_2FeIrO_6 sample and a six-membered $(Ba,Sr)_2CoIrO_6$-series, in which the ratio of the A site was varied in steps of 20 mol-%. Samples were prepared using a solid-state synthesis route. Stoichiometric quantities of La_2O_3 (pre-dried overnight at 900°C), Fe_2O_3, and IrO_2 versus $BaCO_3$, $SrCO_3$, CoO, and IrO_2 were weighed up and manually ground together in a mortar before undergoing repeated heating under ambient pressure, in air. For La_2FeIrO_6, precursors were ground for 1h and heated in powder form three times, first to 900°C for 24 h, then to 1050°C for 39h, and finally to 1100°C for 24h, with intermediate grindings. All members of the $(Ba,Sr)_2CoIrO_6$-series underwent identical treatment of grinding the precursor mixture for 20-25 min and then heating in powder form to 1150°C for 24h, performed twice with an intermediate grinding. All heating programmes were set to heating/cooling rates of max 200°C/h.

Phase purity and structural parameters were determined by X-ray powder diffraction (XRD) performed on a PANalytical XPert PRO diffractometer in Bragg-Brentano setup, using cupper $K\alpha_1$-radiation and a scanning range from 10° to 70° 2θ. Rietveld refinements were performed in Match! software (v. 3.4.2) [133] with FullProf [134]. In complement to FullProf, unit cell parameters were refined manually using Bragg's law and visualization software VESTA (v. 3.4.3) [135] for matching simulated and experimentally obtained XRD patterns.

9.2 Predictive calculations

Multivariate analysis was performed using the Simca P+® software v.11.5 [136]. Data was collected from publications printed during 2009-2019, consisting of 86 individual observations of AFM and FM samples. In order to mitigate statistical bias arising from the order in which B site co-occupants were reported, each observation was duplicated with the B site occupants switched around. Parameters included in the input data are listed in Appendix I, with X-variables in Table 11 and Y-variables in Table 12. Based on the input data, three models were created: one PLS model each for the AFM and FM compounds separately, and one combined PLS model. The sample of interest was entered into the data with dummy values for the Y-variables and AFM/FM group affiliation, in order to make the sample show up in the predictions plot.

DFT calculations were performed using Quantum Espresso software v.6.3 [137]. Atom potentials were modelled with the PAW method, with PBE exchange correlations and GGA framework. The K-point

grid was set to 7x7x7 with Monkhorst-Pack sampling centred around the Γ-point. Energy cut-off was set to 90 Ry and zero-Kelvin temperature assumed. The starting point structure was given in the orthorhombic setting, with parameters adapted from data provided by refs [128–132] (details are given in Appendix I, Table 13) and assuming perfect RS ordering of the B site. The structure was set to relax by the *vcrelax* function, which allows adjustment of both atomic positions and all unit cell parameters. Three cases were considered: nonmagnetic, ferromagnetic, and type II antiferromagnetic, the latter two assuming magnetic activity of the Fe site only. The most stable ground state of the three was found by comparing the total energies of the obtained structures.

10 Results and discussion

10.1 Structure of (Ba,Sr)$_2$CoIrO$_6$

The XRD-patterns of the six-membered series $(Ba,Sr)_2CoIrO_6$ show clear evolution of unit cell parameters as the Ba/Sr ratio is changed. The Sr-end of the series shows clear preference for cubic structure, with a gradual transition to hexagonal symmetry taking place about midway through the series. In the middle of the series, the two phases coexist. Phase fractions for these compounds were estimated based on relative heights for the strongest peak of each phase, assuming equal contribution of the superpositioned hexagonal $(1\ 1\ 0)_h$ + $(1\ 2\ 0)_h$ + $(2\ 1\ 0)_h$ peak as compared to the cubic $(2\ 2\ 0)_c$ peak. Calculated unit cell parameters and phase ratios are presented in Table 2.

Table 2. Unit cell parameters for samples of the $(\mathrm{Ba}_{1-x}\mathrm{Sr}_x)_2\mathrm{CoIrO}_6$ series. Phase fraction X is approximated for dual-phase samples, and tolerance parameter t is calculated based on Shannon ionic radii.

Sample (ratio)	t	Cubic / rhombohedral phase				Hexagonal phase				
		X (%)	Order	a (Å)	α (°)	X (%)	Order	a (Å)	c (Å)	γ (°)
x = 1.0	0.982	100	High	7.8390	90.21	-	-	-	-	-
x = 0.8	0.994	100	High	7.8636	90.00	-	-	-	-	-
x = 0.6	1.006	∼87	High	7.8915	90.00	∼13	?	∼5.61	∼13.85	120
x = 0.4	1.017	∼5	?	∼7.9	90.00	∼95	Yes	5.61	13.69	120
x = 0.2	1.029	-	-	-	-	100	Yes	5.683	14.092	120
x = 0.0	1.041	-	-	-	-	100	Yes	5.72	∼14.22	120

For the three dominatingly cubic samples, B site order could be determined by the appearance of the $(1\ 1\ 1)_c$ peak around 19.5° 2θ, but this peak is too weak to appear for the Ba/Sr 6:4 sample due to its low content of cubic phase. Surprisingly, the end sample Sr_2CoIrO_6, which was expected to be cubic, is found to be distorted, as evidenced by the splitting of the $(2\ 0\ 2)_c$ and $(4\ 2\ 2)_c$ peak series. Axial distortions can be immediately excluded due to the unsplit appearance of the $(2\ 0\ 0)_c$ peak series, leaving an angularly distorted pseudocubic structure as the only alternative. The asymmetric splitting indicates rhombohedral symmetry rather than monoclinic, which would produce symmetrical triplet peaks. Thereby the cubic phase is concluded to undergo an equal distortion of all unit cell angles for the Sr_2CoIrO_6 sample.

The hexagonal phase was matched to a perovskite-related structure of face-sharing octahedra with an ordered B site and 6-layer stacking of BO_6-layers along the hexagonal c-axis. [138] Hexagonal symmetry is expected, as the tolerance parameter for the Ba-end sample is found to be greater than one, and Ba_2CoIrO_6 has previously been reported hexagonal. Known structures of Ba_2CoIrO_6 and

its single perovskite sister compounds express various stacking sequences, including 12L and 5L [24,139]. Ordering of the B site can be concluded by peaks $(1\ 0\ 0)_h$ and $(0\ 0\ 3)_h$ appearing around 18° - 19° 2θ, only allowed for ordered compounds.

Although the proposed 6L structure matches the dual-phase compounds well, it still leaves some peaks unexplained and with mismatching intensities in the two Ba-richest samples. The unexplained peaks could not be matched to any realistic impurity nor to the sample holder, despite being relatively strong, for example the peak around 46.5° - 47° 2θ. It is likely that in these two samples, the BO_6-octahedral stacking follows a different sequence than described by either model examined here. A gradual transformation from cubic to hexagonal structure by increasingly dominating hexagonal BO_6-octahedral layers would explain the appearance of a series of evenly spaced peaks only for the Ba-richest two samples.

A comparison of all XRD-patterns in full width (2θ = 10° - 70°) is seen in Figure 18, and an enlargement of the main peaks is shown in Figure 19. The hexagonal model structure, developed from powder diffraction data reported by Negas *et.al.* [138], is shown in Figure 20 alongside the previously reported structure, and its structural parameters are given in detail in Appendix II.

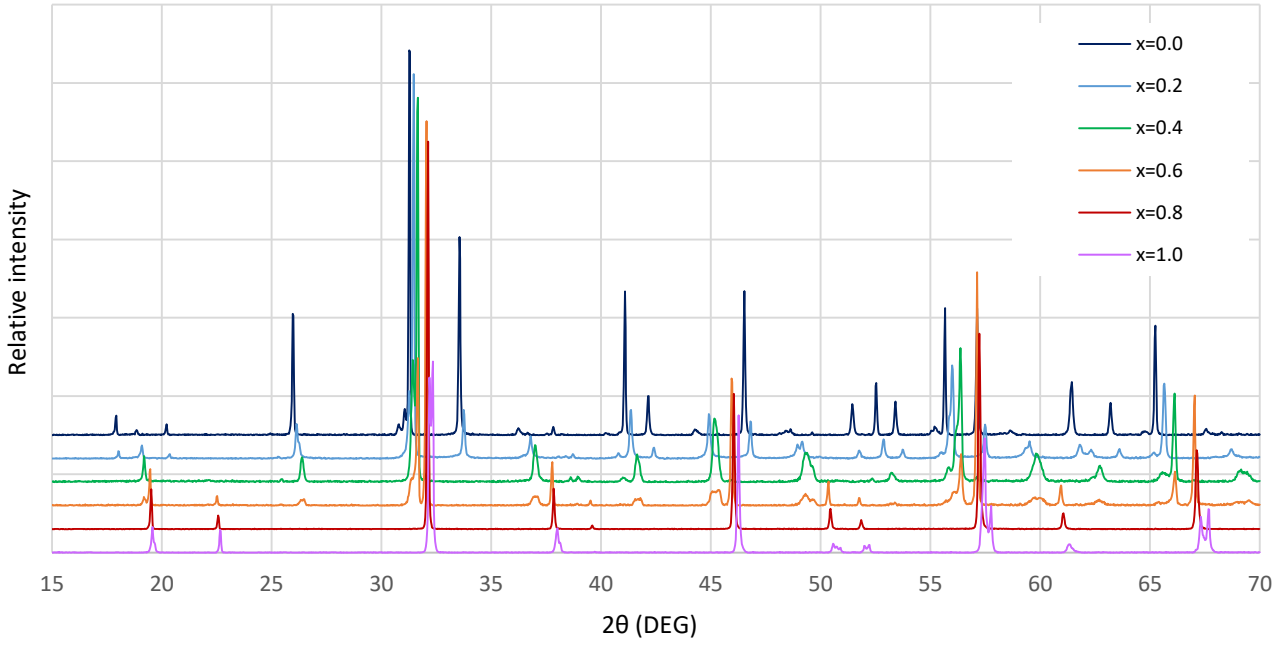

Figure 18. XRD patterns of the $(Ba_{1-x}Sr_x)_2CoIrO_6$ series, normalized according to the highest peak (splitting accounted for in Sr-end sample) and plotted from 10° to 70° 2θ.

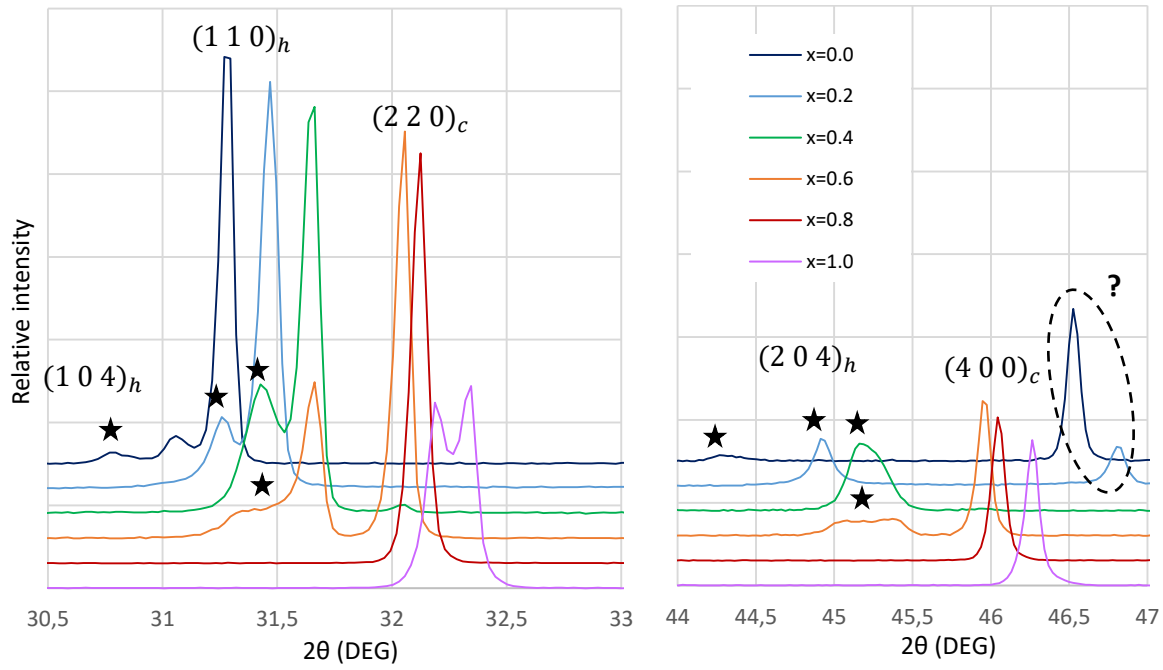

Figure 19. Excerpts of Figure 18, showing the evolution of the main peak $(2\,2\,0)_c$ to $(1\,1\,0\,)_h$ (left), and the $(2\,0\,0)_c$ peak, which remains unsplit to the Sr-end sample (right). An independent peak group associated with the hexagonal phase is marked with stars, and an unidentified peak, appearing at 46.5°-47° for the Ba-richest two samples only, is encircled in black.

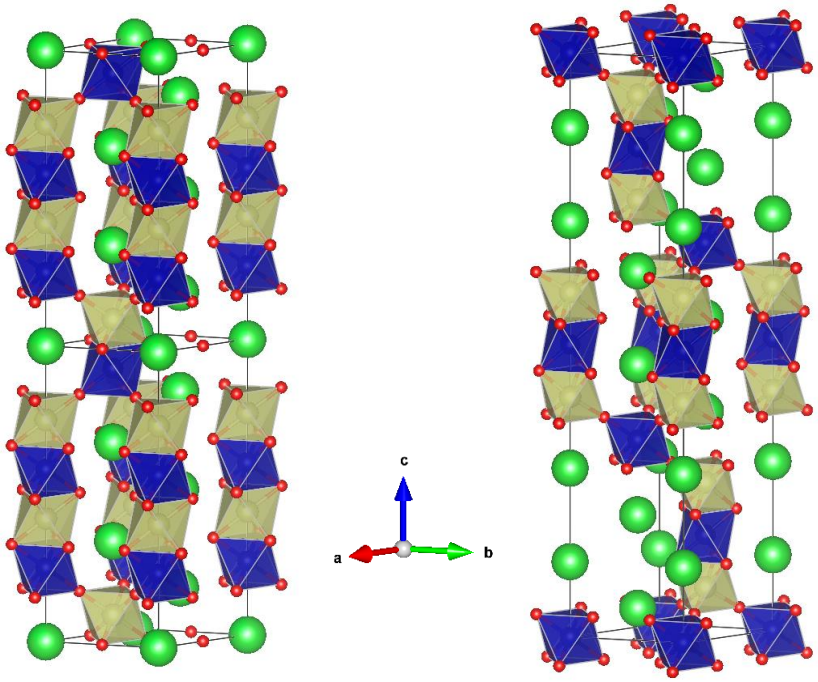

Figure 20. Assumed structure of the hexagonal phase in the Ba-rich end of the $(\mathrm{Ba,Sr})_2\mathrm{CoIrO}_6$ series (left) compared to the previously described structure of $\mathrm{Ba}_2\mathrm{CoIrO}_6$ (right). Structures drawn based on data provided by references [138] (PDF data sheet) and [24], respectively.

10.2 Structure of La_2FeIrO_3

Analysis of the La_2FeIrO_3 XRD pattern indicates the presence of two perovskite phases, of which one in clear majority, and traces of precursor impurities (lanthanum oxide and iron oxide). A mysterious peak at $2\theta = 28.30°$ was identified to originate from the silicon sample holder. Structural parameters for both perovskite phases were ultimately calculated manually after repeated failure of Rietveld refinement to converge. Due to the multiple small peaks caused by the impurity phases and silicon sample holder, determination of whether the perovskite phases are cubic or near-cubic remains imprecise. Modelling the majority phase as orthorhombic provides explanations to a larger number of the small peaks, but some of these peaks could also be explained by the presence of remnant precursors. The absence of a strong $(1\,1\,1)_c$-peak around $2\theta = 19°$ in the XRD pattern indicates a lack of long-range B site order. Only a very vague peak is found, which could originate in impurities. The XRD pattern with peaks marked according to the orthorhombic model for the majority phase is shown in Figure 21, and calculated unit cell parameters are presented in Table 3.

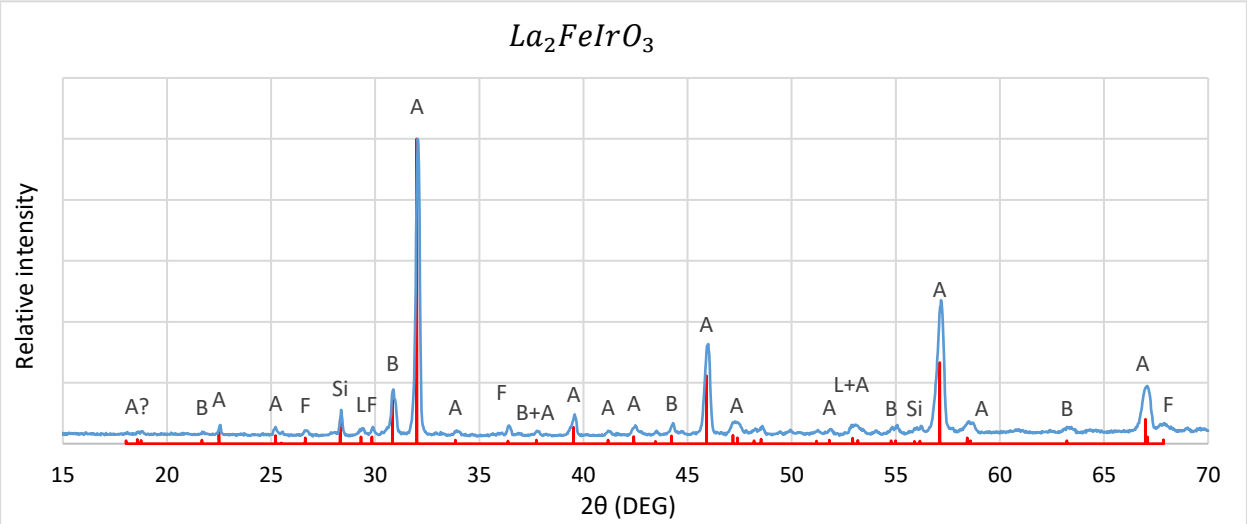

Figure 21. XRD pattern of La_2FeIrO_3. A (B) mark the majority (minority) perovskite phases, Si marks the peaks caused by the sample holder, and L (F) mark the impurity phases lanthanum oxide (iron oxide).

Table 3. Unit cell parameters of the different phases, given by manual calculation based on XDR data. Cell side lengths are scaled to a double perovskite unit cell. Phase fractions are approximate volume fractions of the total perovskite phase content, which totals ca 95% of the sample.

	a	***b***	***c***	***beta***	***fraction***
Majority (OR)	5.592 = 7.908 / $\sqrt{2}$	5.58 = 7.891 / $\sqrt{2}$	7.90	~90°	93 %
Majority (C)	7.90	7.90	7.90	90°	
Minority (C)	8.196	8.196	8.196	90°	7 %

10.3 DFT calculations of La_2FeIrO_3

The unit cell parameters obtained by DFT calculations for the orthorhombic phase are slightly larger than the ones derived from the XRD data, and vary slightly depending on the given magnetic ordering. Simulated diffraction patterns match the majority phase peaks of the experimental pattern perfectly, aside from the $(1\ 0\ 1)$ + $(0\ 1\ 1)$ peak pair at ca 19,5°, which is absent in the experimental data due to the lack of B site order in the synthesized sample. Interestingly, the AFM structure stands out as noticeably larger than the other two, and triclinic instead of monoclinic. The unit cell parameters obtained by DFT are given in Table 4.

Table 4. Unit cell parameters given by DFT calculations. Octahedral tilt is given as deviation from the linear bond along the given unit cell direction.

Magnetic order	Unit cell side lengths (Å)			Unit cell angles (°)		
	a	b	c	α	β	γ
None	5.57465	5.57136	7.89535	90.0000	89.7019	90.0000
FM	5.57744	5.57462	7.89850	90.0000	89.7037	90.0000
AFM	5.58851	5.58113	8.02326	89.9999	89.7056	89.9999

DFT calculations conclude noticeable octahedral tilting of $a^-b^-c^+$ type, with rotation angles up to 15°. The symmetry splitting in AFM results in two unequal environments per unit cell for each cation, which is reflected in the tilting of the B site octahedra as a slight difference in tilting angles. The octahedral tilting angles are shown in Table 5.

Table 5. Extent of octahedral tilting in the structural models given by DFT, expressed as deviation of the bond direction from the given crystallographic direction. For the AFM compound, angles are given separately for the unequal sites.

Magnetic order	FeO_6 tilt (°)			IrO_6 tilt (°)		
	ϕ (ab)	ϕ (-ab)	ϕ (c)	ϕ (ab)	ϕ (-ab)	ϕ (c)
None	13.4046	14.0362	15.1937	12.7289	13.2326	14.4221
FM	13.0001	13.2433	14.7290	12.7168	12.8562	14.4226
AFM	13.2646	13.5208	14.4470	12.9663	13.1129	14.3348
	13.5194	13.2916	14.4616	13.1112	12.9927	14.3215

The octahedral tilting results in strong distortion of the La site, with four bonds considerably longer than the remaining eight in nonmagnetic and FM compounds, while the AFM compound singles out three deviantly long bonds. This indicates that the effective coordination of La might be lowered, which is supported by BVS calculations suggesting strong overbonding for 12-coordinated La. Reducing the coordination to eight also yields considerably lower values for the tolerance parameter and fitness factor, which in turn explains the strong tilting. It also provides a better fit with the obtained BVS values for the B site ions, since without a reduced oxidation state of La, the suggested

combination of Fe^{3+} and Ir^{4+} would not be allowed. A combination of reduced coordination of La and partial charge transfer between all cation sites allows for a compound with oxidation states in close agreement with BVS values obtained for the AFM compound, as shown in Table 6.

Table 6. Comparison of BVS values and suggested charge structure based on bond distances given by DFT calculations. Oxygen is assumed to be precisely -2 in all charge sum calculations. *The charge of CN=8 is used for lanthanum.

Ion	BVS (non)	BVS (FM)	BVS (AFM)	Suggested charge	
La (CN=12)	(3.141)	(3.108)	(3.035)		
La (CN=9)	(2.943)	(2.903)	(2.838)		2.80
La (CN=8)	2.847	2.794	2.728	2.67	
Fe (CN=6)	3.116	2.889	2.765	2.75	2.70
Ir (CN=6)	4.620	4.146	3.898	3.91	3.80
Sum	1.430*	0.622*	0.119*	0	0

The proposed charge transfer presents several possible explanations for the phase segregation seen in experimental data. Phase segregation can occur based on differences in charge, bonding, and ionic radii. Fe^{3+} and Ir^{4+} have near-identical radii and insufficient difference in charge to induce B site ordering, let alone phase segregation. However, the proposed charge transfer between $Ir^{3/4+}$ and $La^{2/3+}$ yields a combination of charges and ionic radii well suited for the formation of a cubic minority phase $LaIrO_3$. Calculated ionic radii, tolerance parameter, and fitness factor of this phase with different charge distribution, as compared to the majority phase, are presented in Table 7.

Table 7. Structural parameters of the proposed cubic minority phase $\mathrm{La^{2+}Ir^{4+}O_3}$. The ionic radius of La^{2+} was estimated as the mean of Ba^{2+} (1.42 Å) and La^{3+} (1.19 Å) of coordination number CN = 8, and radii of mixed-valence ions were calculated as the weighted average of their integer-valence sister ions.

Phase	r(La)	r(Fe)	r(Ir)	r(O)	t	f-f
$La^{2+}Ir^{4+}O_3$	1.29	-	0.625	1.4	0.939	0.992
$La^{2.5+}Ir^{3.5+}O_3$	1.225	-	0.653	1.4	0.904	0.978
$La^{2.75+}{}_2Fe^{2.75+}Ir^{3.75+}O_3$	1.193	0.645	0.653	1.4	0.895	0.801

Antiferromagnetic ordering of the compound is supported by DFT calculations, which gives the lowest total energy for the structure with type II AFM spin alignment for the Fe site. This is in line with the structural data from the calculations, where the BVS values calculated based on the AFM compound data provide the best match for a realistic charge distribution that follows the rule of charge neutrality (Table 6). The calculated energies as compared to the nonmagnetic compound are given in Table 8, together with the calculated absolute magnetic moments μ_{abs}.

Table 8. Energies of La_2FeIrO_6 with different given magnetic order in the Fe site, as calculated with DFT assuming perfect B site ordering and no magnetic contribution from iridium. The absolute magnetic moment is given per double perovskite unit cell (four unit formulas/cell).

Order	E (Ry)	M-NON (Ry)	M-NON (eV)	AFM-FM (eV)	μ(abs) (μ_B/u.c.)
NON	-4435.92565	0	0	-	0
FM	-4436.03005	-0.10440	-1.42047	0	10
AFM (Type II)	-4436.03742	-0.11177	-1.52073	-0.10025	9.6

It is worth noting that the DFT calculations assumed the iridium site to be perfectly nonmagnetic. This holds true for Ir^{3+} in low spin, where the six electrons are evenly paired up in the t_{2g} orbitals. The fraction of potentially magnetic Ir^{4+} in the case of mixed valences also remains small and unlikely to have much impact on the overall magnetic behaviour.

10.4 Multivariate analysis of La_2FeIrO_3

Multivariate analysis yields acceptable goodness-of-fit parameters for all three PLS models (AFM, FM, and combined), presented in Table 9. Reasonably clear trends are visible in the t/t score plots and t/u plots, and the prediction plots present visible linear correlations. No frequent outliers are identified, although the small number of observations in each class results in more widespread distributions overall and lowers the precision of the models.

Table 9. Model fitness parameters for multivariate analysis PLS of FM and AFM compounds, both separately and combined in one model.

Model	A	Observations	R2X	R2Y	Q2(cum)
AFM (Class 1)	3	80	0.568	0.531	0.342
FM (Class 2)	1	92	0.24	0.37	0.305
AFM+FM	3	172	0.404	0.425	0.274

The sample La_2FeIrO_6 fits reasonably well with both of the separately calculated PLS models, somewhat grouping together with other Fe-containing compounds. Separation between FM and AFM compounds is varyingly discernible across score plots in the combined model, being most clear in the t1/t3-scores plot and *t*-to-*u* plots, in which La_2FeIrO_6 frequently places more towards the AFM group. Predicted values for all y-variables differ noticeably between the separate models for FM and AFM compounds, while the predicted values given by the combined model correspond closely with the average of the values from the separate models (Table 10). The larger absolute value of the Weiss temperature given by the AFM model indicates stronger incentive for ordering if the compound was to be AFM, but stands in contradiction to the predicted magnetic ordering temperatures, which are

higher in the FM model. This contradiction is unsurprising as one of the models should be a bad fit for the compound in question and thus present illogical predictions. Comparing the plots for predicted Weiss temperature, the combined model presents the most clearly linear trend and separation between AFM and FM groups. Based on this plot, shown in Figure 22, La_2FeIrO_6 should be antiferromagnetic.

Table 10. Predicted values for overall paramagnetic transition temperature T_C/T_N, independent magnetic ordering of the B site T_B, Weiss temperature Θ, and paramagnetic magnetization μ, for each model respectively. The values of the combined model compare well with the average value for the separate models.

Class	**T_C/T_N (K)**	**T_B (K)**	**Θ (K)**	**μ (μ_B)**
AFM	116	130	-340	2.3
FM	214	207	156	4.8
^ mean	*165*	*168.5*	*-92*	*3.55*
BOTH	160	165	-118	4.8

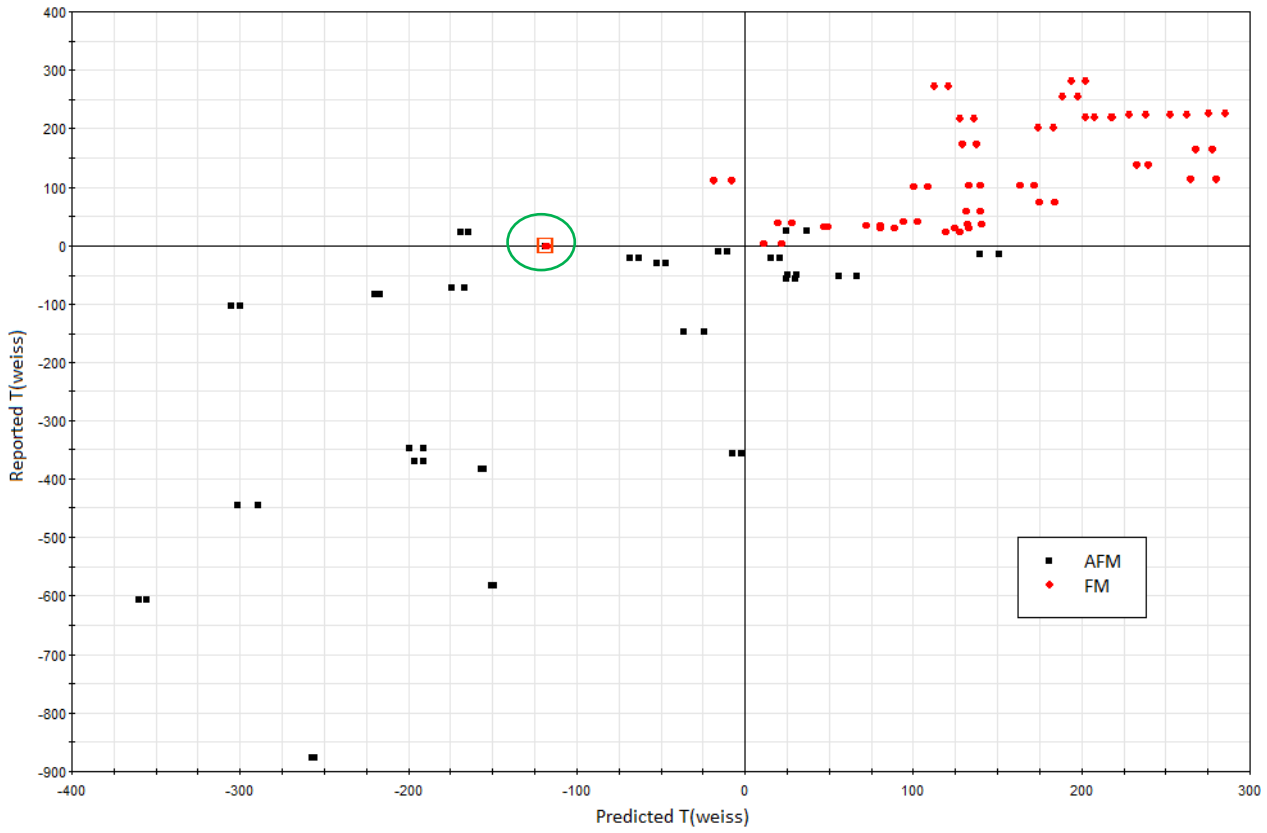

Figure 22. Reported vs predicted Weiss temperatures (Kelvin) given by the combined PLS model. AFM compounds are marked with black squares, and FM compounds with red diamonds. The location of La_2FeIrO_6 on the predicted axis is encircled in green.

11 Conclusions and suggestions

Magnetic ordering in perovskites is highly sensitive to structural parameters, which can be finely adjusted by modifications in chemical composition. The acute effect of doping on the formation and structure of the perovskite phase has been demonstrated in the $(Ba_{1-x}Sr_x)_2CoIrO_6$ series, which undergoes a transition from hexagonal to cubic as Ba^{2+} is replaced by the smaller Sr^{2+}. The transition is attributed to increasing chemical pressure as the average size of the A site ion decreases, and takes place around $x \approx 0.4 \dots 0.6$ as a gradual replacement of the hexagonal phase. The emergent phase is initially cubic, but surprisingly becomes distorted towards the Sr_2CoIrO_6 end sample, which is found to be rhombohedral. This stands in contradiction to previous reports, which have described Sr_2CoIrO_6 as cubic. The precise structure of the hexagonal phase remains unknown, as a series of peaks in the $x = 0.0$ and $x = 0.2$ samples remain unexplained by any of the previously reported structures of Ba_2CoIrO_6 [24]. Further work is thereby needed to determine the precise structure of the hexagonal phase and the details of the biphasic composition around the transition from hexagonal to cubic structure.

For comparison, a similar series could be synthesized for Ba_2CrReO_6, which presents a very similar case to Ba_2CoIrO_6 regarding tolerance parameter and 3d/5d-type assembly of elements. Due to the challenging chemistry of rhenium oxide, this sample could not be included in this study. Synthesis of Re-containing samples requires mitigating the evaporation of volatile Re_2O_7 above 350°C and careful control of the synthesis atmosphere.

Synthesis of La_2FeIrO_6 has produced a sample containing two perovskite phases, in contrast to previous reports which only identify one perovskite phase containing small amounts of precursor impurities. [128–132] The perovskite phases are identified as an orthorhombic majority phase and a cubic minority phase, the latter of which has not been identified before. Similar to previous reports, neither phase show signs of B site ordering. Optimization of the majority phase by density functional theory (DFT) calculations yields a slightly more expanded structure with considerably stronger octahedral tilting than previously described, which could be explained by the lack of focus on La_2FeIrO_6 in the previous studies. Bond valence sum (BVS) calculations based on the structural data provided by DFT suggest mixed oxidation states for all cation species, which has not been suggested before. As the sample contains iron, it would be possible to obtain further data on the charge distribution by Mössbauer spectroscopy.

The magnetic ground state of La_2FeIrO_6 is predicted to be antiferromagnetic by both multivariate analysis (MVA) and DFT, which is in agreement with the one experimental investigation found in

literature. [128,129,131] While MVA is unable to differentiate well between ordered and disordered compounds of the same stoichiometry, DFT can only evaluate the perfectly ordered phase for a given type of magnetic ordering. A previous DFT study on La_2FeIrO_6 has indicated that the AFM and FM ground states could be very close in energy. [132] Further investigations, including experimental analysis of the synthesized sample, are needed to shed more light on the magnetic behaviour of La_2FeIrO_6.

12 Summary

The magnetic behaviour of B site ordered perovskites is acutely influenced by structural parameters such as bond distances and bonding angles. Chemical composition is a determining factor for the structural parameters, and thereby presents a convenient pathway for controlling magnetic interactions. Incommensurate ionic radii introduce distortions that alter the strength of competing superexchange interactions, which determines magnetic ordering. Severely mismatched ionic radii can break the perovskite atomic interconnectivity and replace it with a hexagonal structure. Chemical substitution with a smaller species introduces chemical pressure, which can induce a phase transformation that restores the cubic perovskite structure. In the $(Ba_{1-x}Sr_x)_2CoIrO_6$ series, Ba_2CoIrO_6 forms a hexagonal phase due to Ba^{2+} being slightly too large for its site. In this report, substitution of Ba^{2+} with Sr^{2+} in $(Ba_{1-x}Sr_x)_2CoIrO_6$ has been found to induce a gradual phase transition to cubic around $x \approx 0.4 \dots 0.6$ via a hexagonal/cubic biphasic structure. Additionally, the end sample Sr_2CoIrO_6 is found to be distorted in a rhombohedral manner, in contrast to previous reports of Sr_2CoIrO_6 which describe it as cubic.

New investigations of the structure of La_2FeIrO_6 indicate the presence of a cubic perovskite minority phase, which has not been previously reported. The majority phase matches an orthogonal, antiferromagnetic phase found by density functional theory (DFT), with noticeably stronger octahedral tilting than described previously. Further investigations are needed to determine the precise compositions of the two perovskite phases and the mechanisms for their segregation.

Bond valence sum (BVS) calculations based on the structure found by DFT suggest mixed valence states for all cation species in La_2FeIrO_6, presenting a novel description of its charge distribution. This could potentially affect the magnetic properties of the phase, as the previously assumed charge distribution involves the nonmagnetic Ir^{+3} ion. Multivariate analysis is a promising novel tool in the search for novel compositions of interest. In a novel approach for predicting magnetic ordering, multivariate analysis predicts La_2FeIrO_6 to be antiferromagnetic. The same conclusion is reached by DFT, supporting the idea that 'theory-blind' statistical methods can be used for predicting properties based on chemical parameters alone. However, due to methodological weaknesses in the current work, further investigations are required to determine the definitive magnetic ordering of the compound and verify the predictions of each method.

13 References

[1] M.R. Filip, F. Giustino, The geometric blueprint of perovskites, Proc. Natl. Acad. Sci. 115 (2018) 5397–5402. doi:10.1073/pnas.1719179115.

[2] H.P. Rooksby, Compounds of the structural type of calcium titanate, Nature. 155 (1945) 484–484. doi:10.1038/155484a0.

[3] H.D. Megaw, Crystal structure of barium titanate, Nature. 155 (1945) 484–485. doi:10.1038/155484b0.

[4] B. Saparov, D.B. Mitzi, Organic-inorganic perovskites: structural versatility for functional materials design, Chem. Rev. 116 (2016) 4558–4596. doi:10.1021/acs.chemrev.5b00715.

[5] N.J. Jeon, J.H. Noh, Y.C. Kim, W.S. Yang, S. Ryu, S. Il Seok, Solvent engineering for high-performance inorganic–organic hybrid perovskite solar cells, Nat. Mater. 13 (2014) 897–903. doi:10.1038/nmat4014.

[6] F. Hao, C.C. Stoumpos, D.H. Cao, R.P.H. Chang, M.G. Kanatzidis, Lead-free solid-state organic–inorganic halide perovskite solar cells, Nat. Photonics. 8 (2014) 489–494. doi:10.1038/nphoton.2014.82.

[7] S. Vasala, M. Karppinen, A2B'B"O6 perovskites: A review, Prog. Solid State Chem. 43 (2015) 1–36. doi:10.1016/j.progsolidstchem.2014.08.001.

[8] C. Moure, O. Peña, Recent advances in perovskites: Processing and properties, Prog. Solid State Chem. 43 (2015) 123–148. doi:10.1016/j.progsolidstchem.2015.09.001.

[9] P. Wagner, G. Wackers, I. Cardinaletti, J. Manca, J. Vanacken, From colossal magnetoresistance to solar cells: An overview on 66 years of research into perovskites, Phys. Status Solidi. 214 (2017) 1700394. doi:10.1002/pssa.201700394.

[10] L.F. Schneemeyer, J. V. Waszczak, T. Siegrist, R.B. van Dover, L.W. Rupp, B. Batlogg, R.J. Cava, D.W. Murphy, Superconductivity in YBa2Cu3O7 single crystals, Nature. 328 (1987) 601–603. doi:10.1038/328601a0.

[11] K.F. Wang, J.-M. Liu, Z.F. Ren, Multiferroicity: the coupling between magnetic and polarization orders, Adv. Phys. 58 (2009) 321–448. doi:10.1080/00018730902920554.

[12] S.F. Edwards, P.W. Anderson, Theory of spin glasses, J. Phys. F Met. Phys. 5 (1975) 965–974. doi:10.1088/0305-4608/5/5/017.

[13] K.H. Fischer, Static Properties of Spin Glasses, Phys. Rev. Lett. 34 (1975) 1438–1441. doi:10.1103/PhysRevLett.34.1438.

[14] D. Sherrington, W. Southernl, Spin glass versus ferromagnet, J. Phys. F Met. Phys. 5 (1975) L49–L53. doi:10.1088/0305-4608/5/5/003.

[15] D. Sherrington, S. Kirkpatrick, Solvable Model of a Spin-Glass, Phys. Rev. Lett. 35 (1975) 1792–1796. doi:10.1103/PhysRevLett.35.1792.

[16] T. Tiittanen, M. Karppinen, Structure evolution upon chemical and physical pressure in (Sr 1−x Ba x) 2 FeSbO 6, J. Solid State Chem. 246 (2017) 245–251. doi:10.1016/j.jssc.2016.11.033.

[17] T. Aoba, T. Tiittanen, H. Suematsu, M. Karppinen, Pressure-induced phase transitions of hexagonal perovskite-like oxides, J. Solid State Chem. 233 (2016) 492–496. doi:10.1016/j.jssc.2015.11.028.

[18] Z.-K. Tan, R.S. Moghaddam, M.L. Lai, P. Docampo, R. Higler, F. Deschler, M. Price, A. Sadhanala, L.M. Pazos, D. Credgington, F. Hanusch, T. Bein, H.J. Snaith, R.H. Friend, Bright light-emitting diodes based on organometal halide perovskite, Nat. Nanotechnol. 9 (2014) 687–692. doi:10.1038/nnano.2014.149.

[19] W. Zhang, G.E. Eperon, H.J. Snaith, Metal halide perovskites for energy applications, Nat. Energy. 1 (2016) 16048. doi:10.1038/nenergy.2016.48.

[20] R.D. Shannon, Revised effective ionic radii and systematic studies of interatomic distances in halides and chalcogenides, Acta Crystallogr. Sect. A. 32 (1976) 751–767. doi:10.1107/S0567739476001551.

[21] V.M. Goldschmidt, Die Gesetze der Krystallochemie, Naturwissenschaften. 14 (1926) 477–485. doi:10.1007/BF01507527.

[22] Y. Teraoka, M.-D. Wei, S. Kagawa, Double perovskites containing hexavalent molybdenum and tungsten: synthesis, structural investigation and proposal of a fitness factor to discriminate the crystal symmetry, J. Mater. Chem. 8 (1998) 2323–2325. doi:10.1039/a806442c.

[23] P.C. Donohue, L. Katz, R. Ward, The crystal structure of barium ruthenium oxide and related compounds, Inorg. Chem. 4 (1965) 306–310. doi:10.1021/ic50025a010.

[24] J.F. Vente, P.D. Battle, Structural chemistry and electronic properties of the hexagonal perovskites BaIr(1-x)Co(x)O(3-δ) (x = 0.5, 0.7, 0.8), J. Solid State Chem. 152 (2000) 361–373. doi:10.1006/jssc.2000.8664.

[25] J. Shannon, L. Katz, A refinement of the structure of barium tantalum oxide, Ba5Ta4O15, Acta Crystallogr. Sect. B Struct. Crystallogr. Cryst. Chem. 26 (1970) 102–105. doi:10.1107/S0567740870002017.

[26] L. Pauling, The principles determining the structure of complex ionic crystals, J. Am. Chem. Soc. 51 (1929) 1010–1026. doi:10.1021/ja01379a006.

[27] C.J. Howard, H.T. Stokes, Group-theoretical analysis of octahedral tilting in perovskites, Acta Crystallogr. Sect. B Struct. Sci. 54 (1998) 782–789. doi:10.1107/S0108768198004200.

[28] A.M. Glazer, The classification of tilted octahedra in perovskites, Acta Crystallogr. Sect. B Struct. Crystallogr. Cryst. Chem. 28 (1972) 3384–3392. doi:10.1107/S0567740872007976.

[29] M. Glazer, G. Burns, Space Groups for Solid State Scientists, 3rd ed, Elsevier Science & Technology, 2013.

[30] K.S. Aleksandrov, The sequences of structural phase transitions in perovskites, Ferroelectrics. 14 (1976) 801–805. doi:10.1080/00150197608237799.

[31] N.W. Thomas, Crystal structure–physical property relationships in perovskites, Acta Crystallogr. Sect. B. 45 (1989) 337–344. doi:10.1107/S0108768189003721.

[32] N.W. Thomas, The Compositional Dependence of Octahedral Tilting in Orthorhombic and Tetragonal Perovskites, Acta Crystallogr. Sect. B Struct. Sci. 52 (1996) 16–31. doi:10.1107/S0108768195006100.

[33] N.W. Thomas, A. Beitollahi, Inter-relationship of octahedral geometry, polyhedral volume ratio and ferroelectric properties in rhombohedral perovskites, Acta Crystallogr. Sect. B. 50 (1994) 549–560. doi:10.1107/S0108768194002764.

[34] M.W. Lufaso, P.M. Woodward, Prediction of the crystal structures of perovskites using the software program SPuDS, Acta Crystallogr. Sect. B Struct. Sci. 57 (2001) 725–738. doi:10.1107/S0108768101015282.

[35] M.W. Lufaso, P.W. Barnes, P.M. Woodward, Structure prediction of ordered and disordered multiple octahedral cation perovskites using SPuDS, Acta Crystallogr. Sect. B Struct. Sci. 62 (2006) 397–410. doi:10.1107/S010876810600262X.

[36] G. King, P.M. Woodward, Cation ordering in perovskites, J. Mater. Chem. 20 (2010) 5785. doi:10.1039/b926757c.

[37] L. Landau, On the theory of phase transitions, Zhurnal Eksp. i Teor. Fiz. 7 (1937) 19–32.

[38] P.M. Woodward, Octahedral tilting in perovskites. I. Geometrical considerations, Acta Crystallogr. Sect. B Struct. Sci. 53 (1997) 32–43. doi:10.1107/S0108768196010713.

[39] P.M. Woodward, Octahedral tilting in perovskites. II. Structure stabilizing forces, Acta Crystallogr. Sect. B Struct. Sci. 53 (1997) 44–66. doi:10.1107/S0108768196012050.

[40] H.A. Jahn, E. Teller, Stability of polyatomic molecules in degenerate electronic states - I—Orbital degeneracy, Proc. R. Soc. London. Ser. A - Math. Phys. Sci. 161 (1937) 220–235. doi:10.1098/rspa.1937.0142.

[41] A.V. Vutturi, Jahn Teller distortion, (n.d.). www.adichemistry.com/inorganic/cochem/jahnteller/jahn-teller-distortion.html (accessed August 31, 2019).

[42] J. Varignon, N.C. Bristowe, E. Bousquet, P. Ghosez, Coupling and electrical control of structural, orbital and magnetic orders in perovskites, Sci. Rep. 5 (2015) 1–11. doi:10.1038/srep15364.

[43] J.-S. Zhou, J.B. Goodenough, Unusual Evolution of the Magnetic Interactions versus Structural Distortions in RMnO3 Perovskites, Phys. Rev. Lett. 96 (2006) 247202. doi:10.1103/PhysRevLett.96.247202.

[44] P.K. Davies, H. Wu, A.Y. Borisevich, I.E. Molodetsky, L. Farber, Crystal chemistry of complex perovskites: new cation-ordered dielectric oxides, Annu. Rev. Mater. Res. 38 (2008) 369–401. doi:10.1146/annurev.matsci.37.052506.084356.

[45] S. Yáñez-Vilar, M. Sánchez-Andújar, J. Rivas, M.A. Señarís-Rodríguez, Influence of the cationic ordering in the dielectric properties of the La2MnCoO6 perovskite, J. Alloys Compd. 485 (2009) 82–87. doi:10.1016/j.jallcom.2009.05.103.

[46] V.P. Sakhnenko, N. V. Ter-Oganessian, Theory of order–disorder phase transitions of B-cations in AB'1/2B''1/2O3 perovskites, Acta Crystallogr. Sect. B Struct. Sci. Cryst. Eng. Mater. 74 (2018) 264–273. doi:10.1107/S205252061800392X.

[47] A. Mu oz, J.A. Alonso, M.T. Casais, M.J. Mart nez-Lope, M.T. Fern ndez-D az, Crystal and magnetic structure of the complex oxides Sr2MnMoO6 , Sr2MnWO6 and Ca2MnWO6 : a neutron diffraction study, J. Phys. Condens. Matter. 14 (2002) 8817–8830. doi:10.1088/0953-8984/14/38/306.

[48] A.A. Colville, S. Geller, The crystal structure of brownmillerite, Ca2FeAlO5, Acta Crystallogr. Sect. B Struct. Crystallogr. Cryst. Chem. 27 (1971) 2311–2315. doi:10.1107/S056774087100579X.

[49] Y. Hosaka, N. Ichikawa, T. Saito, P. Manuel, D. Khalyavin, J.P. Attfield, Y. Shimakawa, Two-dimensional charge disproportionation of the unusual high valence state Fe4+ in a layered double perovskite, J. Am. Chem. Soc. 137 (2015) 7468–7473. doi:10.1021/jacs.5b03712.

[50] Y.H. Huang, M. Karppinen, H. Yamauchi, J.B. Goodenough, Systematic studies on effects of cationic ordering on structural and magnetic properties in Sr2FeMoO6, Phys. Rev. B. 73 (2006) 104408. doi:10.1103/PhysRevB.73.104408.

[51] C. Meneghini, S. Ray, F. Liscio, F. Bardelli, S. Mobilio, D.D. Sarma, Nature of "Disorder" in the Ordered Double Perovskite Sr2FeMoO6, Phys. Rev. Lett. 103 (2009) 046403. doi:10.1103/PhysRevLett.103.046403.

[52] B.P. Uberuaga, L.J. Vernon, Interstitial and vacancy mediated transport mechanisms in perovskites: A comparison of chemistry and potentials, Solid State Ionics. 253 (2013) 18–26. doi:10.1016/j.ssi.2013.08.022.

[53] R. Kagimura, D.J. Singh, Ab initio study of Pb antisite defects in PbZrO3 and Pb(Zr,Ti)O3, Phys. Rev. B. 78 (2008) 174105. doi:10.1103/PhysRevB.78.174105.

[54] R. Phatak, S.K. Gupta, K. Krishnan, S.K. Sali, S. V. Godbole, A. Das, Crystallographic site swapping of La3+ ion in BaA'LaTeO6 (A' = Na, K, Rb) double perovskite type compounds: Diffraction and photoluminescence evidence for the site swapping, Dalt. Trans. 43 (2014) 3306–3312. doi:10.1039/c3dt52032c.

[55] C. Sakai, Y. Doi, Y. Hinatsu, K. Ohoyama, Magnetic properties and neutron diffraction study of double perovskites Ca2LnRuO6 (Ln = Y, La–Lu), J. Phys. Condens. Matter. 17 (2005) 7383–7394. doi:10.1088/0953-8984/17/46/022.

[56] C. Sakai, Y. Doi, Y. Hinatsu, Crystal structures and magnetic properties of double perovskite compounds Ca2LnRuO6 (Ln=Y, La–Lu), J. Alloys Compd. 408–412 (2006) 608–612. doi:10.1016/j.jallcom.2004.12.068.

[57] B.S. Guiton, P.K. Davies, Nano-chessboard superlattices formed by spontaneous phase separation in oxides, Nat. Mater. 6 (2007) 586–591. doi:10.1038/nmat1953.

[58] D.E. Cox, A.W. Sleight, Crystal structure of Ba2Bi3+Bi5+O6, Solid State Commun. 19 (1976) 969–973. doi:10.1016/0038-1098(76)90632-3.

[59] J. Matsuno, M. Seto, S. Kitao, Y. Kobayashi, R. Haruki, T. Mitsui, A. Fujimori, Y. Takeda, S. Kawasaki, Effects of charge disproportionation on the phonon density of states in Fe perovskites, J. Phys. Soc. Japan. 73 (2004) 2768–2770. doi:10.1143/JPSJ.73.2768.

[60] Y.W. Long, N. Hayashi, T. Saito, M. Azuma, S. Muranaka, Y. Shimakawa, Temperature-induced A–B intersite charge transfer in an A-site-ordered LaCu3Fe4O12 perovskite, Nature. 458 (2009) 60–63. doi:10.1038/nature07816.

[61] G. Thornton, A.J. Jacobson, A neutron diffraction determination of the structures of Ba2SbVBiIIIO6 and Ba2BiVBiIIIO6, Acta Crystallogr. Sect. B Struct. Crystallogr. Cryst. Chem. 34 (1978) 351–354. doi:10.1107/S056774087800312X.

[62] P.M. Woodward, D.E. Cox, E. Moshopoulou, A.W. Sleight, S. Morimoto, Structural studies of charge disproportionation and magnetic order in CaFeO3, Phys. Rev. B. 62 (2000) 844–855. doi:10.1103/PhysRevB.62.844.

[63] J.A. Alonso, J.L. García-Muñoz, M.T. Fernández-Díaz, M.A.G. Aranda, M.J. Martínez-Lope, M.T. Casais, Charge disproportionation in RNiO3 perovskites: Simultaneous metal-insulator and structural transition in YNiO3, Phys. Rev. Lett. 82 (1999) 3871–3874. doi:10.1103/PhysRevLett.82.3871.

[64] J.R. Hayes, A.P. Grosvenor, An investigation of the Fe and Mo oxidation states in Sr2Fe2-xMoxO6 (0.25 ≤ x ≤ 1.0) double perovskites by X-ray absorption spectroscopy, J. Alloys Compd. 537 (2012) 323–331. doi:10.1016/j.jallcom.2012.05.056.

[65] J. Lindén, T. Yamamoto, M. Karppinen, H. Yamauchi, T. Pietari, Evidence for valence fluctuation of Fe in Sr2FeMoO6-w double perovskite, Appl. Phys. Lett. 76 (2000) 2925–2927. doi:10.1063/1.126518.

[66] K. Kuepper, M. Raekers, C. Taubitz, H. Hesse, M. Neumann, A.T. Young, C. Piamonteze, F. Bondino, K.C. Prince, Fe valence state of Sr2FeMoO6 probed by x-ray absorption spectroscopy: The sample age matters, J. Appl. Phys. 104 (2008) 4–7. doi:10.1063/1.2955749.

[67] Y.-H. Huang, G. Liang, M. Croft, M. Lehtimäki, M. Karppinen, J.B. Goodenough, Double-Perovskite Anode Materials Sr 2 MMoO 6 (M = Co, Ni) for Solid Oxide Fuel Cells, Chem. Mater. 21 (2009) 2319–2326. doi:10.1021/cm8033643.

[68] A. Nishiyama, Y. Doi, Y. Hinatsu, Magnetic interactions in rhenium-containing rare earth double perovskites Sr2LnReO6(Ln=rare earths), J. Solid State Chem. 248 (2017) 134–141. doi:10.1016/j.jssc.2017.02.006.

[69] F. Mezzadri, D. Delmonte, F. Orlandi, C. Pernechele, G. Calestani, M. Solzi, M. Lantieri, G. Spina, R. Cabassi, F. Bolzoni, M. Fittipaldi, M. Merlini, A. Migliori, P. Manuel, E. Gilioli, Structural and magnetic characterization of the double perovskite Pb2FeMoO6, J. Mater. Chem. C. 4 (2016) 1533–1542. doi:10.1039/c5tc03529e.

[70] N.S. Fedorova, Y.W. Windsor, C. Findler, M. Ramakrishnan, A. Bortis, L. Rettig, K. Shimamoto, E.M. Bothschafter, M. Porer, V. Esposito, Y. Hu, A. Alberca, T. Lippert, C.W. Schneider, U. Staub, N.A. Spaldin, Relationship between crystal structure and multiferroic orders in orthorhombic perovskite manganites, Phys. Rev. Mater. 2 (2018) 104414. doi:10.1103/PhysRevMaterials.2.104414.

[71] J. Kreiselt, A.M. Glazer, G. Jones, P.A. Thomas, L. Abello, G. Lucazeau, An x-ray diffraction and Raman spectroscopy investigation of A-site substituted perovskite compounds: The (Na1-xKx)0.5Bi0.5TiO3 (0 ≤ x ≤ 1) solid solution, J. Phys. Condens. Matter. 12 (2000) 3267–3280. doi:10.1088/0953-8984/12/14/305.

[72] R. Morrow, J. Yan, M.A. McGuire, J.W. Freeland, D. Haskel, P.M. Woodward, Effects of chemical pressure on the magnetic ground states of the osmate double perovskites SrCaCoOsO6 and Ca2CoOsO6, Phys. Rev. B - Condens. Matter Mater. Phys. 92 (2015) 1–7. doi:10.1103/PhysRevB.92.094435.

[73] B.E. Day, N.D. Bley, H.R. Jones, R.M. McCullough, H.W. Eng, S.H. Porter, P.M. Woodward, P.W. Barnes, Structures of ordered tungsten- or molybdenum-containing quaternary perovskite oxides, J. Solid State Chem. 185 (2012) 107–116. doi:10.1016/j.jssc.2011.11.007.

[74] P.W. Barnes, M.W. Lufaso, P.M. Woodward, Structure determination of A2M3+TaO6 and A2M3+NbO6 ordered perovskites: octahedral tilting and pseudosymmetry., Acta Crystallogr. B. 62 (2006) 384–396. doi:10.1107/S0108768106002448.

[75] V.M. Katukuri, P. Babkevich, O. Mustonen, H.C. Walker, B. Fåk, S. Vasala, M. Karppinen, H.M. Rønnow, O. V. Yazyev, Exchange Interactions Mediated by Non-Magnetic Cations in Double Perovskites, (2019) 1–6.

[76] M.S. Senn, W.T. Chen, T. Saito, S. García-Martín, J.P. Attfield, Y. Shimakawa, B-cation order control of magnetism in the 1322 perovskite CaCu3Fe2Nb2O12, Chem. Mater. 26 (2014) 4832–4837. doi:10.1021/cm502064b.

[77] L. Karvonen, M. Valkeapää, R.-S. Liu, J.-M. Chen, H. Yamauchi, M. Karppinen, O- K and Co- L XANES Study on Oxygen Intercalation in Perovskite SrCoO 3-δ, Chem. Mater. 22 (2010) 70–76. doi:10.1021/cm9021563.

[78] L. Karvonen, S. Yoon, P. Hug, H. Yamauchi, A. Weidenkaff, M. Karppinen, The n=3 member of the SrCoO(3n−1)/n series of layered oxygen-defect perovskites, Mater. Res. Bull. 46 (2011) 1340–1345. doi:10.1016/j.materresbull.2011.05.028.

[79] L. Karvonen, S. Räsänen, H. Yamauchi, M. Karppinen, Chemical Oxidation of SrCoO3−δ, Chem. Lett. 36 (2007) 1176–1177. doi:10.1246/cl.2007.1176.

[80] S. Royer, H. Alamdari, D. Duprez, S. Kaliaguine, Oxygen storage capacity of La1−xA'xBO3 perovskites (with A'=Sr, Ce; B=Co, Mn)—relation with catalytic activity in the CH4 oxidation reaction, Appl. Catal. B Environ. 58 (2005) 273–288. doi:10.1016/j.apcatb.2004.12.010.

[81] N. Guilhaume, M. Primet, Three-Way Catalytic Activity and Oxygen Storage Capacity of Perovskite LaMn0.976Rh0.024O3+δ, J. Catal. 165 (1997) 197–204. doi:10.1006/jcat.1997.1481.

[82] Y. Doi, M. Wakeshima, K. Tezuka, Y.J. Shan, K. Ohoyama, S. Lee, S. Torii, T. Kamiyama, Y. Hinatsu, Crystal structures, magnetic properties, and DFT calculation of B-site defected 12L-perovskites Ba2La2MW2O12 (M = Mn, Co, Ni, Zn), J. Phys. Condens. Matter. 29 (2017) 365802. doi:10.1088/1361-648X/aa7c9b.

[83] K. Onodera, T. Kogawa, M. Matsukawa, H. Taniguchi, K. Nishidate, A. Matsushita, M. Shimoda, Magnetic, thermodynamic and optical properties of Sb-substituted Ba2PrBiO6 double perovskite oxides, J. Phys. Conf. Ser. 969 (2018). doi:10.1088/1742-6596/969/1/012122.

[84] Y. Doi, Y. Hinatsu, K. Ohoyama, Structural and magnetic properties of pseudo-two-dimensional triangular antiferromagnets Ba3MSb2O9 (M = Mn, Co, and Ni), J. Phys. Condens. Matter. 16 (2004) 8923–8935. doi:10.1088/0953-8984/16/49/009.

[85] C. Artini, Crystal chemistry, stability and properties of interlanthanide perovskites: A review, J. Eur. Ceram. Soc. 37 (2017) 427–440. doi:10.1016/j.jeurceramsoc.2016.08.041.

[86] J.M.D. Coey, Magnetism and Magnetic Materials, Cambridge University Press, 2009.

[87] L. Guo, Y. Bai, C. Huang, W. Ma, Revisiting La 2 MMnO 6 (M = Co, Ni, Cu, Zn) perovskites in view of 3d-electron configuration, J. Appl. Phys. 124 (2018) 065103. doi:10.1063/1.5021975.

[88] T.D. Rao, S. Marik, D. Singh, R.P. Singh, Observation of exchange bias effect in La2NiIrO6, J. Alloys Compd. 705 (2017) 849–852. doi:10.1016/j.jallcom.2017.02.115.

[89] R.O. Kuzian, V. V. Laguta, J. Richter, Lieb-Mattis ferrimagnetic superstructure and superparamagnetism in Fe-based double perovskite multiferroics, Phys. Rev. B. 90 (2014) 134415. doi:10.1103/PhysRevB.90.134415.

[90] E.O. Wollan, W.C. Koehler, Neutron diffraction study of the magnetic properties of the series of perovskite-type compounds, Phys. Rev. 100 (1955) 545–563. doi:10.1103/PhysRev.100.545.

[91] A. Yoshimori, A new type of antiferromagnetic structure in the rutile type crystal, J. Phys. Soc. Japan. 14 (1959) 807–821. doi:10.1143/JPSJ.14.807.

[92] G. Grosso, G.P. Parravicini, Solid State Physics, 2nd ed., 2013.

[93] H. Dersch, G. Blatter, New critical-state model for critical currents in ceramic high-Tc superconductors, Phys. Rev. B. 38 (1988) 11391–11404. doi:10.1103/PhysRevB.38.11391.

[94] Y. Fei, M. Iqbal, S.D. Kong, Z. Xue, C.P. McFadden, J.L. Guillet, L.H. Doerrer, E.E. Alp, W. Bi, Y. Lu, C.B. Dandamudi, P.J. Ranganath, K.J. Javier, M. Ahmadian, C.J. Ellison, K.P. Johnston, Aqueous

superparamagnetic magnetite dispersions with ultrahigh initial magnetic susceptibilities, Langmuir. 34 (2018) 622–629. doi:10.1021/acs.langmuir.7b03702.

[95] R.B. Griffiths, Nonanalytic Behavior Above the Critical Point in a Random Ising Ferromagnet, Phys. Rev. Lett. 23 (1969) 17–19. doi:10.1103/PhysRevLett.23.17.

[96] Y. Shimakawa, M. Mizumaki, Multiple magnetic interactions in A-site-ordered perovskite-structure oxides, J. Phys. Condens. Matter. 26 (2014). doi:10.1088/0953-8984/26/47/473203.

[97] J.B. Goodenough, Theory of the Role of Covalence in the Perovskite-Type Manganites [La,M(II)]MnO3, Phys. Rev. 100 (1955) 564–573. doi:10.1103/PhysRev.100.564.

[98] J. Kanamori, Superexchange interaction and symmetry properties of electron orbitals, J. Phys. Chem. Solids. 10 (1959) 87–98. doi:10.1016/0022-3697(59)90061-7.

[99] Y. Shi, Y. Guo, S. Yu, M. Arai, A. Sato, A.A. Belik, K. Yamaura, E. Takayama-Muromachi, Crystal growth and structure and magnetic properties of the 5d oxide Ca3LiOsO6: extended superexchange magnetic interaction in oxide, J. Am. Chem. Soc. 132 (2010) 8474–8483. doi:10.1021/ja102606q.

[100] Z. Fang, K. Terakura, J. Kanamori, Strong ferromagnetism and weak antiferromagnetism in double perovskites: Sr2FeMO6 (M=Mo, W, and Re), Phys. Rev. B. 63 (2001) 180407. doi:10.1103/PhysRevB.63.180407.

[101] H.L. Feng, S. Calder, M.P. Ghimire, Y.H. Yuan, Y. Shirako, Y. Tsujimoto, Y. Matsushita, Z. Hu, C.Y. Kuo, L.H. Tjeng, T.W. Pi, Y.L. Soo, J. He, M. Tanaka, Y. Katsuya, M. Richter, K. Yamaura, Ba2NiOsO6: A Dirac-Mott insulator with ferromagnetism near 100 K, Phys. Rev. B. 235158 (2016) 1–9. doi:10.1103/PhysRevB.94.235158.

[102] L.M. Levinson, M. Luban, S. Shtrikman, Microscopic Model for Reorientation of the Easy Axis of Magnetization, Phys. Rev. 187 (1969) 715–722. doi:10.1103/PhysRev.187.715.

[103] R. Morrow, R. Mishra, O.D. Restrepo, M.R. Ball, W. Windl, S. Wurmehl, U. Stockert, B. Büchner, P.M. Woodward, Independent ordering of two interpenetrating magnetic sublattices in the double perovskite Sr2CoOsO6, J. Am. Chem. Soc. 135 (2013) 18824–18830. doi:10.1021/ja407342w.

[104] S. Gangopadhyay, W.E. Pickett, Spin-orbit coupling, strong correlation, and insulator-metal transitions: The Jeff= 32 ferromagnetic Dirac-Mott insulator Ba2NaOsO6, Phys. Rev. B - Condens. Matter Mater. Phys. 91 (2015) 19–21. doi:10.1103/PhysRevB.91.045133.

[105] B. Yan, A.K. Paul, S. Kanungo, M. Reehuis, A. Hoser, D.M. Többens, W. Schnelle, R.C. Williams, T. Lancaster, F. Xiao, J.S. Möller, S.J. Blundell, W. Hayes, C. Felser, M. Jansen, Lattice-site-specific spin dynamics in double perovskite Sr2CoOsO6, Phys. Rev. Lett. 112 (2014) 1–6. doi:10.1103/PhysRevLett.112.147202.

[106] A. Prodi, E. Gilioli, A. Gauzzi, F. Licci, M. Marezio, F. Bolzoni, Q. Huang, A. Santoro, J.W. Lynn, Charge, orbital and spin ordering phenomena in the mixed valence manganite (NaMn3+3)(Mn3+2Mn4+2)O12, Nat. Mater. 3 (2004) 48–52. doi:10.1038/nmat1038.

[107] X. Ding, B. Gao, E. Krenkel, C. Dawson, J.C. Eckert, S.-W. Cheong, V. Zapf, Magnetic properties of double perovskite Ln2CoIrO6 (Ln=Eu, Tb, Ho): hetero-tri-spin 3d-5d-4f systems, Phys. Rev. B. 99 (2019) 014438. doi:10.1103/PhysRevB.99.014438.

[108] C.R. Wiebe, J.E. Greedan, G.M. Luke, J.S. Gardner, Spin-glass behavior in the S=1/2 fcc ordered perovskite Sr2CaReO6, Phys. Rev. B. 65 (2002) 144413. doi:10.1103/PhysRevB.65.144413.

[109] J. Snyder, J.S. Slusky, R.J. Cava, P. Schiffer, How 'spin ice' freezes, Nature. 413 (2001) 48–51. doi:10.1038/35092516.

[110] O. Mustonen, S. Vasala, E. Sadrollahi, K.P. Schmidt, C. Baines, H.C. Walker, I. Terasaki, F.J. Litterst, E. Baggio-Saitovitch, M. Karppinen, Spin-liquid-like state in a spin-1/2 square-lattice antiferromagnet perovskite induced by d10–d0 cation mixing, Nat. Commun. 9 (2018) 1085. doi:10.1038/s41467-018-03435-1.

[111] R. Morrow, J.W. Freeland, P.M. Woodward, Probing the links between structure and magnetism in Sr2-xCaxFeOsO6 double perovskites, Inorg. Chem. 53 (2014) 7983–7992. doi:10.1021/ic5006715.

[112] I. Yamada, K. Takata, N. Hayashi, S. Shinohara, M. Azuma, S. Mori, S. Muranaka, Y. Shimakawa, M. Takano, A perovskite containing quadrivalent iron as a charge-disproportionated ferrimagnet, Angew. Chemie Int. Ed. 47 (2008) 7032–7035. doi:10.1002/anie.200801482.

[113] C. Zener, Interaction between the s-shells in the transition metals. II. Ferromagnetic compounds of manganese with perovskite structure, Phys. Rev. 82 (1951) 403–405. doi:10.1103/PhysRev.82.403.

[114] R.A. de Groot, F.M. Mueller, P.G. van Engen, K.H.J. Buschow, New class of materials: half-metallic ferromagnets, Phys. Rev. Lett. 50 (1983) 2024–2027. doi:10.1103/PhysRevLett.50.2024.

[115] J.-H. Park, E. Vescovo, H.-J. Kim, C. Kwon, R. Ramesh, T. Venkatesan, Direct evidence for a half-metallic ferromagnet, Nature. 392 (1998) 794–796. doi:10.1038/33883.

[116] O. Mustonen, S. Vasala, T.-L. Chou, J.-M. Chen, M. Karppinen, Competition between ferromagnetism and antiferromagnetism in the rutile Cr1-xVxO2 system, Phys. Rev. B. 93 (2016) 014405. doi:10.1103/PhysRevB.93.014405.

[117] R.I. Dass, J.B. Goodenough, Multiple magnetic phases of La2CoMnO6−δ, Phys. Rev. B. 67 (2003) 014401. doi:10.1103/PhysRevB.67.014401.

[118] L. Eriksson, T. Byrne, E. Johansson, J. Trygg, C. Vikström, Multi- and megavariate data analysis: Basic principles and applications, 3rd ed., Umetrics Academy, Sweden, 2013.

[119] F. Giustino, Materials Modelling Using Density Functional Theory: Properties and Predictions, Oxford University Press, Incorporated, 2014.

[120] E. Schrödinger, Quantisierung als Eigenwertproblem, erste Mitteilung, Ann. Phys. 384 (1926) 489–527. doi:10.1002/andp.19263840602.

[121] X. Xu, W.A. Goddard, The extended Perdew-Burke-Ernzerhof functional with improved accuracy for thermodynamic and electronic properties of molecular systems, J. Chem. Phys. 121 (2004) 4068–4082. doi:10.1063/1.1771632.

[122] J.P. Perdew, K. Burke, M. Ernzerhof, Generalized Gradient Approximation made simple, Phys. Rev. Lett. 77 (1996) 3865–3868. doi:10.1103/PhysRevLett.77.3865.

[123] J.P. Perdew, K. Burke, M. Ernzerhof, Generalized Gradient Approximation sade simple [Phys. Rev. Lett. 77, 3865 (1996)], Phys. Rev. Lett. 78 (1997) 1396–1396. doi:10.1103/PhysRevLett.78.1396.

[124] N. Imamura, T. Mizoguchi, H. Yamauchi, M. Karppinen, Multivariate data analysis approach to understand magnetic properties of perovskite manganese oxides, J. Solid State Chem. 181 (2008) 1195–1203. doi:10.1016/j.jssc.2008.02.025.

[125] A.W. Sleight, J. Longo, R. Ward, Compounds of osmium and rhenium with the ordered perovskite structure, Inorg. Chem. 1 (1962) 245–250. doi:10.1021/ic50002a010.

[126] T. Tiittanen, M. Karppinen, Structure evolution upon chemical and physical pressure in (Sr1−xBax)2FeSbO6, J. Solid State Chem. 246 (2017) 245–251. doi:10.1016/j.jssc.2016.11.033.

[127] M. Uhl, S.F. Matar, B. Siberchicot, Calculated magnetic and electronic properties of the double perovskites La2TIrO6 (T=Mn, Fe, Co), J. Magn. Magn. Mater. 187 (1998) 201–209. doi:10.1016/S0304-8853(98)00122-X.

[128] L. Bufaiçal, L. Mendonça Ferreira, R. Lora-Serrano, O. Agüero, I. Torriani, E. Granado, P.G. Pagliuso, A. Caytuero, E. Baggio-Saitovich, Physical properties of disordered double-perovskite Ca2−xLaxFeIrO6, J. Appl. Phys. 103 (2008) 07F716. doi:10.1063/1.2830719.

[129] L. Bufaiçal, L. Mendonça Ferreira, R. Lora-Serrano, P.G. Pagliuso, A. Caytuero, E. Baggio-Saitovich, The role of cationic disorder on the magnetic properties of double perovskites (Ca, Sr)2 - x Lax FeIrO6, Phys. B Condens. Matter. 404 (2009) 3285–3288. doi:10.1016/j.physb.2009.07.096.

[130] L. Bufaiçal, C. Adriano, R. Lora-Serrano, J.G.S. Duque, L. Mendonça-Ferreira, C. Rojas-Ayala, E. Baggio-Saitovitch, E.M. Bittar, P.G. Pagliuso, Structural, electronic and magnetic properties of the series of double perovskites (Ca, Sr)2-xLaxFeIrO6, J. Solid State Chem. 212 (2014) 23–29. doi:10.1016/j.jssc.2014.01.007.

[131] L. Bufaiçal, L.T. Coutrim, T.O. Santos, H. Terashita, C.B.R. Jesus, P.G. Pagliuso, E.M. Bittar, Physical properties of Sr2FeIrO6 and Sr1.2La0.8FeIrO6 double perovskites obtained by a new synthesis route, Mater. Chem. Phys. 182 (2016) 459–465. doi:10.1016/j.matchemphys.2016.07.057.

[132] H.R. Fuh, K.C. Weng, Y.P. Liu, Y.K. Wang, New ferromagnetic semiconductor double perovskites: La2FeMO6 (M = Co, Rh, and Ir), J. Alloys Compd. 622 (2015) 657–661. doi:10.1016/j.jallcom.2014.10.010.

[133] H. Putz, MATCH! Phase Identification from Powder Diffraction, (2017).

[134] J. Rodriguez-Carvajal, FullProf, (2018).

[135] K. Momma, F. Izumi, Visualization for Electronic and Structural Analysis (VESTA), (2017).

[136] Simca P+, (2013).

[137] Quantum Espresso, (2018).

[138] T. Negas, R.S. Roth, Phase equilibria and structural relations in the system BaMnO3−x, J. Solid State Chem. 3 (1971) 323–339. doi:10.1016/0022-4596(71)90068-5.

[139] M. Parras, A. Varela, H. Seehofer, J.M. González-Calbet, HREM Study of the BaCoO3-y System: Evidence for a New 5H Phase, J. Solid State Chem. 120 (1995) 327–331. doi:10.1006/jssc.1995.1416.

[140] I.D. Brown, Accumulated table of bond valence parameters, (2016).

[141] M.E. Jamer, Y.J. Wang, G.M. Stephen, I.J. McDonald, A.J. Grutter, G.E. Sterbinsky, D.A. Arena, J.A. Borchers, B.J. Kirby, L.H. Lewis, B. Barbiellini, A. Bansil, D. Heiman, Compensated ferrimagnetism in the zero-moment Heusler alloy Mn3Al, Phys. Rev. Appl. 7 (2017) 064036. doi:10.1103/PhysRevApplied.7.064036.

[142] E. Lieb, D. Mattis, Ordering energy levels of interacting spin systems, J. Math. Phys. 3 (1962) 749–751. doi:10.1063/1.1724276.

14 Appendices

Appendix I. Variables in MVA

Table 11. Input variables for multivariate analysis by MVA, their meaning, values, and calculated importance for the model. These served as the X-variables in the model.

Variable	Parameter	Values	Variable importance score
norm-a norm-b norm-c	Unit cell parameters normalized to pseudocubic setting	numeric	0.35 … 0.69
par-alpha par-beta par-gamma	Unit cell parameters α / β / γ	numeric	~1.20
c/a	Pseudocubic ratio c/a	numeric	1.11
V(red)	Unit cell volume (cubic normalized)	numeric	0.53
%d(V)	Unit cell volume compared to ideal volume	numeric	0.48
ch(A)	Charge of the A site	numeric	1.08
ch(B') ch(B'')	Charge of the B sites (absolute)	numeric	0.44
d-ch(B)	Charge of the B sites (difference)	numeric	1.28
r(A) r(B') r(B'')	Radii of cations A and B	numeric	0.21 … 0.60
m-r(B)	Radius of B sites (average)	numeric	0.44
d-rB	Radius of the B sites (difference; absolute)	numeric	0.76
%d-rB	Radius of the B sites (difference; percentual)	numeric	0.85
t-par	Tolerance parameter	numeric	0.56
f-f	Fitness factor	numeric	0.58
X(A) X(B') X(B'')	Electronegativity of the A / B sites	numeric	0.37 … 0.65
m-X(B)	Electronegativity of the B sites (average)	numeric	0.62
d-X(B)	Electronegativity of the B sites (difference)	numeric	0.59
Ei(A)	Ionization energy of the A site (absolute)	numeric	1.24
Ei(B') Ei(B'')	Ionization energy of the B sites (absolute)	numeric	0.42
m-Ei(B)	Ionization energy of the B sites (average)	numeric	1.13
d-Ei(B)	Ionization energy of the B sites (difference)	numeric	1.33
order-deg	Degree of B site order	numeric	1.26
f(A) d(A) d(B') d(B'')	Valence electrons in the f / d orbitals	integer	0.42 … 0.64
magn A magn B' magn B''	Magnetic behaviour of A & B sites	AFM / FM / PM / NULL	0.35 … 0.63 2.27 … 2.42
syn-T max	Maximal synthesis temperature	numeric	0.69
syn-t(h)	Synthesis time	integer	0.36
A-O	Bond distances to oxygen	numeric	0.39 … 0.60

B'-O B''-O			
BVS A-O BVS B'-O BVS B''-O	Bond valence sums of cations	numeric	$0.18 \dots 0.33$
%m-dev(BOB)	Deviation from 180° of average B-O-B bond angle (fraction)	numeric	0.47

Table 12. Input variables for multivariate analysis by MVA, their meaning, values, and calculated importance for the model. These served as the Y-variables in the model.

Variable	Parameter	Values
T(weiss)	Weiss temperature of the sample	numeric
T-trans T-trans(B') T-trans(B'')	magnetic transition temperature for the whole sample and the separate B site ions, respectively	numeric
μeff	effective total magnetic moment of the sample	numeric

Table 13. The structure of La_2FeIrO_6 given as the starting point for DFT calculations. The structure is given in semiorthorhombic setting with lattice parameters $a = 5.5360$ Å, $b = 5.5604$ Å, $c = 7.8249$, and $\beta = 89.80°$

Atom	x	y	z	occupancy
La	0.5148	0.4817	0.2541	1
La	0.4852	0.5183	0.7459	1
La	0.9852	0.9817	0.2459	1
La	0.0148	0.0183	0.7541	1
O1	0.2359	0.1971	0.0361	1
O1	0.7641	0.8029	0.9639	1
O1	0.2641	0.6971	0.4639	1
O1	0.7359	0.3029	0.5361	1
O2	0.236	0.7807	0.0274	1
O2	0.764	0.2193	0.9726	1
O2	0.264	0.2807	0.4726	1
O2	0.736	0.7193	0.5274	1
O3	0.5647	0.0024	0.255	1
O3	0.4353	0.9976	0.745	1
O3	0.9353	0.5024	0.245	1
O3	0.0647	0.4976	0.755	1
Fe	0	0.5	0	1
Fe	0.5	0	0.5	1
Ir	0.5	0	0	1
Ir	0	0.5	0.5	1

Appendix II. Structure of $(Ba,Sr)_2CoIrO_6$

Table 14. Atomic positions for the hexagonal structure shown in Figure 20. The positions are given for the disordered compound with space group $P\bar{6}m2$, from which the ordered compound is derived by alternating the identity of the B site ions in layers along the c direction. The proposed structure of the hexagonal phase is developed from data given by Negas et.al. [138].

Atom	Wyckoff	x	y	z
Ba 1	1 a	0.0000	0.0000	0.0000
Ba 2	1 d	0.3333	0.6667	0.5000
Ba 3	2 i	0.6667	0.3333	0.3333
Ba 4	2 h	0.3333	0.6667	0.1670
Co / Ir 1	2 g	0.0000	0.0000	0.2500
Co / Ir 2	2 g	0.0000	0.0000	0.4170
Co / Ir 3	2 i	0.6667	0.3333	0.0830
O 1	3 j	0.5000	0.5000	0.0000
O 2	3 k	0.8333	-0.8333	0.5000
O 3	6 n	0.1670	-0.1670	0.3333
O 4	6 n	0.8333	-0.8333	0.1670